CHANNELING IN SEMICONDUCTORS AND ITS APPLICATION TO THE STUDY OF ION IMPLANTATION

Thesis by

Samuel Thomas Picraux

In Partial Fulfillment of the Requirements

For the Degree of

Doctor of Philosophy

California Institute of Technology

Pasadena, California

1969

(Submitted April 30, 1969)

Acknowledgments

The author expresses his deepest appreciation to James W. Mayer who through his careful guidance introduced an exciting world of research rather than a perplexing plethora of facts and to John A. Davies for the stimulation and insight into channeling he provided. Special thanks go to Jens U. Andersen, Lennart Eriksson and Nils G. E. Johansson for exciting discussions and collaboration in various aspects of our research. The guidance and experimental assistance of Charles A. Barnes on the Kellogg Van de Graaff and Ogden J. Marsh with ion implantation were greatly appreciated.

The use of facilities at Chalk River Nuclear Laboratories, Hughes Research Laboratories and Caltech's Kellogg Radiation Laboratory are gratefully acknowledged. Financial support was generously supplied by Air Force Cambridge Research Laboratory and by a National Aeronautics and Space Administration Traineeship. The Kellogg Van de Graaff was supported by the National Science Foundation.

Abstract

The channeling characteristics of protons and helium ions in various diamond-type lattices (diamond, Si, Ge, GaP, GaAs, GaSb) have been studied by means of elastic backscattering in the 0.5 to 2 MeV range. Critical angles ($\psi_{\frac{1}{2}}$) and minimum yields (χ_{min}) have been measured and compared to theory. The values of $\psi_{\frac{1}{2}}$ for axial channeling have a functional dependence which agrees well with calculations based on the average potential along the row - both for uniform and for non-uniform spacing and (in the case of the compound semiconductors) for mixed atomic composition. Planar critical angles also show a functional dependence in agreement with average potential calculations. However, it is necessary to include in the calculation the effect of surface transmission which becomes increasingly important for higher order planar directions (e.g. lower atomic density of the planes). Measured full angular distributions are compared with calculated distributions for planar channeling. For both axial and planar channeling the measured critical angles are $\approx$ 25% lower in absolute magnitude than calculated.

Channeling and electrical measurements are combined to study ion implanted impurities in silicon. The lattice disorder and impurity atom lattice location are investigated by channeling effect measurements using a 1 MeV helium ion analyzing beam. The electrical type, number of carriers/cm^2 and mobility are determined by use of Hall effect and sheet resistivity measurements.

The anneal behavior of Cd and Te implantations (20-50 keV) into Si at substrate temperatures of 23^oC and 350^oC were investigated. The room

temperature Te implants showed substitutional behavior and donor action after anneal at 600°C. In room temperature Cd implantations, outdiffusion of the Cd was observed when the disordered layer annealed. Implantations of Cd at 350°C indicated the presence of an interstitial component and n-type behavior was observed.

Table of Contents

Acknowledgements	ii
Abstract	iii
Introduction	1
Chapter I Channeling in Semiconductors	3
I.1 Introduction	3
I.2 Experimental Method	7
I.3 Theory - Axial and Planar	16
I.3.1 Critical Angles	16
I.3.2 Minimum Yields	23
I.4 Results	28
I.4.1 Axial Channeling	30
I.4.2 Planar Channeling	40
I.5 Summary	54
Chapter II Applications to the Study of Ion Implantation	56
II.1 Introduction	56
II.2 Lattice Disorder	60
II.2.1 Technique	61
II.2.2 Results	65
II.3 Lattice Location of Impurities	70
II.3.1 Technique	71
II.3.2 Results	77
II.4 Hall Effect Measurements	80
II.4.1 Technique	84
II.4.2 Results	86

Table of Contents

II.5 Summary 89

Appendix A Table of Symbols 92

B Derivations for Critical Angles 94

C Limits of the Average Potential Approximation 100

D Planar Channeling Angular Distribution Calculation 104

E Useful Formulas for Channeling Applications 106

References 111

INTRODUCTION

In recent years, much effort has been spent in studying the motion of energetic charged particles in single crystals. Whenever a low-index crystal axis or plane is aligned with a beam of positively charged particles, one observes a significant reduction in energy loss and an even larger reduction in the yield of processes requiring a close encounter with the lattice atoms (such as elastic backscattering, nuclear reactions, and inner shell X-ray production). The interest in this "channeling" effect lies both in the further understanding of the channeled mechanism itself (Chapter I) and in its application to the study of the solid state (Chapter II).

Among the various applications of channeling as an analytical tool have been foreign atom location,[1,2] lattice disorder,[3] surface effects,[4] and nuclear lifetimes.[5] One particularly fruitful application has been the study of ion implantation in semiconductors[6] in which the lattice location of the implanted ions and the amount of disorder is determined from channeling effect measurements with MeV projectiles. Ion implantation is a means of introducing an impurity into a material by first ionizing the impurity atoms and then accelerating them to keV energies to inject them into the material. The impurity atoms typically penetrate 100 to 1000 Å, creating disorder as they come to rest. Typically, the implantations involve heavy ions (e.g. As) at keV energies and the analysis is carried out with light ions (e.g. He) at MeV energies.

Further insight has been made in the understanding of ion implan-

tation phenomena by combining channeling measurements with Hall and sheet resistivity measurements. Previous interpretation of measurements of the number of electrically active dopant species has been complicated by the combined effects of lattice defects and uncertainty in the lattice site location of the implanted species. The ability to measure the number of implanted atoms on lattice sites and the gross amount of lattice disorder as well as the number of carriers (by combining channeling and electrical measurements) often permits one to distinguish between the disorder and lattice location effects.

Some aspects of the work contained in this thesis have been published previously:

"Channeling in Diamond Type Lattices," Phys. Rev. (to be published, April, 1969) S. T. Picraux, J. A. Davies, L. Eriksson, N. G. E. Johansson and J. W. Mayer.

"The Influence of Surface Transmission on Planar Channeling in Semiconductors," (submitted to J. Appl. Phys.) S. T. Picraux and J. U. Andersen.

"Temperature Dependence of Lattice Disorder in Ion Implanted Silicon," Appl. Phys. Letters 14, 7 (1969) S. T. Picraux, J. E. Westmoreland, J. W. Mayer, O. J. Marsh and R. R. Hart.

"Analysis of Cd and Te Implantations in Silicon by Channeling and Hall Measurements," Proc. Electrochem. Soc. (to be published, May, 1969) S. T. Picraux, N. G. E. Johansson and J. W. Mayer.

"Ion Implantation of Silicon and Germanium at Room Temperature: Analysis by Means of 1.0 MeV Helium Ion Scattering," Can. J. Phys. 46, 663 (1968) J. W. Mayer, L. Eriksson, S. T. Picraux and J. A. Davies.

Chapter I

Channeling in Semiconductors

I.1 Introduction.

The channeling of an energetic beam of particles in a single crystal occurs whenever the crystal axis or plane is aligned with the beam direction. During channeling the incident particles are steered by a series of gentle collisions with the lattice atoms of the rows or planes. The influence of channeling on particle trajectories is most strikingly observed in the significant reduction in the energy loss of the particles passing through the crystal and the even larger reduction in processes requiring a close encounter with lattice atoms (e.g. large angle scattering, nuclear reactions, x-ray production). In order for an energetic beam of particles to be steered by the lattice, the beam direction must be oriented within a certain critical angle ($\psi_{\frac{1}{2}}$) of the crystal axis or plane. This critical angle can best be measured by one of the close encounter events such as large angle backscattering.

There are two reasons why the critical angle is a particularly interesting parameter to study in characterizing the channeling process. First, an elegant but simple theoretical framework has been developed by Lindhard[7] for quantitatively interpreting the channeling angular distributions and, in particular, the critical angle. A direct comparison between experiment and theory is thus possible. Second, from a practical point of view, it is essential to know $\psi_{\frac{1}{2}}$ for a given experimental situation in which one is using channeling as a tool in the study of solid state phenomena such as lattice disorder and impurity atom location.

Another characterization of the channeling process is the measurement of the yield of backscattered particles when the beam is perfectly aligned with a crystal axis or plane. The minimum yield (χ_{min}) is defined as the ratio of the yield in the perfectly aligned direction to that in a random direction.* In the aligned case, those particles which enter the crystal sufficiently close to a row (plane) of atoms are given a deflection larger than the critical angle. These deflected particles, typically 1 to 5% of the total number, can no longer be steered by the lattice rows and interact normally with the lattice atoms. Thus, the yield of backscattered particles does not drop to zero even under perfect alignment conditions; the minimum yield is a measure of this unchanneled fraction.

In the study of channeling itself, the diamond-type lattice is a particularly interesting structure. Within a given crystal one may select a direction where the steering of the channeled particles is due either to a row of uniformly spaced atoms (such as the $\langle 110 \rangle$, fig. I.1), or to a non-uniformly spaced row ($\langle 111 \rangle$). Furthermore, in a compound crystal such as GaP, one has, along the $\langle 110 \rangle$ (fig. I.2a), separate monatomic rows of Ga and P, whereas along the $\langle 111 \rangle$ direction all rows contain both Ga and P. In addition, due to the asymmetric spacing along the $\langle 111 \rangle$, the $\langle 111 \rangle$ and $\langle \bar{1}\bar{1}\bar{1} \rangle$ configurations are not equivalent. Similar variations may be found for certain planar configurations (fig. I.2b): the inter-planar spacing is uniform for the $\langle 110 \rangle$ and non-uniform for the $\langle 111 \rangle$; in compound crystals, individual planes also may or

*We will define such a "random" direction as an orientation for which the incident particles undergo no significant correlated collisions (i.e. the lattice appears as a random distribution of atoms).

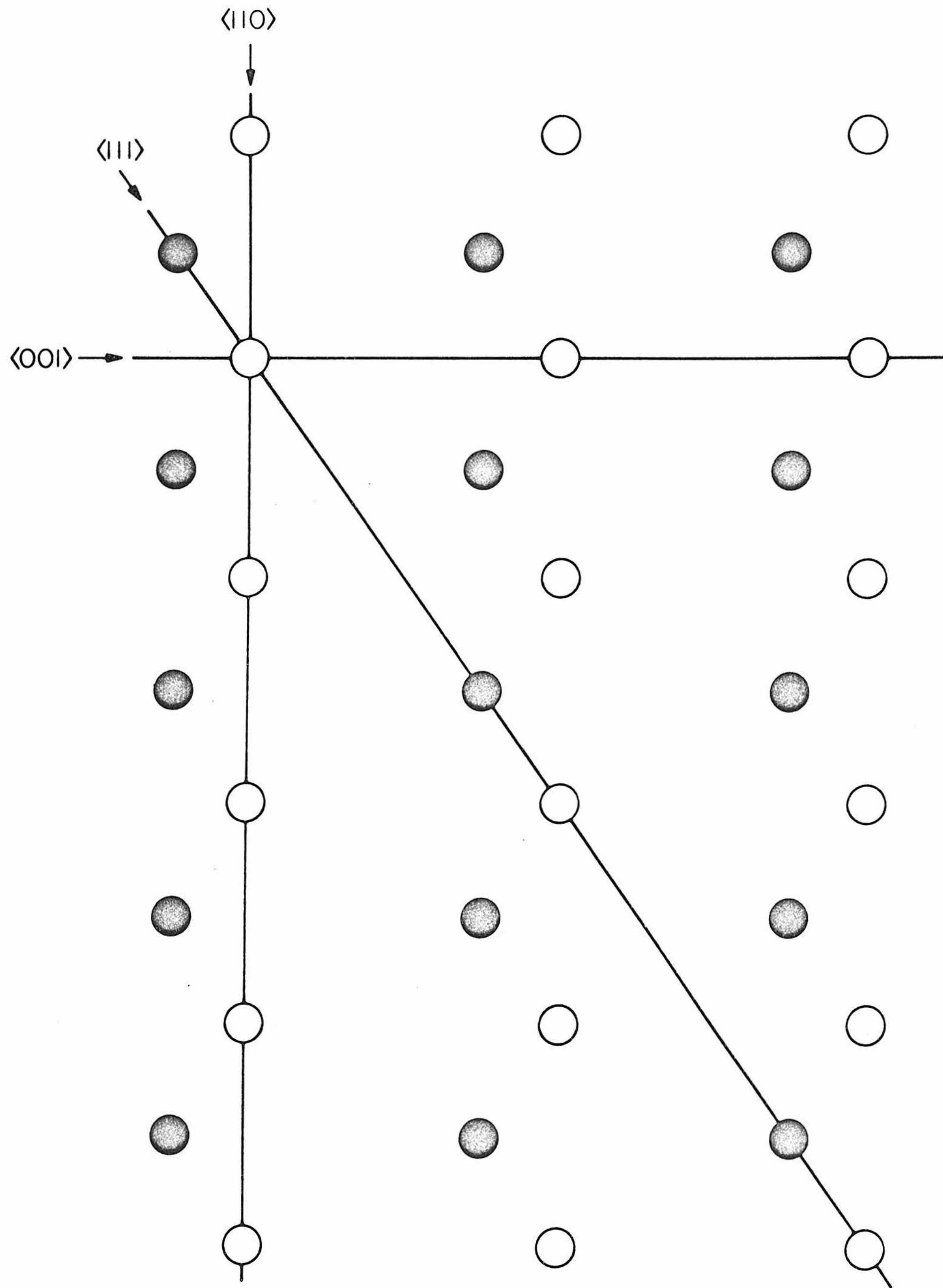

Fig. I.1 Atomic positions in the $\{1\bar{1}0\}$ plane of the diamond lattice structure showing the three major axial directions ⟨110⟩, ⟨111⟩, and ⟨001⟩. The solid and open circles distinguish between the two different types of atoms for a diatomic lattice such as GaP.

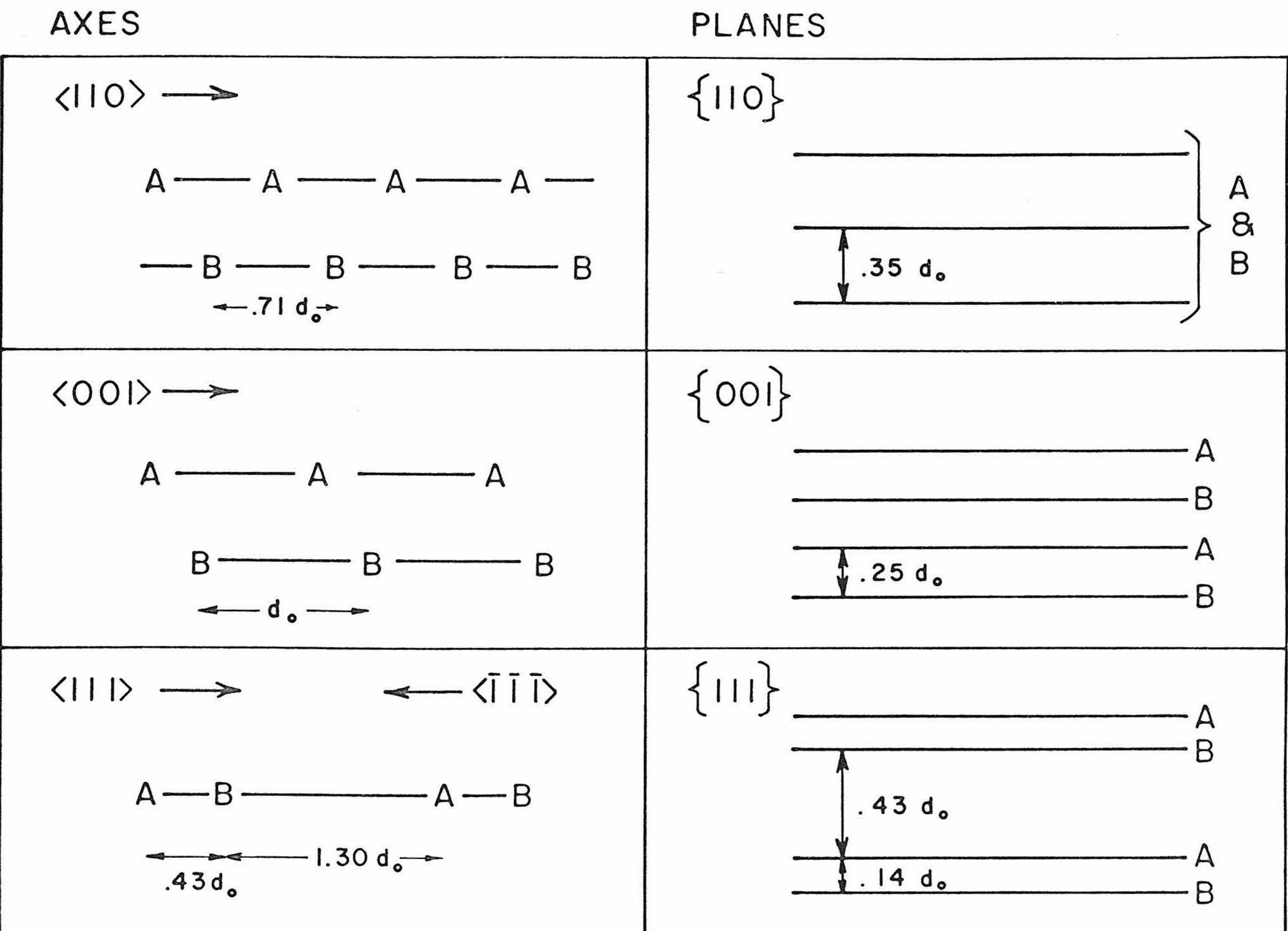

Fig. I.2 Spacing of atoms along axial directions and between planes for the diatomic diamond-type lattice with atoms A and B and lattice constant d_o. For monatomic lattices A = B.

may not contain both types of atoms (fig. I.2b).

The influence of different lattice spacing or composition is most directly seen in measurements of the critical angle, the minimum yield, and the energy loss for channeled particles. Previous channeling measurements have been made in the monatomic diamond lattices of Si and Ge by Appleton et al.[8] and Davies et al.[9] There have been channeled particle energy loss measurements in these materials and in GaAs by Sattler et al.[10]

The main purpose of this chapter is to explore the channeling behavior observed in various diamond-type lattices. In general we have used projectile energies of 500 keV to 2 MeV and wide-angle backscattering to investigate critical channeling angles. The advantage of backscattering is that good depth resolution is possible, and so the critical angle can be measured simultaneously at several depths within the first micron of the surface. This enables the effects of dechanneling to be investigated and a suitable correction applied, if necessary.

I.2 Experimental Method.

The measurements presented in this chapter were carried out on the Chalk River 2 MeV Van de Graaff. A monoenergetic beam of protons or helium ions was used. Typical currents were 2 nanoamps and the beam divergence was less than 0.05°. The backscattered particles were measured with a surface barrier detector placed about 5 cm from the crystal (fig. I.3). The scattering angle was 160° and the angle subtended by the detector was large ($\sim 12^{\circ}$) so as to reduce crystalline effects along the outgoing trajectory. Energy analysis was performed by a 100-channel analyzer and by eight single-channel analyzers with scalers.

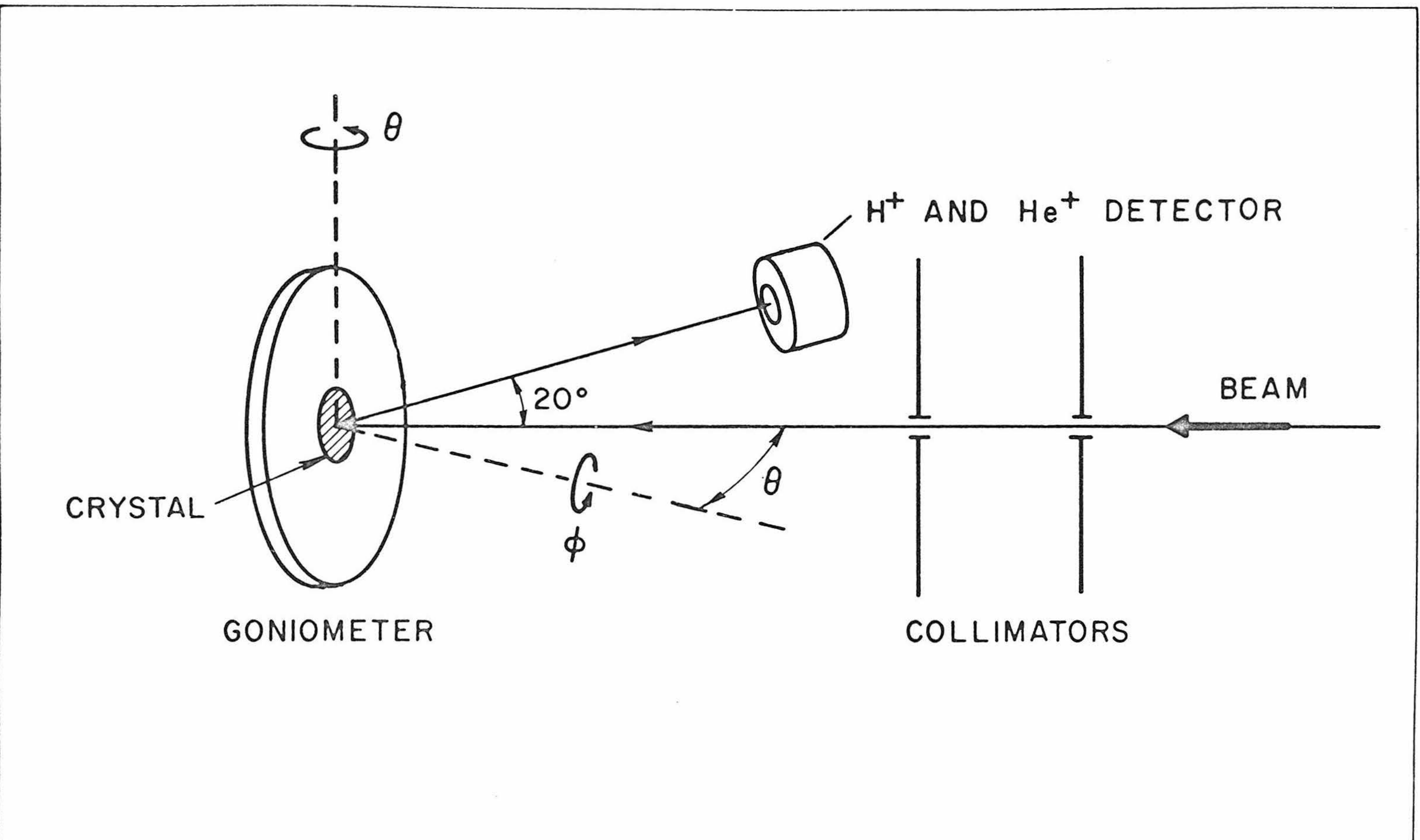

Fig. I.3 Schematic diagram of the experimental arrangement.

The energy resolution of the solid state detector was approximately 20 keV FWHM for 1 MeV helium ions. The electronics arrangement is shown in fig. I.4. The semiconductor samples were mounted in the scattering chamber on a goniometer (fig. I.3) such that the crystal could be rotated and tilted with respect to the direction of the incident beam. The goniometer rotation (φ) and tilt (θ) angles could be set reproducibly to 0.02°. An additional adjustment on the crystal holder made it possible to tilt the crystal until its axis coincided with the rotation axis (φ) of the goniometer. This simplified the measurement of axial critical angles.

Typical energy spectra of the backscattered particles are shown in fig. I.5a. The "random" spectrum is obtained by orienting the crystal so that the incident beam is not aligned with any crystal axis or plane. This means the incident particles do not undergo correlated collisions with the lattice atoms (i.e. the lattice appears as a random distribution of atoms). The particles with highest energy (i.e. at the spectrum edge) correspond to scattering off the surface of the crystal. The helium ions lose energy in electronic stopping processes as they move through the crystal so that the continuum at lower energies corresponds to scattering from progressively larger depths. The aligned spectrum shows the large reduction in backscattered yield when a crystal axis ($\langle 111 \rangle$ in this case) is parallel to the beam direction. Detailed orientation scans from two different depths in silicon are shown in fig. I.5b. These are obtained by recording the yield in the narrow energy regions 1 and 2 (fig. I.5a) while tilting the $\langle 111 \rangle$ axis through the beam direction. The critical angle is determined by measuring the

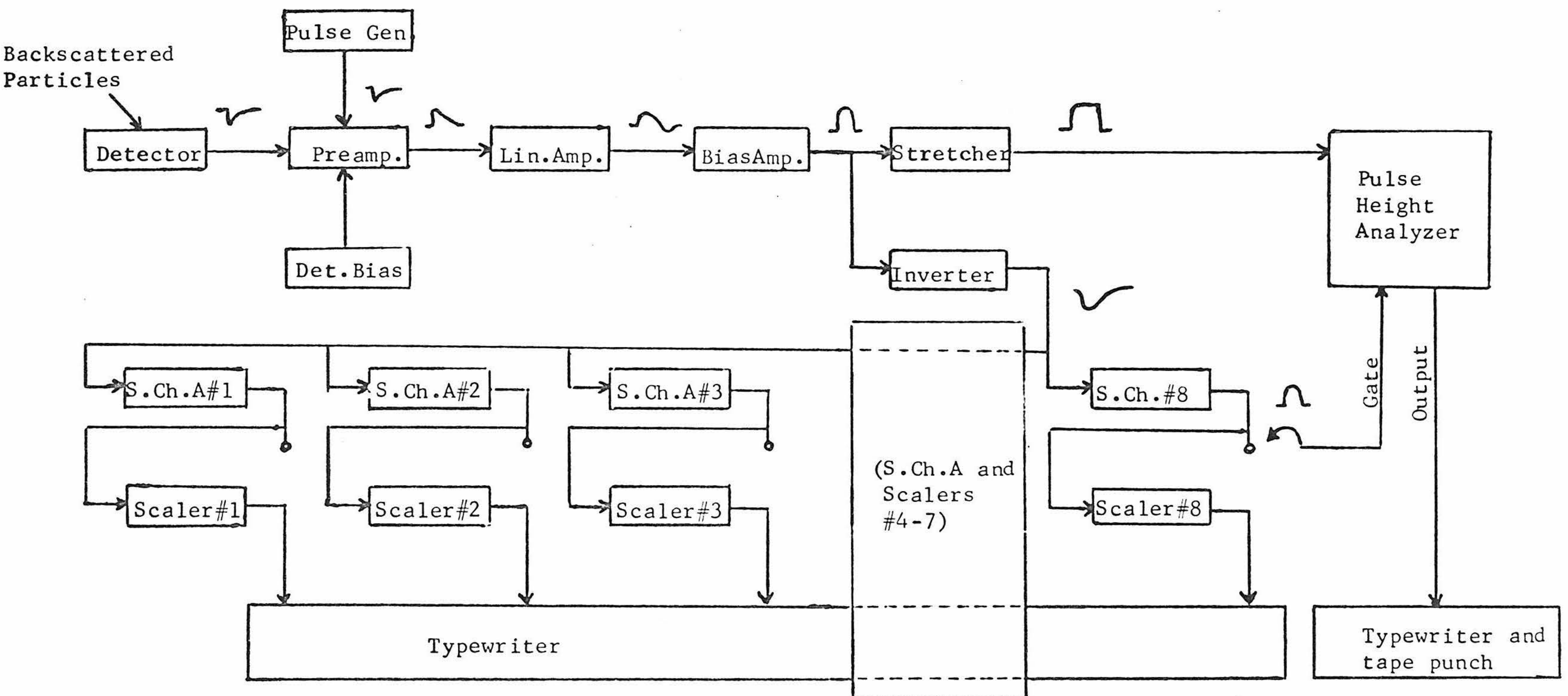

Fig. I.4 Schematic diagram of the electronic instrumentation for energy analysis of backscattered particles.

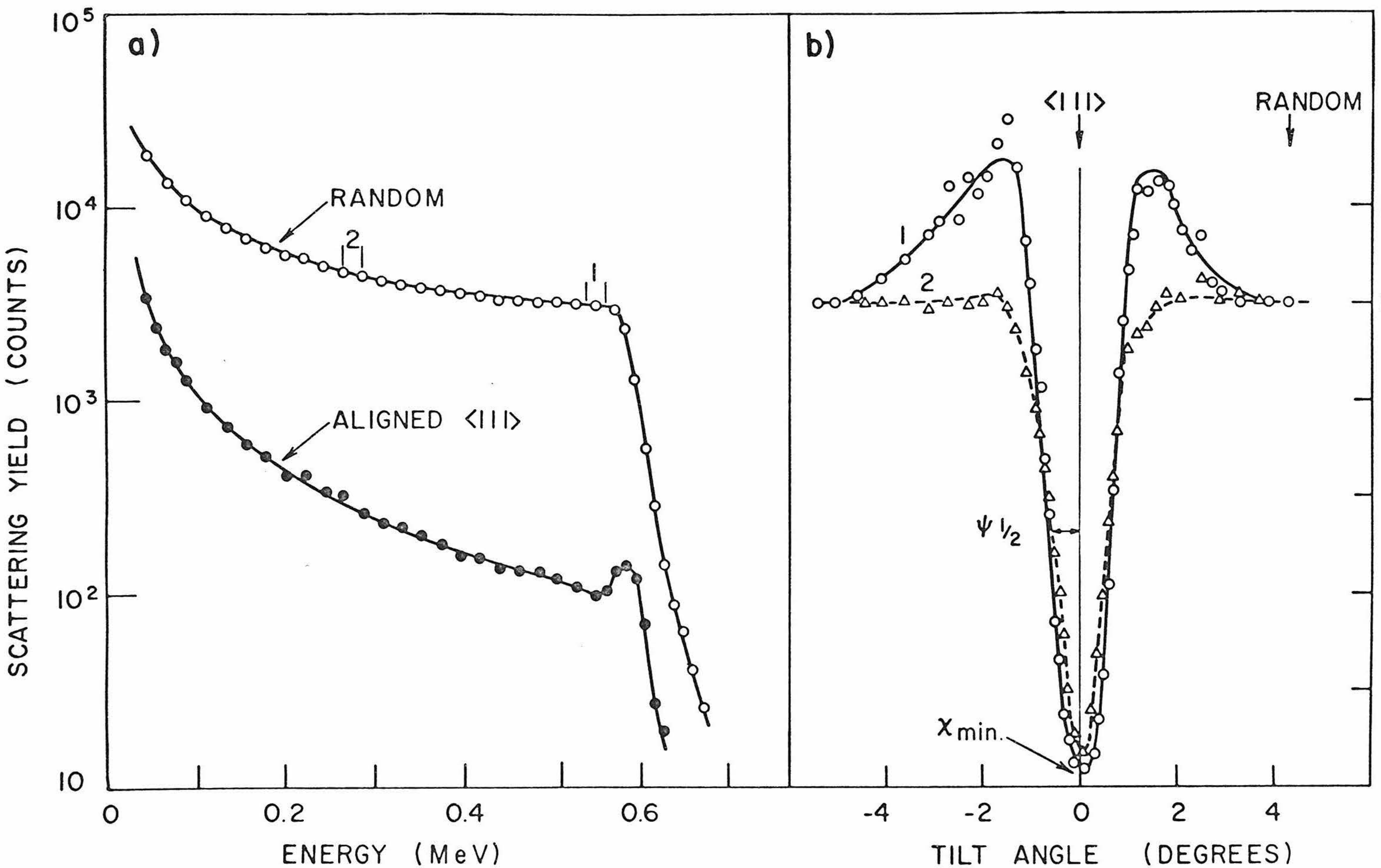

Fig. I.5a Energy spectra for 1 MeV helium ions backscattered from a silicon crystal: ●-beam incident along the ⟨111⟩;○-beam incident in a "random" direction. The energy regions 1 and 2 indicate the two single-channel-analyzer settings used in 5b. These correspond to depths of 900 and 6000 Å respectively.

Fig. I.5b Orientation dependence of the normalized yield obtained from the energy regions 1 and 2 (fig. 5a). Tilt angles marked "⟨111⟩ and "random" show the orientations at which the energy spectra of fig. 5a were taken.

angular half-width ($\psi_{\frac{1}{2}}$) at a level midway between the aligned and random levels. The accuracy of the axial critical angle measurements is estimated to be $\pm$ 0.06^{o}. The value of the minimum yield (χ_{min}) is shown in fig. I.5b.

In order to compare the measured values of $\psi_{\frac{1}{2}}$ and χ_{min} with theoretical predictions, it is necessary that these are representative of their values near the surface. The minimum yield which is a measure of the unchanneled fraction is depth dependent because some of the channeled particles can be deflected outside the critical angle (dechanneled) as they penetrate deeper into the crystal. The fraction of the beam that has been dechanneled increases with depth leading to an increase in minimum yield. The depth dependence of the minimum yield can be obtained from the aligned and random spectra of fig. I.5a. The fraction of the beam that is still channeled is given by (1-χ_{min}). From the results in fig. I.6, it can be seen that, even at a depth of 6000 Å, more than 90% of the beam is still channeled. Germanium, which has a larger thermal vibrational amplitude, shows a significantly larger dechanneling rate than silicon.

The critical angle also is dependent on the depth from which the backscattering occurs as is illustrated in figs. I.5b and I.7. In the case of silicon, we see very little difference between the ⟨111⟩ critical angle for 1 MeV helium ions at 900 and 6000 Å (fig. I.5b). On the other hand, in germanium a significant variation is observed over the same depth region (fig. I.7); in this case, the angles are measured simultaneously for scattering from several depths over the region 500 - 8000 Å, and extrapolation to the surface is then made to allow comparison

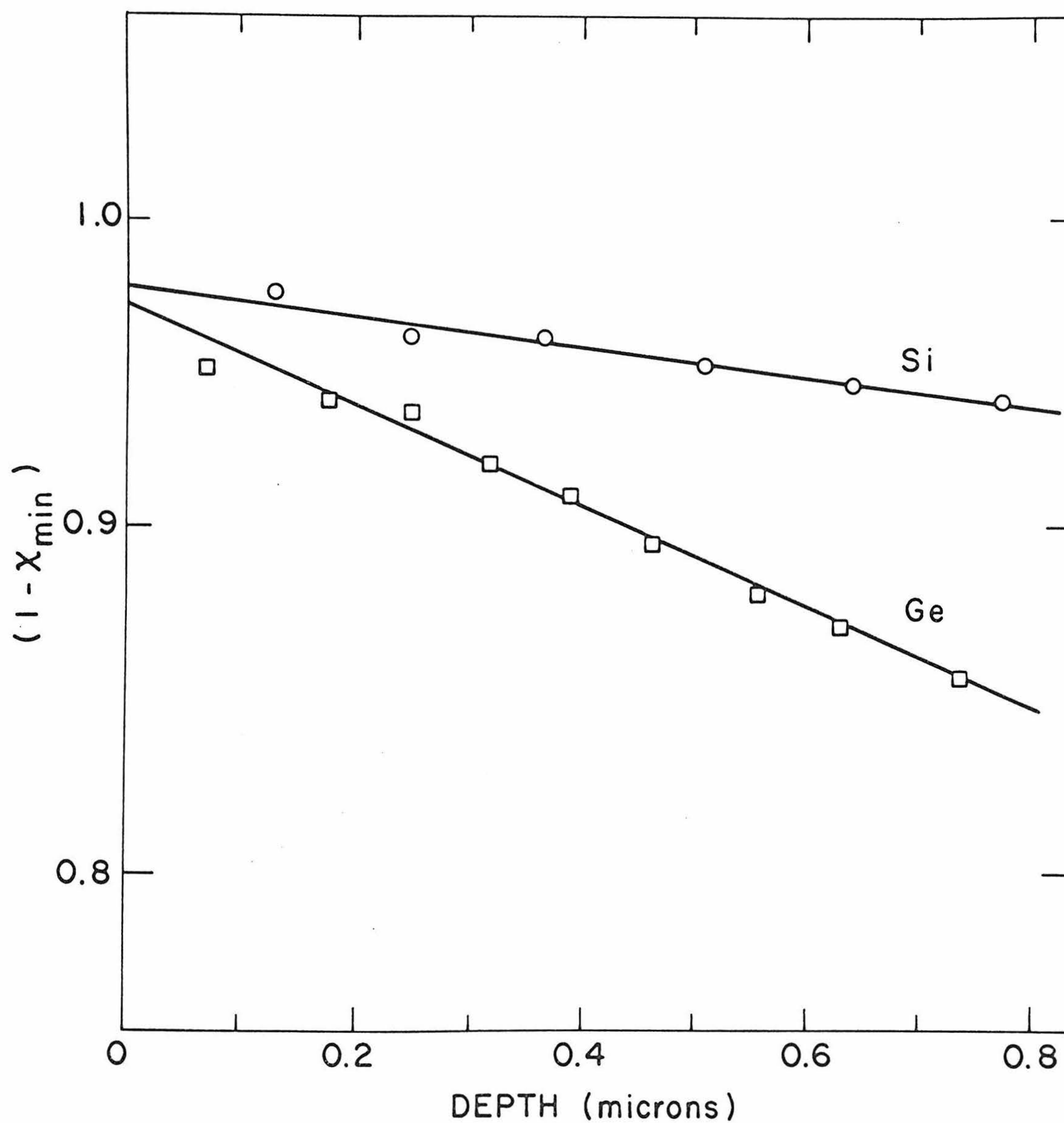

Fig. I.6 Depth dependence of χ_{min} for 1 MeV helium ions along the ⟨111⟩ axis in silicon and germanium.

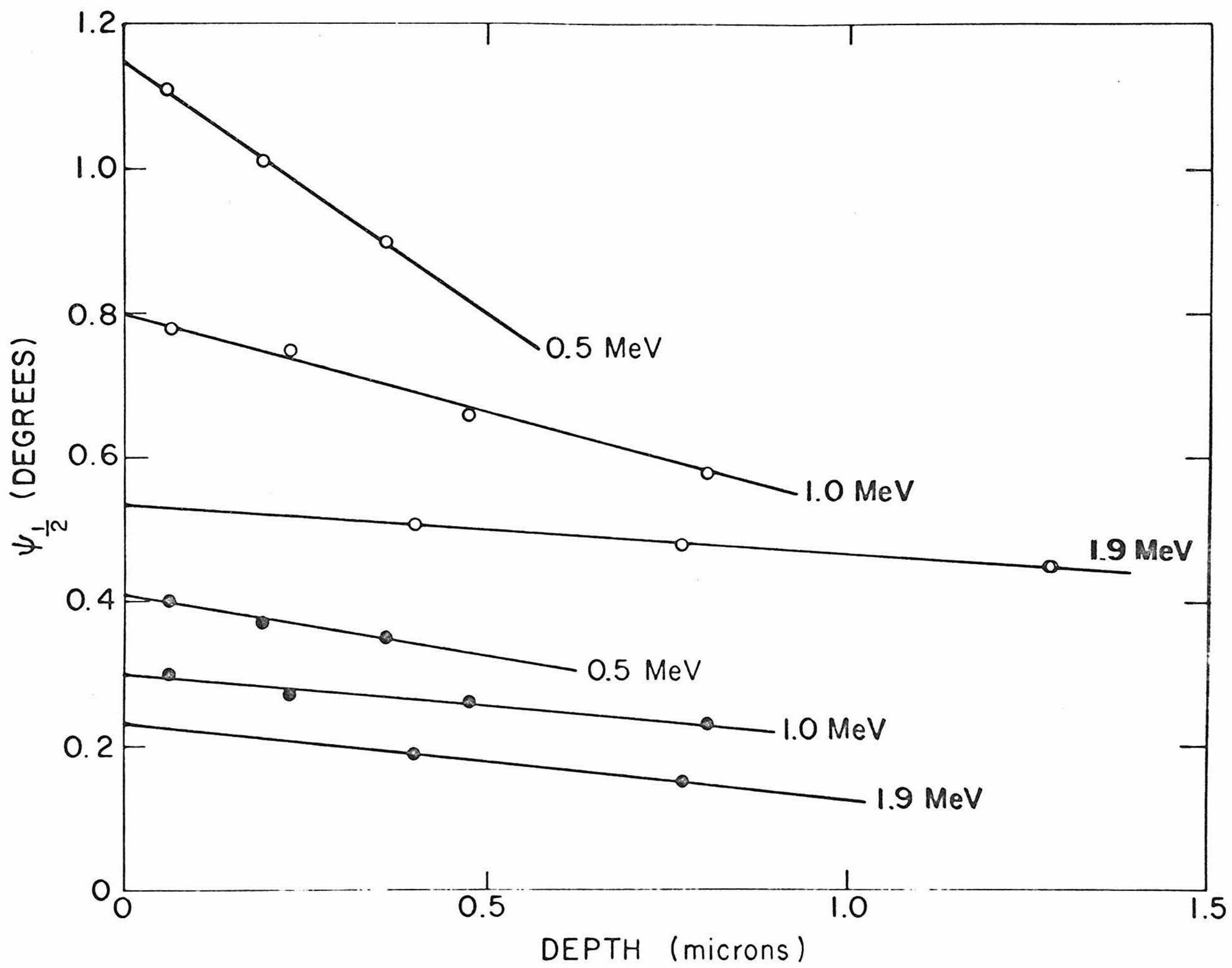

Fig. I.7 Depth dependence of $\psi_{\frac{1}{2}}$ for the $\langle 111 \rangle$ axis (O) and the $\{110\}$ plane (●) in germanium, using 0.5, 1.0 and 1.9 MeV He ions.

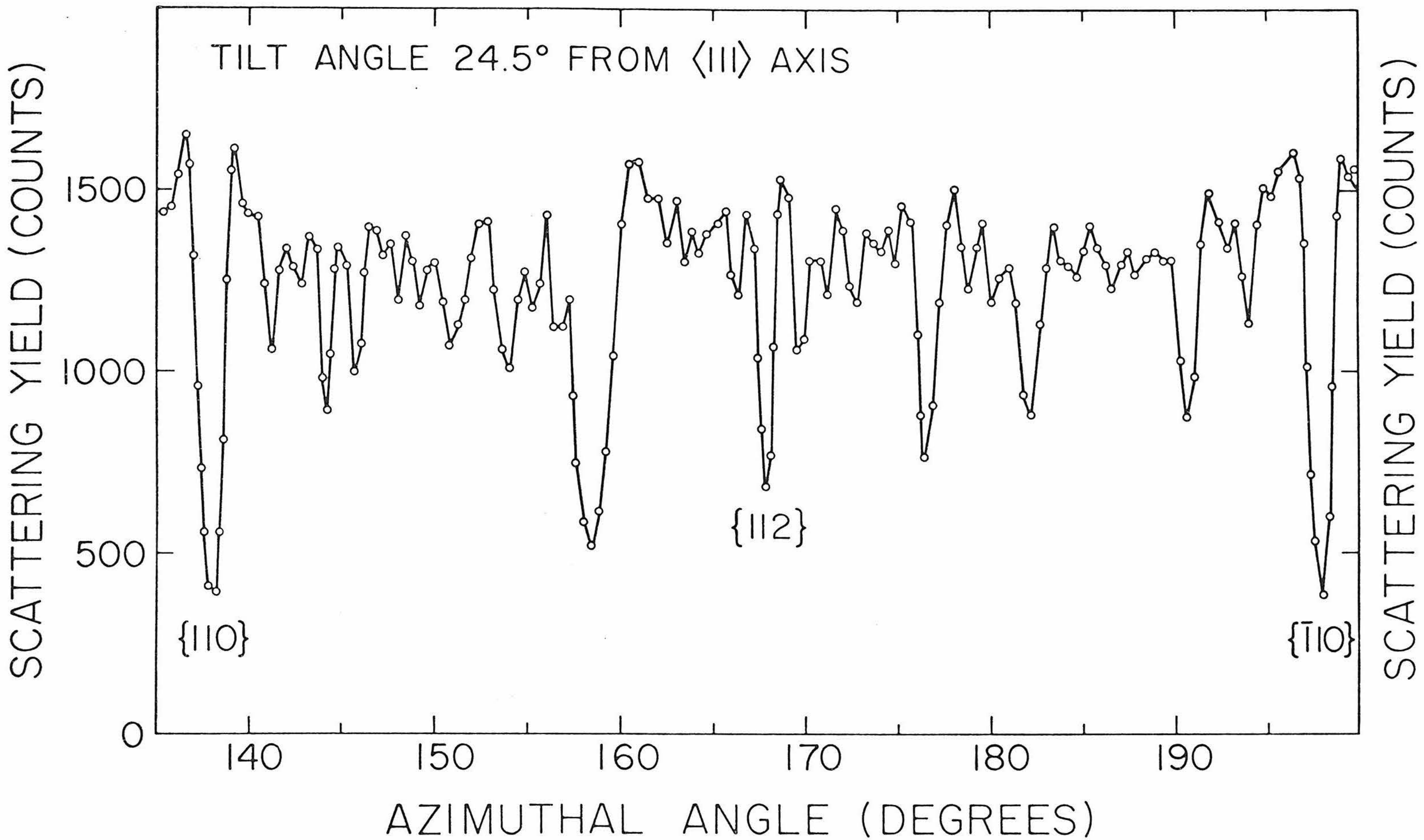

Fig. I.8 Planar channeling of 1.0 MeV helium ions in germanium, measured by rotating around the ⟨111⟩ axis at a tilt angle of 24.5°.

with theory. Figure I.7 also demonstrates the increased importance of depth effects at lower projectile energies in the axial case. For planar channeling, on the other hand, the depth dependence of $\psi_{\frac{1}{2}}$ is seen to be rather small and is relatively insensitive to energy variations although percentage differences are more difficult to detect due to the smaller magnitudes involved.

In measuring axial and planar critical angles, it is necessary to avoid competing effects from higher order directions or planes. Fig. I.8 indicates the complexity that exists when the crystal has been tilted 24.5^{o} from the $\langle 111 \rangle$ and the yield is measured as a function of rotation. Care must be taken to find a position which is representative of an average (random) yield.

I.3 Theory - Axial and Planar.

I.3.1 Critical Angles.

Channeling in single crystals is described on the basis that a particle moving at a small angle with respect to a row or plane of atoms is steered by a series of gentle correlated collisions with many lattice atoms in the row or plane.[7,11] The requirement that the individual atomic collisions be gentle implies that the deflection given to the particle during a single collision is small compared to the total angle through which the particle is steered (see Appendix C for calculation). Based on Lindhard's treatment,[7] we describe the steering of the particle by its interaction with the average potential of the row or plane (e.g. the discrete atomic potentials

are replaced by a continuum model).* Lindhard has shown that a good approximation is to treat the transverse energy of the channeled particle as conserved. If the energy in the transverse motion of the particle is insufficient to overcome the potential barrier presented by the lattice row (plane) then we may write

$$\bar{V}(r) = \tfrac{1}{2} M_1 (v\sin\psi)^2$$
$$\approx E\psi^2$$

where $\frac{1}{2}M_1v^2$ is the energy (E) of the particle, ψ the angle of incidence of the particle with respect to the row and $\bar{V}(r)$ the average potential at an impact parameter r with the row corresponding to incident angle ψ. The minimum impact parameter (r_{min}) corresponds to the maximum or "critical" angle ($\psi = \psi_{\frac{1}{2}}$) for which the particle can be steered by the crystal row (see Appendix B.1). For larger angles of incidence the particle penetrates the row and is able to undergo large angle scattering. Thus

$$\psi_{\frac{1}{2}} = \sqrt{\frac{\bar{V}(r_{min})}{E}} \, . \qquad \text{(I.1)}$$

Typical values of $\psi_{\frac{1}{2}}$ for MeV He ions incident on silicon are less than one degree (0.2°-0.8°). For axial channeling, we obtain (see Appendix B.2)

---

*Detailed angular distribution calculations for axial channeling have been performed by Feldman[12] without the use of the average potential approximation by following the individual collisions in a Monte Carlo type calculation. Comparison of these results[13] to average potential calculations by Andersen[14] has shown good agreement over the range of validity of the average potential model.

$$\psi_{\frac{1}{2}} = \alpha\, \psi_1 \;, \text{ for } \psi_1 < a/d \tag{I.2}$$

where

$$\psi_1 = \left[\frac{2Z_1Z_2e^2}{Ed}\right]^{\frac{1}{2}} \tag{I.3}$$

$$\alpha = \left[\tfrac{1}{2}\log\left(\frac{3a^2}{\rho_r^{\,2}\log 2} + 1\right)\right]^{\frac{1}{2}} \;, \text{ for } \psi_1 < \rho_r/d \tag{I.4}$$

and Z_1, Z_2 are projectile and lattice atomic numbers, d is the spacing along the row, a the Thomas-Fermi screening distance, and $\rho_r^{\,2}$ the mean square vibrational amplitude of the lattice atoms in the plane perpendicular to the row. The main functional dependence of the critical angle is contained in ψ_1 which involves energy, atomic number, and lattice spacing. Note that Z_2e/d is simply the nuclear charge per unit distance along the row. The constant α depends only on the vibrational amplitude and the screening distance, a, associated with the potential ($a = 0.886\, a_o \left(Z_1^{\,2/3} + Z_2^{\,2/3}\right)^{-\frac{1}{2}} \approx 0.1$ to 0.2 Å where a_o = Bohr radius). The value of α is of the order of unity. Detailed numerical calculations by J. U. Andersen[14] have shown that eq. I.4 is accurate in the region $\psi_1 < \rho/d$. The measurements presented in this work have been at sufficiently high energies ($\psi_1 < a/d, \rho_r/d$) that the average potential model holds and the above equations are valid (see Appendix C).

An extension of the average potential model to the case of more than one type of atom along the rows and of non-uniform spacing of the atoms along the row results in a simple modification of the ψ_1 formula,

$$\psi_1 = \left[\frac{2Z_1\bar{Z}_2e^2}{E\bar{d}}\right]^{\frac{1}{2}} \qquad (I.5)$$

where $\bar{Z}_2$ is the average atomic number of the atoms along the row and $\bar{d}$ is the average spacing of the atoms along the row. One of the purposes of this work was to determine experimentally if our simple extension was valid.

The planar case is treated in a similar manner. The use of an average planar potential for the case of uniformly spaced planes leads to a planar critical angle

$$\psi_{\frac{1}{2}} = \beta'\psi_n \; , \quad \text{for } \psi_n < 2Nd_pa^2 \qquad (I.6)$$

where

$$\psi_n = \left[\frac{Z_1Z_2e^2Nd_pa}{E}\right]^{\frac{1}{2}} \; , \qquad (I.7)$$

$$\beta' = b\beta \; , \quad (b < 1)^*$$

$$\beta = \left\{\frac{2\pi}{a}\left[\left(y_{min}^2 + 3a^2\right)^{\frac{1}{2}} - y_{min}\right]\right\}^{\frac{1}{2}} \qquad (I.8)$$

and N is the atomic density, d_p the spacing between planes, and y_{min} the minimum impact parameter (see Appendix B.4 and C for details). Note that Z_2eNd_p in eq. I.7 is simply the nuclear charge density (n_p) of the monatomic uniformly spaced planes. This case differs from that for axial channeling in that we are unable to solve for the minimum impact parameter explicitly. In the axial case, one can use the angular dis-

*The value of b depends on the influence of the surface transmission (as discussed in I.3b): e.g. for {110} planar direction in Si b = 0.7.

tribution function (eq. B.1) to solve for the minimum impact parameter and include the effect of vibrational amplitude ($r_{min} = \rho_r\sqrt{\log 2}$, Appendix B.1). For the planar case, the distribution function (eq. D.2) could not be solved explicitly. However, from the distribution function calculated by numerical integration for the case inside the crystal (i.e. without surface transmission effects), one obtains $\psi_{\frac{1}{2}}$. Then for the case of helium in silicon, we get the value $\beta = 2.7$; this value together with eq. I.8 gives $y_{min} = 0.7a$. This should be treated only as a rough estimate since the minimum impact parameter is a rather sensitive function of β and is a somewhat less well defined quantity in planar channeling. Also the value of y_{min} may be influenced by thermal vibration but this effect will not have a strong influence on the value of β.

Experimental results taken on different semiconductors with different ρ values also indicate that β' is relatively insensitive to variations of vibrational amplitude (compare axial and planar, figs. I.10a and I.14). This means a satisfactory estimate can be made of $\psi_{\frac{1}{2}}$ planar values without including the influence of thermal vibrations. Qualitatively, planar critical angles should be less sensitive to a change in vibrational amplitude. This can be seen by making an order of magnitude estimate of the steepness of the planar average potential relative to that for the axial case in the region of the minimum impact parameter. We will use the average potentials (see Appendix B) and choose $\rho \approx a$ to compare the slope of the potentials at $r_{min} \approx y_{min} \approx a$. With these conditions, the ratio of the planar to axial slope, $\overline{V}'(y_{min}=a)/\overline{V}'(r_{min}=a)$ is $2dNd_pa$. Typical values of the slope of the planar average potential are a factor of 6 lower than the axial $\overline{V}$ in this region. Thus the ther-

mal vibrations which are of the order of y_{min} will have a smaller effect on the planar average potential.

For cases other than the monatomic uniformly-spaced planes considered above the nuclear charge density of the planes is no longer simply $n_p = Z_2 eNd_p$ and one must select values of Z_2 and d_p for eq. I.7 consistent with the average potential model. In the case of uniformly spaced planes of identical atomic composition containing more than one type of atom, Z_2 must be replaced by $\overline{Z}_2$, the average atomic number in the plane. For non-uniform planar spacing, the atomic configuration must be considered in detail. For example, in the {111} direction in the diamond type lattice, the planar atomic density is the <u>same</u> even though the spacing is non-uniform. So for a monatomic lattice d_p is replaced by the average spacing. However, in the case of a compound lattice, the two different planes contain different types of atoms and so the average planar nuclear charge densities are different ($Z_{2A} eN\overline{d}_p$ and $Z_{2B} eN\overline{d}_p$) and a unique result for $\psi_{\frac{1}{2}}$ is not obtained.

The major advantage of the critical angle treatment given above is the simplicity of the resulting formulas and the insight they give into the channeling process. The major effects which have not been included in this discussion of critical angles are

a) Thermal vibrations (partly included in axial case)

b) Surface transmission

c) Depth dependence

The significance of these effects will be discussed in turn.

a) <u>Thermal vibrations</u>. The influence of thermal vibrations on the axial critical angle has been treated in the parameter α (Appen-

dix B.1). In determining this parameter, only the lattice atom with which the particle interacts in a close encounter event is considered to be vibrating. The slight lowering of the average potential field due to the vibration of the rest of the atoms in the lattice has not been included. However, Erginsoy[(15)] has found this effect to be small. Our experimental results indicate that the functional dependence of the critical angle on vibrational amplitude is consistent with these calculations. Andersen and Uggerhøj [(16)] also found agreement for the case of protons in tungsten in the low energy region. Thermal vibrations have not been included in our critical angle treatment of the planar case except for the full distribution calculations (Appendix D). Our experimental results and the qualitative arguments discussed above both indicate that this does not have a strong effect on planar critical angles.

b) Surface transmission. When the incident beam of particles passes into (or out of) the crystal lattice along a channeling direction, the angular distribution of the particles is modified for those particles passing closest to a crystal row or plane. This leads to a reduction in the observed critical angle. Detailed numerical calculations including this effect have been made by Andersen.[(14)] He has shown that the effect on axial critical angles is negligible; but, for planar channeling, there is a dependence of critical angle on planar spacing in addition to the $\sqrt{d_p}$ found in ψ_n (eq. I.7). Using Andersen's procedure (Appendix D), we have calculated the planar critical angles and full angular distributions for the different diamond lattice semiconductors for comparison with our experimental data. We include in our planar critical angle formula for β' a surface transmission factor b ($\beta'=b\beta$) which

accounts for the reduction of the angular width. The value of b depends upon the planar spacing. Numerical solutions give, for example, b = 0.7 for helium in silicon along the {110} for d_p = 1.92 Å.

c) <u>Depth dependence</u>. There is a change in the transverse energy distribution (and thus angular distribution) as the particles penetrate deeper into the crystal. This effect is easily observed in the measurement of the critical angle as a function of depth (fig. I.7) and is seen to be more pronounced at lower incident beam energies. In general, the depth dependence of such parameters as $\psi_{\frac{1}{2}}$ and χ_{min} is expected to become more important as the roughness of the potential increases[17] due to such effects as increased thermal vibrations, change from monatomic to compound lattices or other changes of projectile and lattice such that ψ_1 increases towards a/d. This depth dependence has not yet been treated analytically except in a few special cases.[17,18] Since there is not a general treatment, we have measured the $\psi_{\frac{1}{2}}$ values as near to the surface as possible. In cases of rapid variation (fig. I.7), the values are obtained by extrapolation to zero depth.

<u>I.3.2 Minimum Yields</u>. The minimum yield χ_{min} (χ_{min} = aligned yield/random yield) is another useful experimental parameter for characterizing the channeling behavior since it is a measure of that fraction of the beam which is not channeled. Its value for particles scattered near the surface is essentially just the fraction of the beam penetrating the crystal sufficiently near a crystal row (or plane) so that this fraction of the particles are deflected by more than the critical angle and are no longer channeled. This impact distance r_{min} is a fairly well defined quantity for axial channeling. Therefore, an estimate of the

minimum yield for axial channeling can be made from the ratio of the areas around the row (πr_{min}^2) to the total crystal area per row (1/Nd),

$$\chi_{min} = \pi N d r_{min}^2 \tag{I.9}$$

where N is the atomic density, d the lattice spacing along the row and r_{min} is the minimum impact parameter for a channeled particle with the row. Using the result of Appendix B.1 ($r_{min}^2 = \rho_r^2 \log 2$), one can obtain a rough estimate of $\chi_{min} \approx \pi N d \rho_r^2$ or for small vibrations $r_{min} \approx a$ giving $\chi_{min} \approx \pi N d a^2$ where ρ_r^2 is the mean square vibrational amplitude perpendicular to the row and a is the Thomas-Fermi screening distance.

Although the minimum impact parameter y_{min} is not as well defined as in the axial case, a crude estimate of the minimum yield for planar channeling can be obtained from the fraction of the total area that is within y_{min} giving

$$(\chi_{min})_p = 2y_{min}/d_p \ . \tag{I.10}$$

If we use $y_{min} \approx a$, we obtain as a rough estimate $\chi_{min} \approx 2a/d_p$.

For comparison to experimental results, a better procedure is to relate the minimum yield directly to the critical angle through the minimum impact parameter by

$$E(\psi_{\frac{1}{2}})^2 = \bar{V}(r_{min}) \ .$$

The result for axial channeling is obtained in Appendix A.3,

$$\chi_{min} = \frac{\pi^3}{16} N d a^2 \left(\frac{\psi_1}{\psi_{\frac{1}{2}}}\right)^4 \ . \tag{I.11}$$

In this way, the effect of thermal vibrations is included through an experimentally determined quantity $\psi_{\frac{1}{2}}$.

For deeper depths in the crystal, the contributions to χ_{min} due to dechanneling of particles which were initially channeled becomes important.[17,19] The same factors which affect the depth dependence of the critical angle also play a role in the minimum yield. For comparison with the prediction of eq. I.11, we will restrict our attention to minimum yield measurements made near the surface.

The treatment of channeling in this section is summarized in Table Ia. Experimental results for semiconductors (presented later) indicate that the observed values of critical angles are approximately 25% lower in magnitude than those obtained from the equations in Table Ia. In Table Ib, typical values of the relevant parameters are given for 1 MeV helium ions in silicon.

Table Ia

Summary of Channeling Parameters

	Axial	Planar
Average Potential	$\overline{V}(r)=\frac{Z_1Z_2e^2}{d}\log\left[\left(\frac{ca}{r}\right)^2+1\right]$	$\overline{V}(y)=2\pi Z_1Z_2e^2Nd_p\left[\left(y^2+c^2a^2\right)^{\frac{1}{2}}-y\right]$
Condition	$\psi_1 < a/d$	$\psi_n < 2Nd_pa^2$
Critical Angle	$\psi_{\frac{1}{2}} = \alpha\psi_1$ $\psi_1 = \sqrt{\frac{2Z_1Z_2e^2}{Ed}}$ $\alpha=\left[\frac{1}{2}\log\left(\frac{3a^2}{\rho_r^2\log2}+1\right)\right]^{\frac{1}{2}}$ for $\psi_1 < \rho_r/d$	$\psi_{\frac{1}{2}} = \beta'\psi_n$ $\psi_n=\sqrt{\frac{Z_1Z_2e^2Nd_pa}{E}}$ $\beta = \left\{\frac{2\pi}{a}\left[\left(y_{min}^2+3a^2\right)^{\frac{1}{2}}-y_{min}\right]\right\}^{\frac{1}{2}}$ $\beta' = b\beta$
Minimum Impact Parameter	$r_{min} \simeq \rho_r \log2$	$y_{min} \simeq 0.7a$
Surface Transmission	negligible for $\psi_{\frac{1}{2}}$	$b \simeq 0.7$ (for {110} planar direction where $d_p \approx 2$Å)
Minimum Yield	$\chi_{min} = \pi N d r_{min}^2$	$(\chi_{min})_p = 2\, y_{min}/d_p$

Table Ib

Typical Calculated Values: 1 MeV He^+ in Silicon

$a = 0.17$ Å

Lattice constant $d_o = 5.43$ Å

Axial	Planar
⟨110⟩: $d = \frac{d_o}{\sqrt{2}} = 3.84$ Å	{110}: $d_p = \frac{d_o}{2\sqrt{2}} = 1.92$ Å
⟨111⟩: $\bar{d} = \frac{\sqrt{3}d_o}{2} = 4.70$ Å	{100}: $d_p = d_o/4 = 1.36$ Å
	{112}: $d_p = d_o/2\sqrt{6} = 1.11$ Å
$\rho_r = 0.106$ Å	
$r_{min} = 0.088$ Å	$y_{min} = 0.12$ Å
⟨110⟩: $a/d = 2.5^o$	{110}: $2Nd_pa^2 = 0.33^o$
⟨110⟩: $\rho_r/d = 1.6^o$	
⟨110⟩: $\bar{V}(r_{min}) = 265$ eV	{110}: $\bar{V}(y_{min}) = 50$ eV
⟨110⟩: $\psi_1 = 0.83^o$	{110}: $\psi_n = 0.15^o$
$\alpha = 1.12_5$	$\beta = 2.7$
	{110}: $b = 0.70$
⟨111⟩: $\psi_1 = 0.75^o$	{100}: $b = 0.62_5$
	{112}: $b = 0.58$
	{110}: $\beta' = 1.9$
⟨110⟩: $\psi_{\frac{1}{2}} = 0.94$	{110}: $\psi_{\frac{1}{2}} = 0.28$
⟨110⟩: $\chi_{min} = 0.005$	{110}: $\chi_{min} = 0.13$

1.4 Results.

The channeling critical angles and minimum yields have been measured by means of backscattering of 0.5 to 1.9 MeV helium ions in C (diamond), Si, Ge, GaAs, GaP and GaSb. Some measurements have also been made using protons. The value of primary interest is the critical angle at the surface which is obtained by measuring the critical angle at several depths by energy analysis of the backscattered particles and extrapolating to zero depth. The critical angle measurements are summarized in Table II. The main purpose of this section will be to present these values in the curves that follow and discuss the results on the basis of the average potential model.

We first treat the axial channeling critical angles for the effect of changing from uniform to non-uniform atomic spacing along the row. Then the results for different monatomic lattices are compared and the importance of thermal vibrations of the lattice atoms is demonstrated. Finally axial critical angles for compound semiconductors are included for the case of mixed atomic rows and pure rows of two different types.

The axial minimum yields are compared first to estimates of their theoretical values and then directly to the critical angle measurements through a derived relationship between these two parameters.

The planar critical angles are related according to the planar spacing and the importance of surface transmission is demonstrated. The critical angles are compared for different semiconductors for both monatomic and diatomic planes. Full planar channeling angular distributions are also correlated with calculated results for a number of representative cases.

Table II

Critical Angles[a] in Diamond Type Lattices

Crystal	Z_1	E (MeV)	$\psi_{\frac{1}{2}}$ axial		$\psi_{\frac{1}{2}}$ planar				
			⟨111⟩	⟨110⟩	{110}	{111}	{001}	{112}	{113}
Si		.25		1.02	.32	.33	.25	.20	.16
$\alpha = 1.12_5$		.50		0.68	.24	.26	.17	.16	.13
		1.00		0.53	.16	.20	.12	.11	.10
		2.00		0.36	.12	.13	.08	.08	.08
	He^+	.50	.98	1.10	.30	.32	.23	.19	.16
		1.00	.69	.75	.22	.26	.18	.13	.16
		2.00	.46	.55	.17	.16	.13	.09	.09
Ge	He^+	.50	1.13		.40				
		1.00	.80	.95	.30	.23	.18	.20	
$\alpha = 1.00$		1.90	.54		.23				
C(diamond)	H^+	1.00	.46	.54	.16				
$\alpha = 1.44$	He^+	1.00	.58	.75					
GaAs	He^+	.50	1.07		.33				
$\alpha = 1.03$		1.00	.81		.24				
		1.90	.48		.14				
GaP	He^+	.50	1.03		.38				
$\alpha = 1.14$		1.00	.74	.99	.25	.26	.18	.18	
		1.90	.59		.18				
GaSb	He^+	.50	1.16						
$\alpha = 0.94$		1.00	.88	1.10	.28	.25	.17		

(a) Estimated error for axial measurements $\pm 0.06^{\circ}$.
Estimated error for planar maasurements $\pm 0.03^{\circ}$.

I.4.1 Axial Channeling. A comparison of $\psi_{\frac{1}{2}}$ values for the ⟨110⟩ and the ⟨111⟩ directions in a given monatomic crystal enables the change from uniform to non-uniform spacing (fig. I.1) to be studied, while keeping all other parameters fixed. This is shown in fig. I.9 for measurements in silicon at energies ranging from 250 keV to 2 MeV. The predicted value for the ⟨111⟩ direction, derived from the best fit to the ⟨110⟩ data and the change in the lattice spacing, is shown using the maximum (d_{max} = 1.30 d_o), minimum (d_{min} = 0.43 d_o), and average ($\bar{d}$ = 0.87 d_o) spacing along the ⟨111⟩ (cf. fig. I.2). The experimental values (+) agree closely with the predicted curve using the average lattice spacing $\bar{d}$. Critical angle data for the {110} plane are included in fig. I.9 to illustrate the relative magnitude for planar channeling.

The critical angles in different diamond-type lattices are presented in fig. I.10a. Here the predicted dependence on lattice spacing, $\bar{d}$, has been removed by including a $(\bar{d})^{\frac{1}{2}}$ term in the abscissa. This enables both the ⟨111⟩ and ⟨110⟩ measurements to be included. A systematic deviation is observed between the diamond, silicon and germanium data. However, as shown in fig. I10b, when the effect of vibrational amplitude is taken into account by using the parameter α, the agreement between the three crystals is greatly improved. From fig. I.10b, we see that the angles in germanium are only slightly lower than those in silicon and diamond. The values of α were calculated using the r.m.s. vibrational amplitude (ρ_r) perpendicular to the axis. The values of ρ_r were obtained from existing measurements of the Debye characteristic temperature, according to the procedure outlined by Lonsdale[20] (see Appendix B.2). Note that a 30% change in the value of the Debye charac-

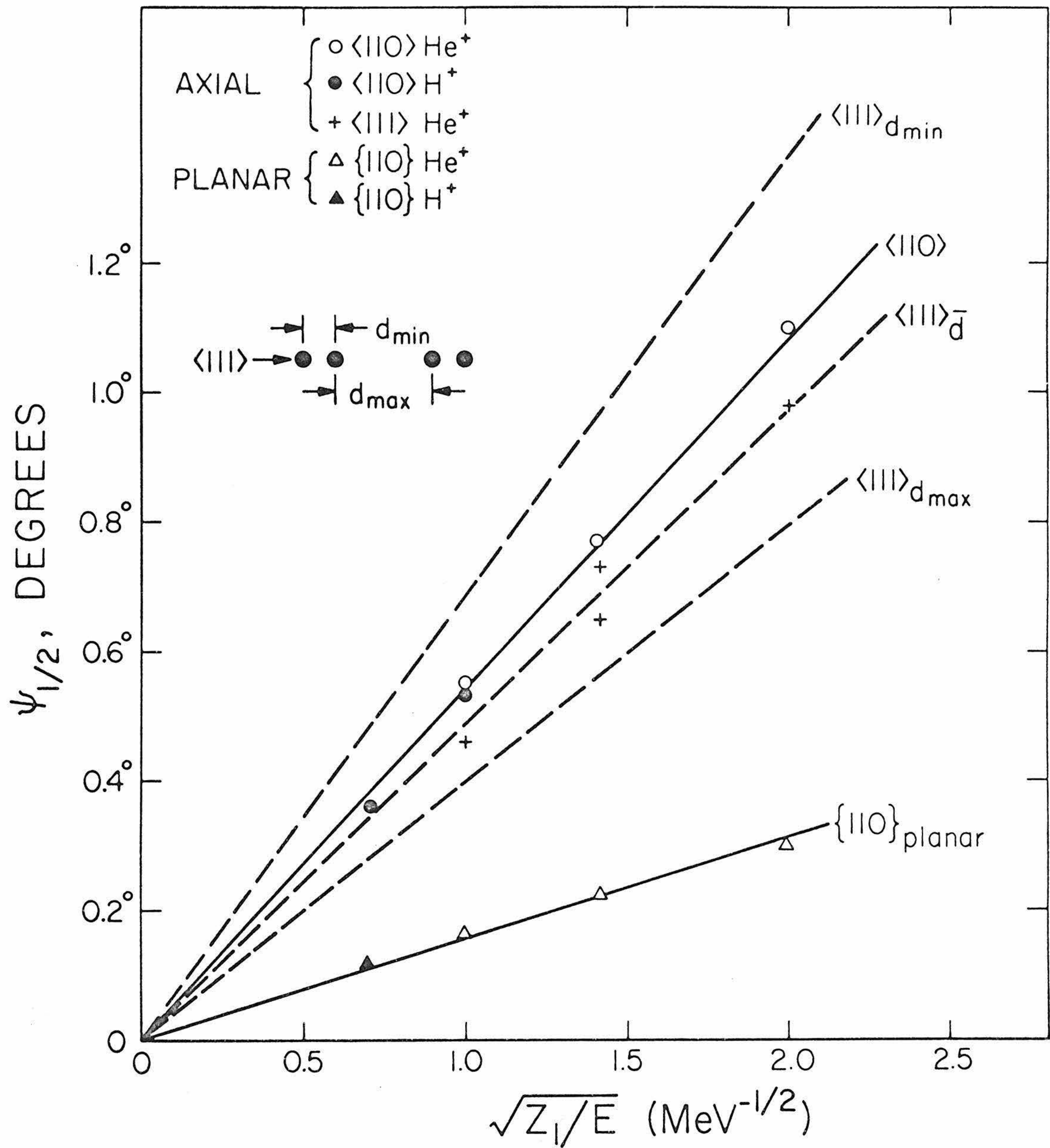

Fig. I.9 The energy (E) and atomic number (Z_1) dependence of $\psi_{\frac{1}{2}}$ in silicon. Solid lines (———) represent best fits to ⟨110⟩ axial and {110} planar data. Dashed lines are calculated from eq. I.2 for the ⟨111⟩ axis from the ⟨110⟩ data using various values for the effective lattice spacing (cf. fig. I.2).

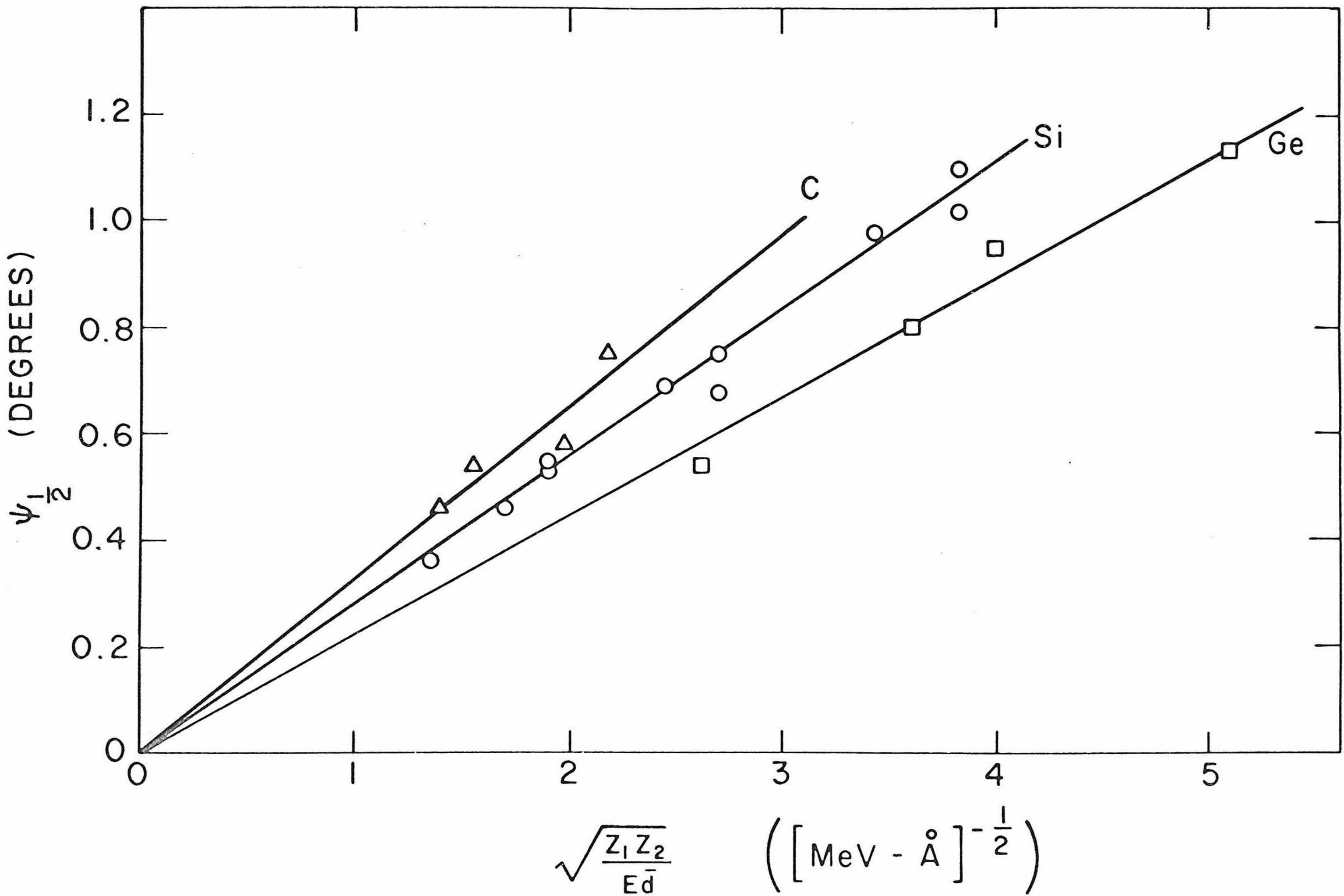

Fig. I.10a The observed functional dependence of axial critical angles ($\psi_{\frac{1}{2}}$) on energy (E), atomic number (Z_1, Z_2) and mean lattice spacing ($\bar{d}$) in various lattices: Δ - C (diamond), O - Si, $\square$ - Ge.

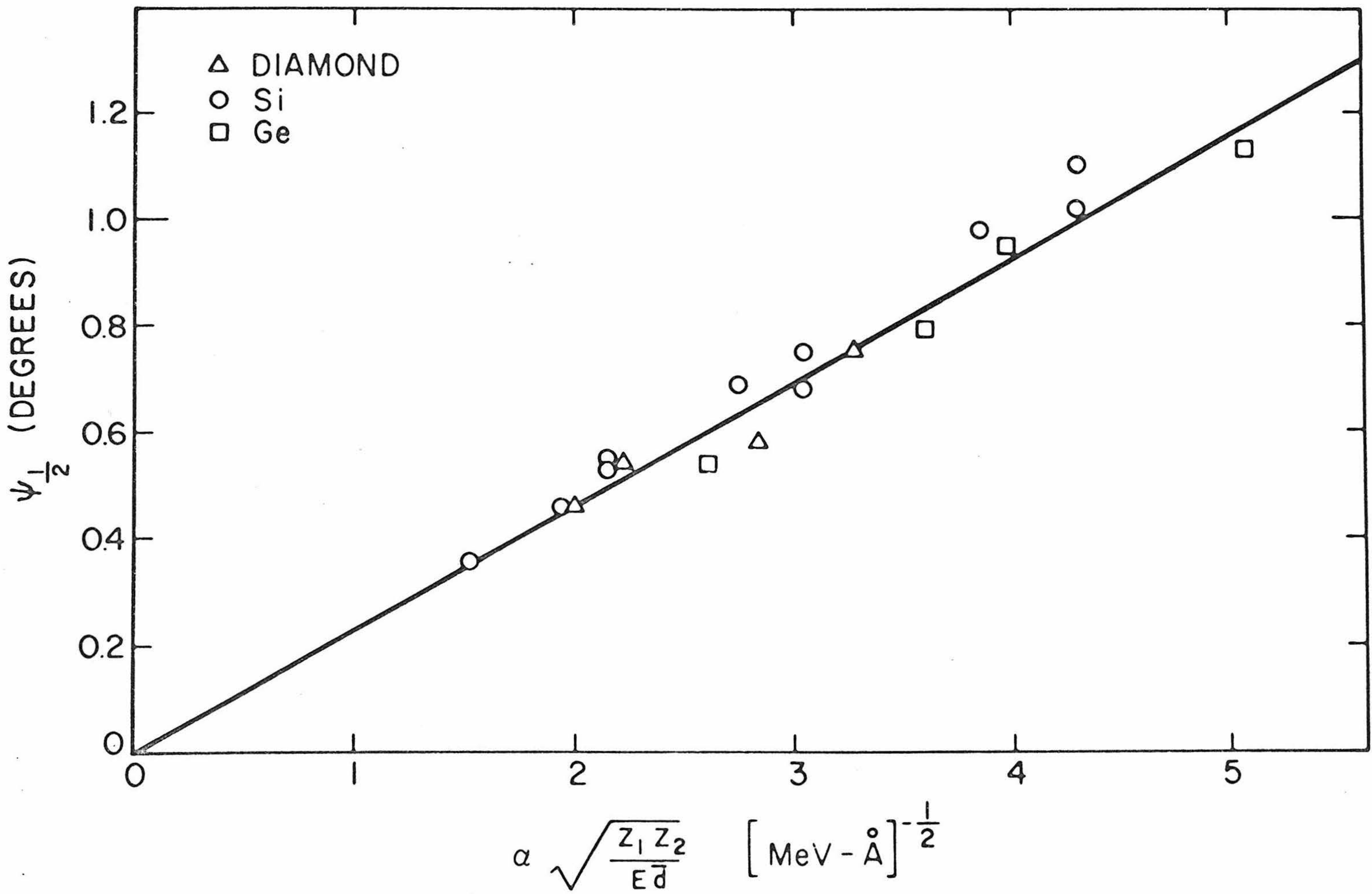

Fig. I.10b As in fig. I.10a but with the effect of thermal vibrations (eq. I.4) included.

teristic temperature produces only a 5% change in the magnitude of α.

I.4.2 $\psi_{\frac{1}{2}}$ Values - Diatomic Lattice. In the compound lattices, we measure only the critical angle for the heavier elements. As illustrated in fig. I.11 for GaP, the end point of the energy spectrum of the lighter elements is lower than that for the heavier element (see Appendix E). This makes it difficult to obtain quantitatively a critical angle corresponding to the scattering yield from the lighter elements.

Axial critical angles measured by backscattering from the compound crystals are shown in fig. I.12. There are two basic cases (fig. I.2): mixed rows containing both atomic species (e.g. $\langle 111 \rangle$), and monatomic rows (e.g. $\langle 110 \rangle$ or $\langle 100 \rangle$). For a mixed row such as the $\langle 111 \rangle$, the steering of the channeled particles is due to the average effect of both types of atoms in the lattice: i.e. the critical angle is obtained using the average atomic number $\overline{Z}_2 = (Z_A \; Z_B)/2$ and the average spacing $\overline{d}$ along the $\langle 111 \rangle$ row. The values of α (Table II) were obtained in the same manner as for the monatomic lattice, using an average value of the Thomas-Fermi screening distance in the case of the mixed rows. The agreement with the monatomic lattices, and hence with the predicted functional dependence on $\overline{Z}_2$ and $\overline{d}$ is seen to be fairly good. The GaAs angles are essentially the same as those obtained in Ge; this is not surprising since the average potential is the same as in Ge.

The $\langle 111 \rangle$ and $\langle \bar{1}\bar{1}\bar{1} \rangle$ critical angles were measured in GaP for 1 MeV helium ions. The anisotropy between these two directions is illustrated in fig. I.2. No significant difference was noted in the measured values for 1 MeV He^+. On the basis of the average potential theory, local anisotropy should not produce significant effects - except perhaps in the

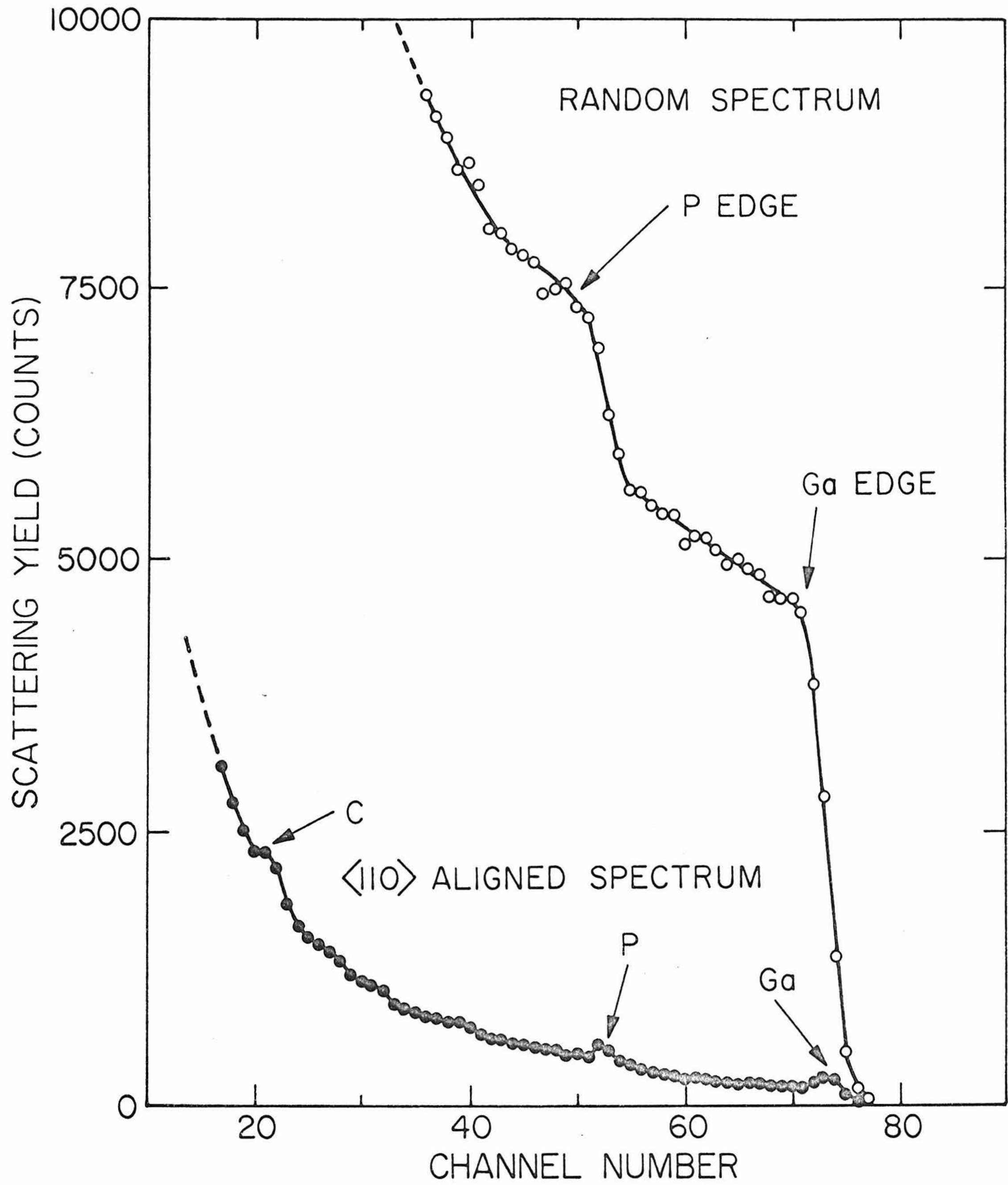

Fig. I.11 Energy spectra for 1 MeV helium ions backscattered from a GaP crystal:
● - beam incident along the ⟨110⟩ axis;
O - beam incident in a "random" direction.

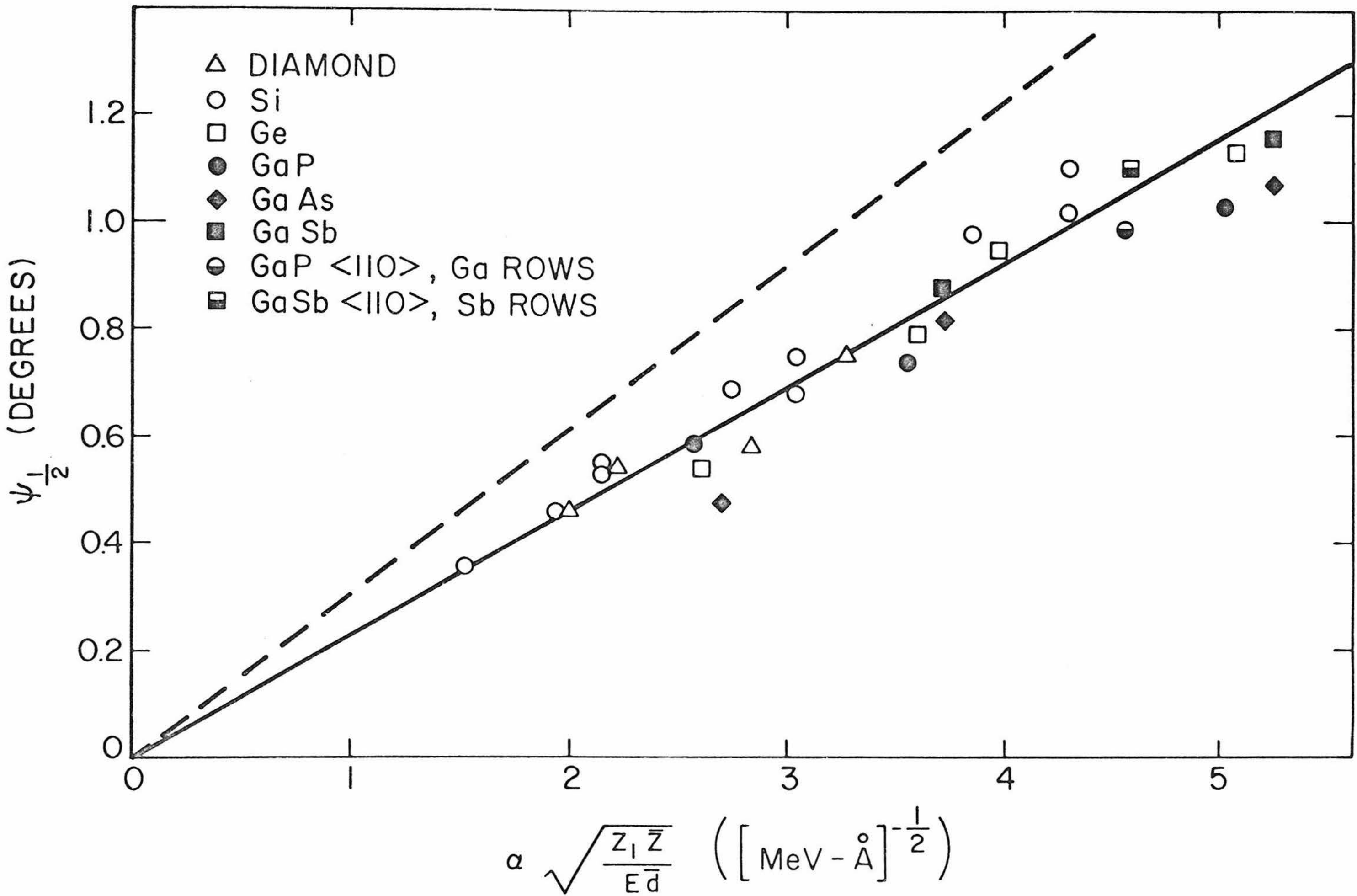

Fig. I.12 The observed functional dependence of axial critical angles in diamond lattice semiconductors for monatomic: C (diamond), △; Si, O; Ge, □ ⟨111⟩ and ⟨110⟩ values. Diatomic: GaP, ● - ⟨111⟩, ◒ - ⟨110⟩ (Ga rows); GaAs, ◆ - ⟨111⟩; GaSb, ■ - ⟨111⟩, ⊟ - ⟨110⟩ (Sb rows). The dotted line is that predicted from eq. I.2.

low-energy region where the continuum potential treatment is no longer applicable: i.e. where $\psi_1 \geqslant a/\bar{d}$. This low-energy region would correspond approximately* to the energy region below 300 keV for helium in GaP.

Along the ⟨110⟩ direction, there are individual monatomic rows of the two types of atoms in the lattice (fig. I.2). Each of these rows is characterized by a critical angle within which it can steer the incident beam. This critical angle is determined by the averaged potential of the individual row. Thus, near the surface, two separate critical angles - one corresponding to each of the two types of atomic rows - should exist. At larger depths in the crystal, the separation between the two critical angles becomes less distinct. Particles that are just within the critical angle of the Z_A row ($Z_A > Z_B$), but that have an angle greater than the critical angle of the Z_B row, will undergo normal multiple scattering by close encounters with the Z_B atoms; this scattering will rapidly cause them to become dechanneled with respect to the Z_A rows also as has been seen in UO_2[22] However, this effect should not strongly influence the present backscattering measurements from the heavier element Z_A, since distances within 1000 Å of the surface can be probed. For GaP and GaSb, $\psi_{\frac{1}{2}}$ ⟨110⟩ values have been measured for scattering from the heavier Z_A elements. These data have been plotted in fig. I.11 using $\bar{Z}_2 = Z_A$. As expected, they show good agreement with the values for the monatomic lattices.

While all the axial critical angles measured for diamond type lat-

---

*The transition from the continuum ($\psi_1 < a/d$) region to the low-energy region is not a sharp one, but extends over an energy region of an order of magnitude as shown by the recent experiments of Bergström et al.[21]

tices exhibit the predicted functional dependence on Z_1, Z_2, E and $\bar{d}$, their average value is about 25% lower in absolute magnitude than one obtains from the theory (dotted line, fig. I.12). To remove the 25% discrepancy would require an increase in the thermal vibrational amplitude of ≈ 0.1 Å for C, Si and Ge. This is equivalent to a value of the vibrational amplitude approximately twice that calculated from Debye temperature values. Calculations by Feldman and Andersen[23] have suggested that the more accurate Moliere potential approximation might reduce the calculated value by $\approx 5\%$. Including the vibration of all the atoms might further reduce the results by another 5%, leaving still a 15% discrepancy between the calculated and observed values in semiconductors. At present we do not understand the reason for this discrepancy between theory and experiment. In tungsten crystals, the reported values of critical angles are in good agreement with calculations based on the same model we have used.

I.4.3 χ_{min} Values. Measured and estimated values of χ_{min} are compared in Table III. For the cases of Si, Ge, GaP and diamond, the observed values of χ_{min} agree reasonably well with the values given by eq. I.11. In the other crystals studied here (GaSb, GaAs), the χ_{min} values are considerably larger than predicted. It should be pointed out that surface contamination, lattice defects, etc., always tend to increase the observed value of χ_{min}. This may perhaps explain why these two crystals (GaAs, GaSb) exhibit values of χ_{min} significantly larger than those given by eq. I.11.

In all cases the observed values of χ_{min} are considerably greater than the estimated lower limit of $Nd\pi\rho_r^2$ (Table III), set by thermal

Table III

χ_{min} Values Along the $\langle 110 \rangle$ Axis
(using 1 MeV H^+ or He^+ beams)

Crystal	Projectile	Rough Estimate of χ_{min}		χ_{min} (Calc. from eq. I.11)	χ_{min} observed
		$Nd\pi\rho_r^2$	$Nd\pi a^2$		
C (diamond)	H^+	.004	.07	.03	.04
	He^+	.004	.06	.03	.05
Si	He^+	.005	.02	.02	.03
Ge	He^+	.005	.01	.02	.03
GaP	He^+	$.004_5$	$.01_5$	.02	$.01_5$
GaAs	He^+	.005	.01	.01	.04
GaSb	He^+	.006	.008	.02	.08

vibrations alone.

I.4.4 Planar Channeling.

$\psi_{\frac{1}{2}}$ Values in Silicon - Surface Transmission Effect. The comparison of critical angles for three different planes in silicon is shown in fig. I.13. By use of {110} oriented crystals and rotations through these planes at 14° from the ⟨110⟩, it was possible to obtain $(\psi_{\frac{1}{2}})_{planar}$ with an accuracy of ± 0.03^{o}. Since the relative magnitudes were of primary importance, the critical angles were all measured in the same sample in order to eliminate any differences between samples due to surface oxide layer or crystal prefection. The {110} $\psi_{\frac{1}{2}}$ values for 1 MeV He in silicon were checked in several samples. The individual planar critical angles (fig. I.13) increase linearly with $(Z_1/E)^{\frac{1}{2}}$, indicating that the predicted functional dependence on atomic number and energy of the projectile is correct.

The dashed curve (long dashes) is a best fit to the experimental {110} $\psi_{\frac{1}{2}}$ values. This dashed line corresponds to a value 0.8 times the calculated value for the critical angles in silicon.* This 20% discrepancy is nearly the same as that observed in the axial case. Using the dashed line best fit to the {110} $\psi_{\frac{1}{2}}$ values in fig. I.13, the relative values for the {100} and {112} directions are determined without surface transmission, $\psi_{\frac{1}{2}} \propto b\sqrt{d_p}$, (solid line). There is good agreement between experiment and theory when the effect of surface transmission is included. Use of the surface transmission factor in this case changes the

*The experimentally derived value of β' is 1.5 whereas the calculated values of β' is 1.9 (using the relation $\beta' = b\beta$ with $\beta = 2.7$ for silicon and the surface transmission factor $b = 0.7$ for the {110} planar spacing in silicon according to the calculation of Andersen outlined in Appendix D).

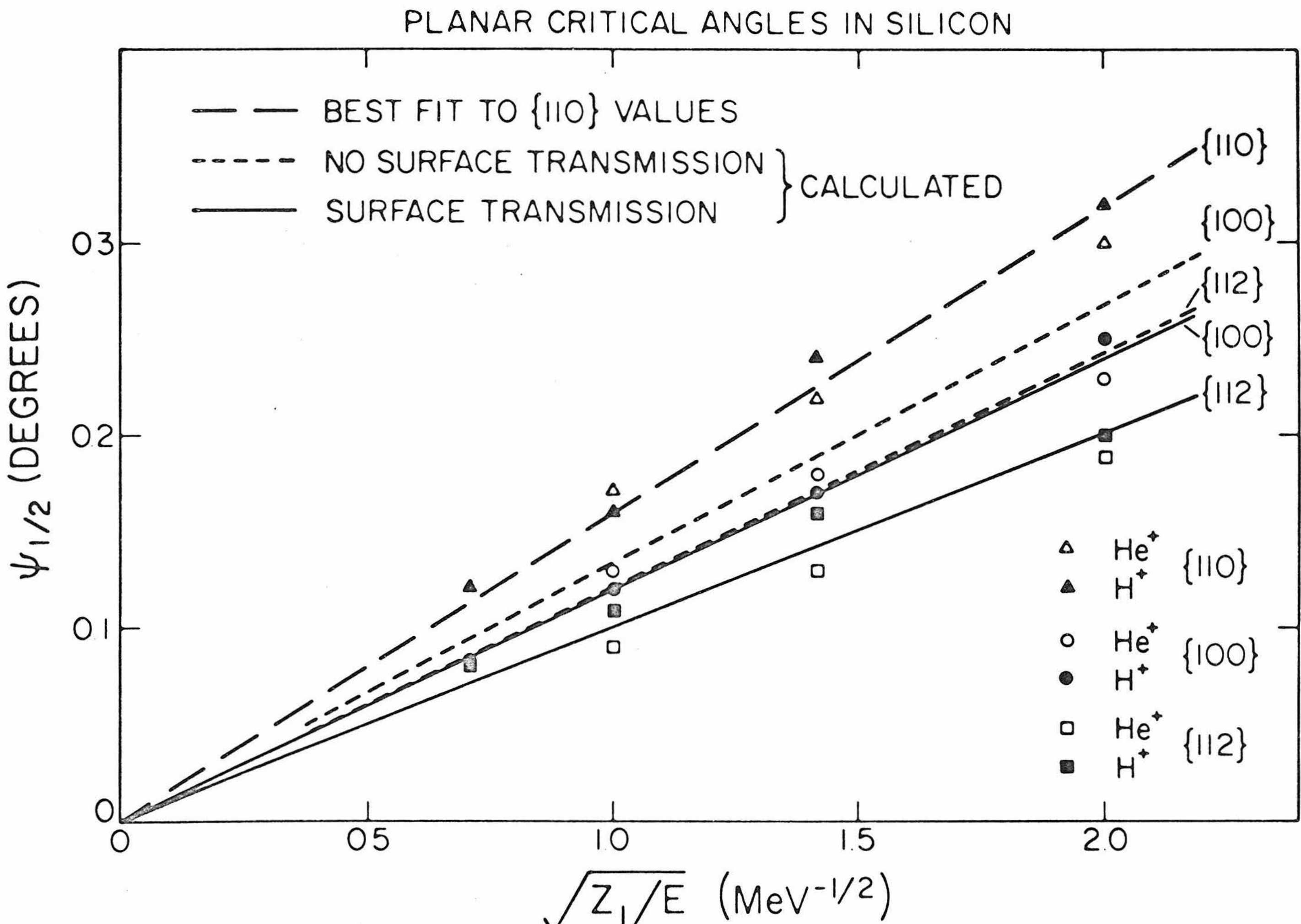

Fig. I.13 Critical angles for several low-index planes in silicon, plotted as a function of $(Z_1/E)^{1/2}$: {110} data - ▲ (H^+), △ (He^+); {001} data - ● (H^+), O He^+); {112} data - ■ (H^+), □ (He^+). The dashed line (long dashes) is the "best fit" to the {110} data; the short dashed lines are the values calculated from the {110} curve without surface transmission ($d_p^{\frac{1}{2}}$ dependence) and the solid lines the values including surface transmission ($b \cdot d_p^{\frac{1}{2}}$ dependence).

critical angle dependence on planar spacing from $(d_p)^{\frac{1}{2}}$ to approximately d_p. Note that any contribution from beam divergence or mosaic spread in the crystal tends to reduce the observed differences between the various planes, and so cannot be used as an alternative explanation to the inclusion of surface transmission.

$\psi_{\frac{1}{2}}$ Values in Monatomic and Diatomic Semiconductors. Critical angles for the {110} plane in various crystals are plotted in fig. I.14 - with the functional dependence of lattice, projectile, and projectile energy incorporated into the abscissa on the basis of the average potential theory. Since the planar spacing d_p is 2.0 ∓ 0.1 Å for all the crystals considered, it was not necessary to include the surface transmission factor in this comparison. The experimental values of $\psi_{\frac{1}{2}}$ for all the lattices can be fitted reasonably well to a single relationship, indicating that the predicted functional dependence (eq. I.6) is obeyed. Similar to that found for the silicon {110} $\psi_{\frac{1}{2}}$ values alone, the solid line of fig. I.13 corresponds to an observed $\beta' = 1.5$.

In trying to fit the data in fig. I.14 to a single relationship, no correction was required* for the variation of thermal vibrational amplitude in the different diamond lattices - unlike the axial channeling case shown in fig. I.10b. For planar channeling, vibrational effects are generally less significant as previously discussed (section I.3). This difference between planar and axial channeling has earlier been observed[9] as a marked difference in "dechanneling" rate as a function of temperature (i.e. of vibrational amplitude). In the axial case, it was

*Note that the planar critical angle measurements will be somewhat less sensitive to a given percentage change simply due to their lower relative magnitude.

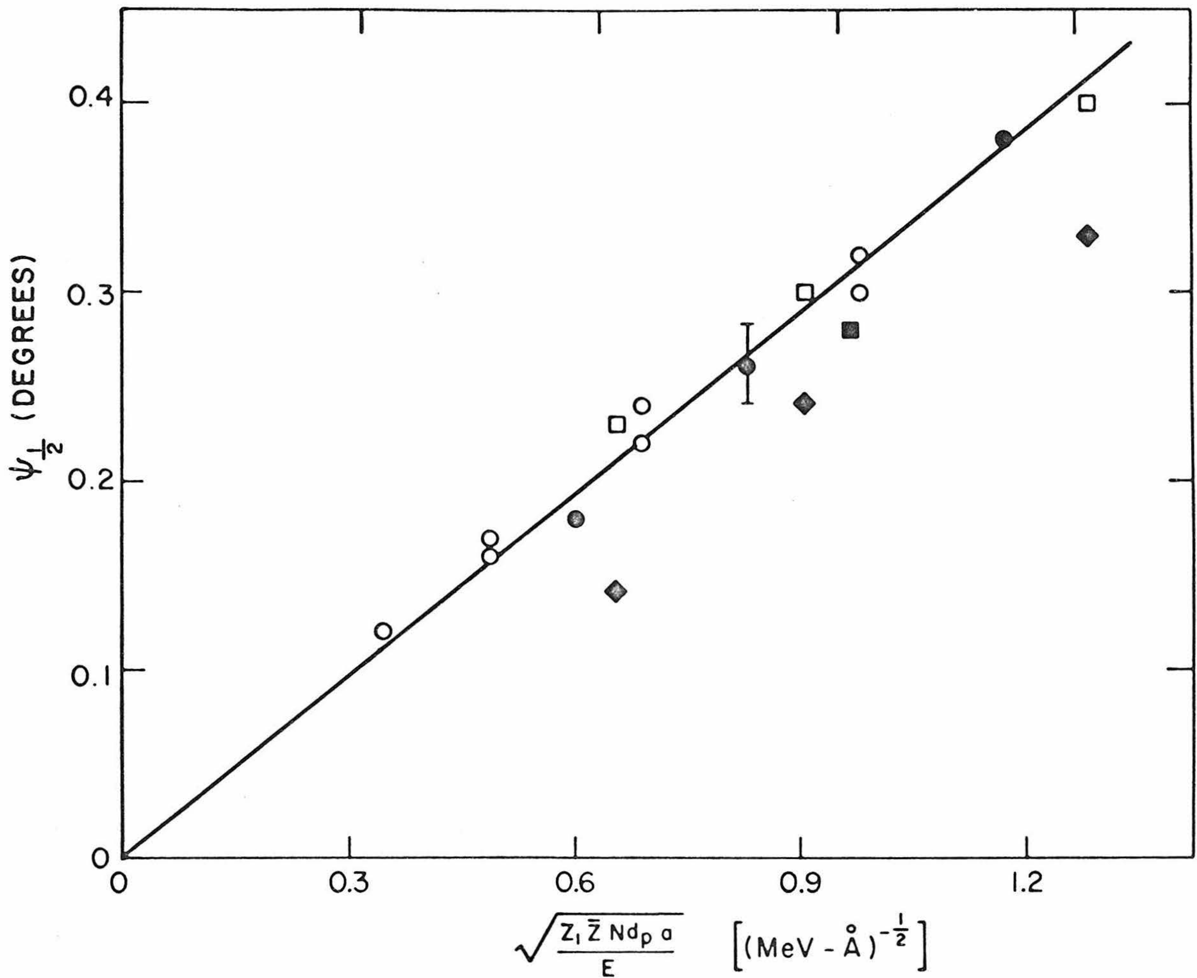

Fig. I.14 The observed functional dependence of $\psi_{\frac{1}{2}}$ for the {110} plane in various semiconductor lattices: O - Si; □ - Ge; ● - GaP; ◆ - GaAs; ■ - GaSb.

found that the dechanneling rate is strongly temperature dependent, but in the planar case, it is almost independent of temperature.

The case of a mixed plane has also been investigated. The {110} plane was selected since the inter-planar spacing is uniform and each plane contains equal numbers of the two atomic species. Thus, a single planar critical angle, based on the averaged potential, should be obtained. Experimental values of $\psi_{\frac{1}{2}}$ are compared with the monatomic results for the {110} plane in fig. I.14 using the averaged atomic number $\overline{Z} = (Z_A+Z_B)/2$. The agreement is quite good for GaP and GaSb. However, the GaAs values are somewhat low; the reason for this discrepancy is not understood.

Angular Distributions. For a more detailed comparison between experimental and calculated results, we will compare the full angular distributions about planar channeling directions. There has previously been only one direct comparison for planar channeling given by Andersen[(14)] for 480 keV protons about the {110} plane in tungsten. The calculated distributions used here follow the methods outlined by Andersen and are described in Appendix D. The integrations were performed numerically by computer to error estimates of $\leq 1\%$. The effects of surface transmission and lattice vibrations are included as discussed section I.3.

Measured and calculated planar channeling angular distributions for 1 MeV He ions about the {110} plane are shown for the monatomic lattices in silicon and germanium in figs. I.15 and I.16. The comparison between experimental and calculated curves for the {110} plane will be discussed in terms of the angular width, minimum yield and shoulders. The shoulders are that region of the curve in which the normalized scattering

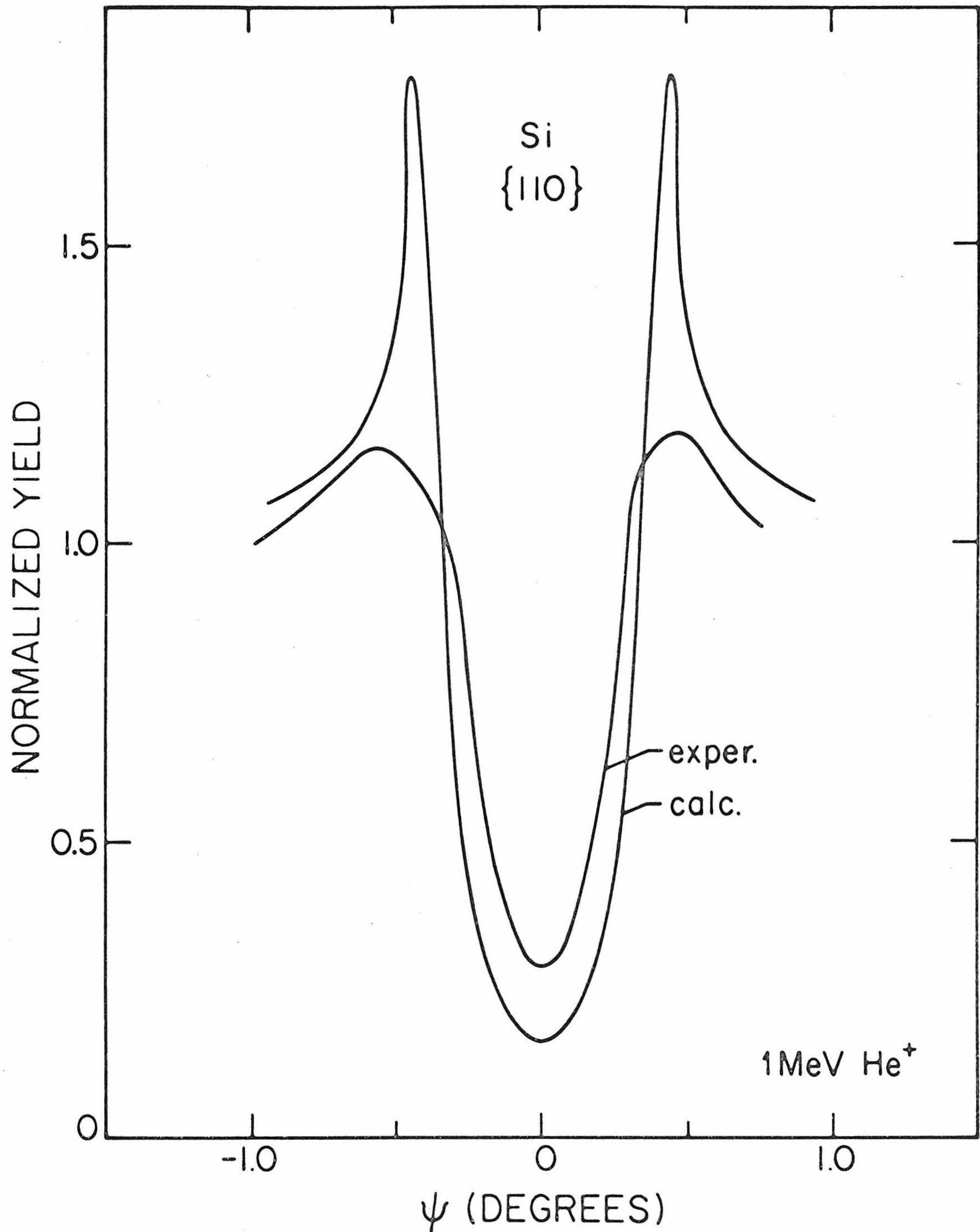

Fig. I.15 Measured backscattering yield and calculated angular distribution for planar channeling of 1 MeV He ions incident along the {110} plane in silicon. The experimental curve is obtained by an automated angular scanning system.

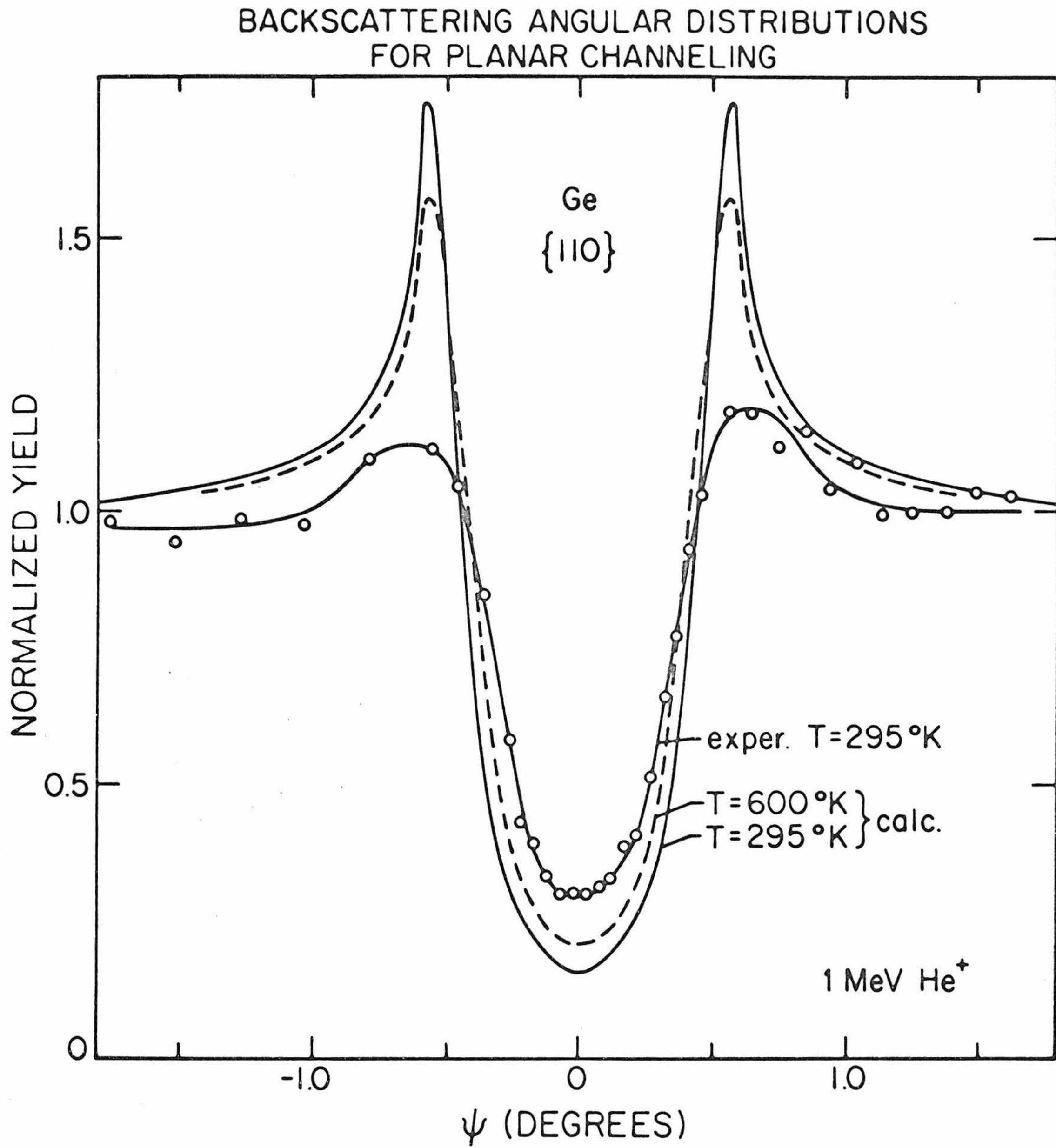

Fig. I. 16 Measured backscattering yield and calculated angular distributions for planar channeling of 1 MeV He ions incident along the {110} plane in germanium. The calculated distributions are for T=295°K (solid line); T=600°K(dashed line).

yield rises substantially above unity.

The angular widths show the best agreement; in each case, the experimentally observed angular widths are slightly narrower than the calculated curves. Comparisons for a number of different diamond lattice semiconductors (Si, Ge, GaP, GaSb) showed the measured planar critical angles to be always lower than the calculated values by about 20 to 25%. This is consistent with the axial channeling results where the observed $\psi_{\frac{1}{2}}$ values were $\approx$ 25% smaller in magnitude than calculated.

The channeling angular distributions do not show as good agreement for the shoulders and the minimum yield as for the angular widths. This can be understood in terms of the limitations of the experimental technique and the assumptions on which the calculation is based. There is always some oxide layer on the crystal (typically $\approx$ 20 Å thick on silicon) through which the beam must penetrate. The minimum yield is quite sensitive to this layer which dechannels an additional fraction of the beam and results in a larger experimentally observed minimum yield.

The initial beam divergence and goniometer accuracy place an angular resolution limit of $\approx 0.04^{\circ}$ on the measurement - a value comparable to the width of the shoulder near the maximum yield. This results in a small smearing effect which would tend to lower the shoulders slightly and make them less sharp. More important is the fact that the planar potential is not in fact smooth and continuous as assumed but made up of discrete atoms. The shoulder region of higher backscattering yields than normal are due to the "focusing" of channeled particle trajectories into the plane (regions of higher atomic density) and are sensitive to deviations from the assumed smooth planar potential. One way to see the

effect of this on the calculation is from the change in the calculated distribution with temperature. This is shown for a change in temperature from $295^{o}K$ to $600^{o}K$ for Ge in fig. I.16. The effect on the angular width is small while the change in the shoulder is more noticeable. Thus, the "roughness" of the potential shows up most strongly in the lack of good agreement between calculation and experiment in the shoulder region. Also we can show that the average potential assumption is not as accurate an approximation for the planar as for the axial case by use of the criteria obtained in Appendix C for $\Delta\psi/\psi$. For 1 MeV helium ions in silicon comparison of $\langle 111 \rangle$ axial and $\{110\}$ planar channeling gives an axial $\Delta\psi/\psi \simeq 0.03$ while for the planar case $\Delta\psi/\psi \simeq 0.2$.

Figure I.17 shows calculated angular distributions for planar channeling of 1 MeV helium ions in silicon for the $\{110\}$, $\{100\}$ and $\{112\}$ planes. This shows the decrease in width and increase in χ_{min} as one goes to higher order planes. Figure I.18 shows the distributions for the same three planes including an angular normalization factor so that the angles are given in units of ψ/ψ_n. In the normalized curves the effects on angular width, other than surface transmission, have essentially been removed through the normalization factor (eq. I.7).. Estimates of the planar channeling angular distributions and critical angles may quickly be obtained from the normalized curves of fig. I.18 for a given set of experimental parameters in the energy region corresponding to $\psi_n < 2Nd_p a^2$. The shape and angular width depend only on vibrational amplitude (ρ), Thomas-Fermi screening distance (a), and planar spacing (d_p). The curves have been computed for a and ρ values for helium atom channeling in silicon at room temperature. These are good as typical

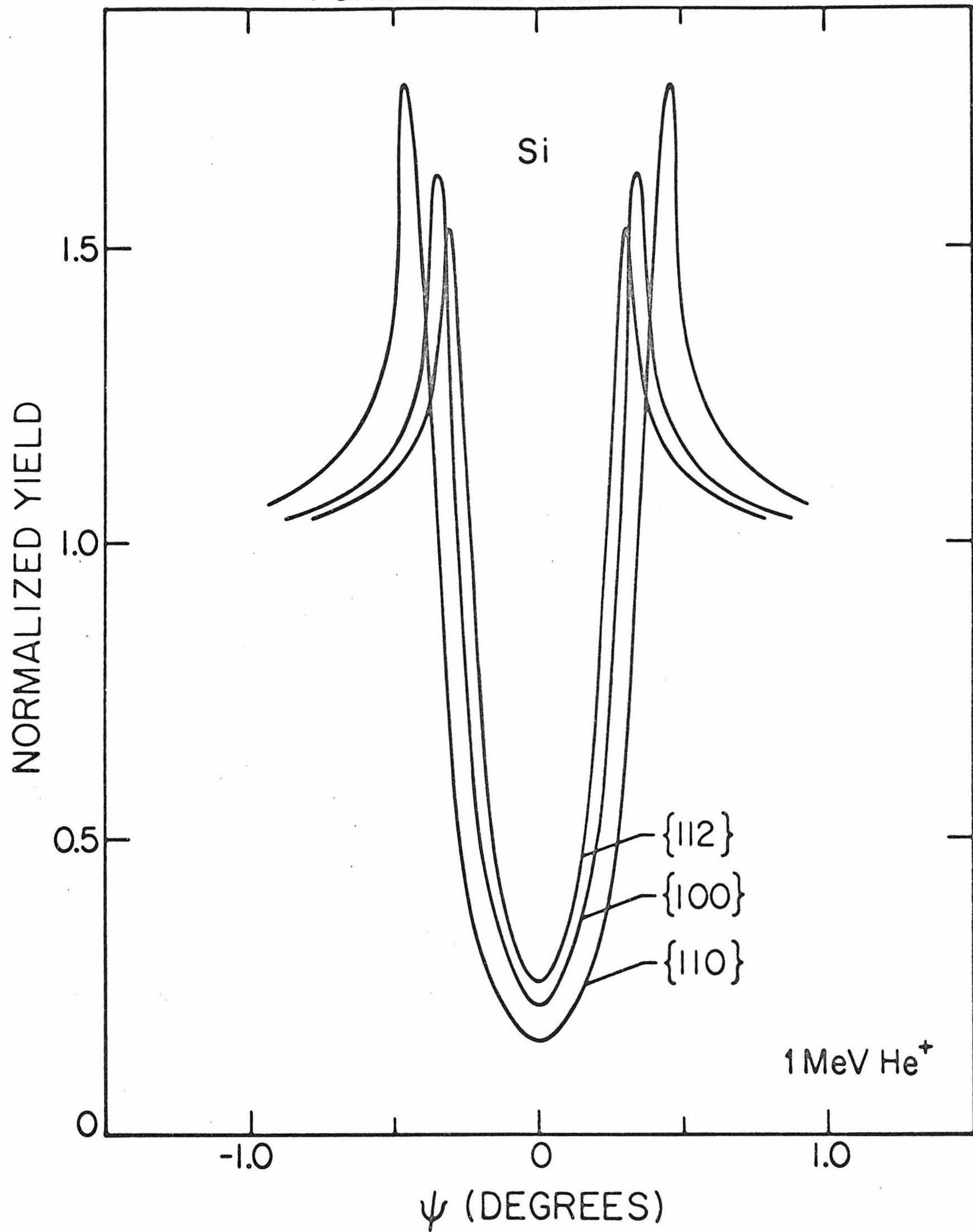

Fig. I.17 Calculated angular distributions for planar channeling of 1 MeV He ions for the {110}, {100}, and {112} planes in silicon.

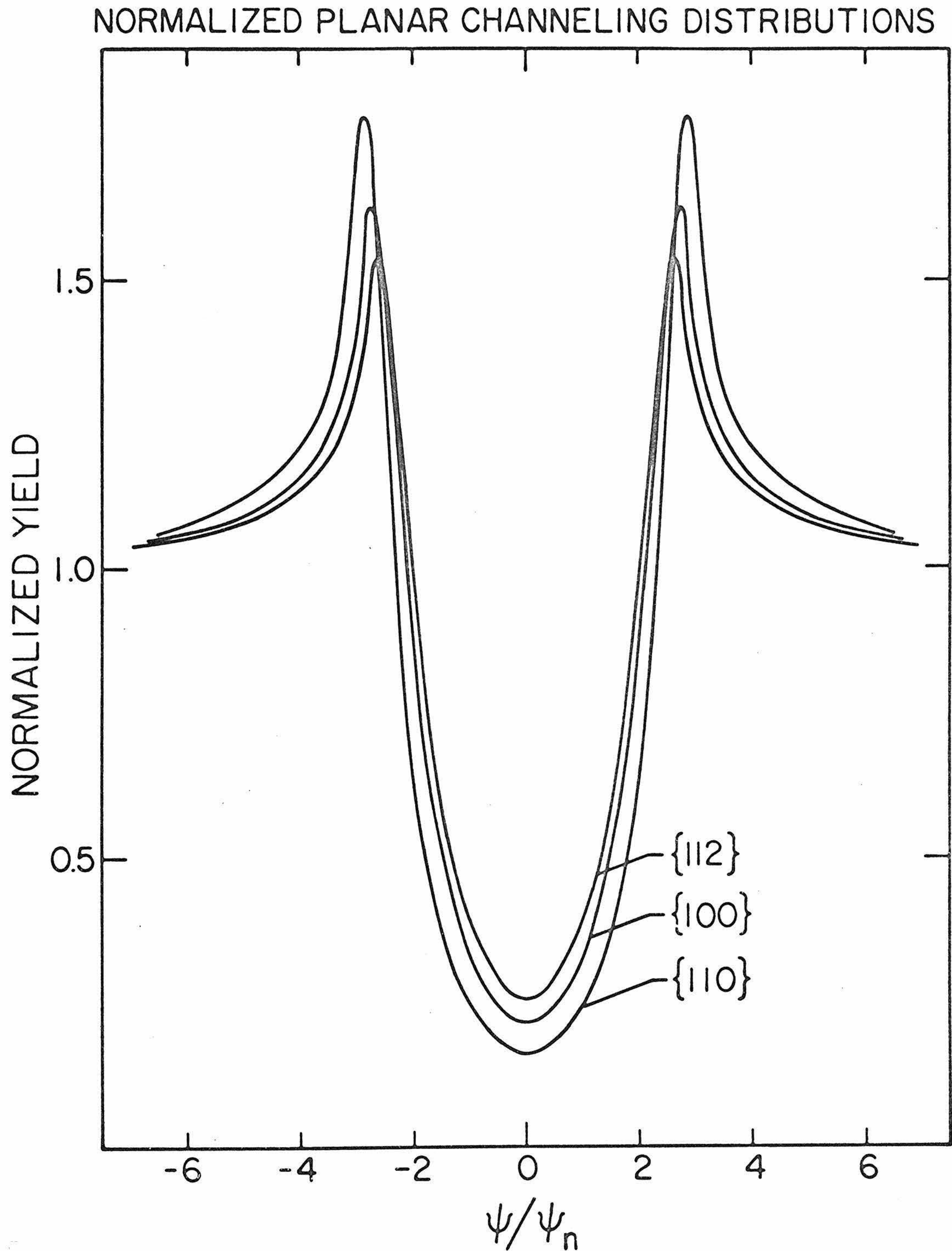

Fig. I.18 As is fig. I.17 except the angular scale has been normalized to obtain generalized curves including surface transmission for the angular width as a function of planar spacing ({110}, {100} and {112} correspond to d_p = 1.92, 1.36, 1.11 respectively).

values since the calculation is only weakly dependent on these parameters. Curves have been given for the planar spacing of the {110}, {100} and {112} planes in silicon (d_p = 1.92, 1.36 and 1.11 Å respectively) to represent a normal range of d_p values. Critical angles for a given crystal, projectile and energy may be obtained from these curves by selecting the value of ψ/ψ_n at which the curve has risen to a level half way between χ_{min} and unity (i.e. the value of β' in the expression $\psi_{\frac{1}{2}} = \beta'\psi_n$). It should be remembered that our experimental results in semiconductors indicate the calculated value for the critical angle near the surface should be further reduced by $\approx$ 20 to 25%.

For higher order planes agreement with the average potential calculations should not be as good since the planar atomic density (Nd_p) is decreasing as the planar width decreases. Fair agreement was obtained for the case of 1 MeV He ions in germanium for the {112} plane (fig. I.19). The shoulders are less pronounced as expected because of the increased roughness of the potential. But in the case of the {112} direction in silicon, the agreement was poorer, particularly with respect to the minimum yield. The calculated distributions about the {100} plane were similar in both germanium and silicon. The angular width and minimum yield differed from the theoretical calculations in a similar manner to that shown in fig. I.19.

Compound semiconductor crystals of the diamond lattice type have also been examined. The comparison of {110} measured and calculated results are shown for 1 MeV He channeling in gallium phosphide in fig. I.20. The results are similar to those for silicon and germanium. This is to be expected since on the basis of the average potential model the

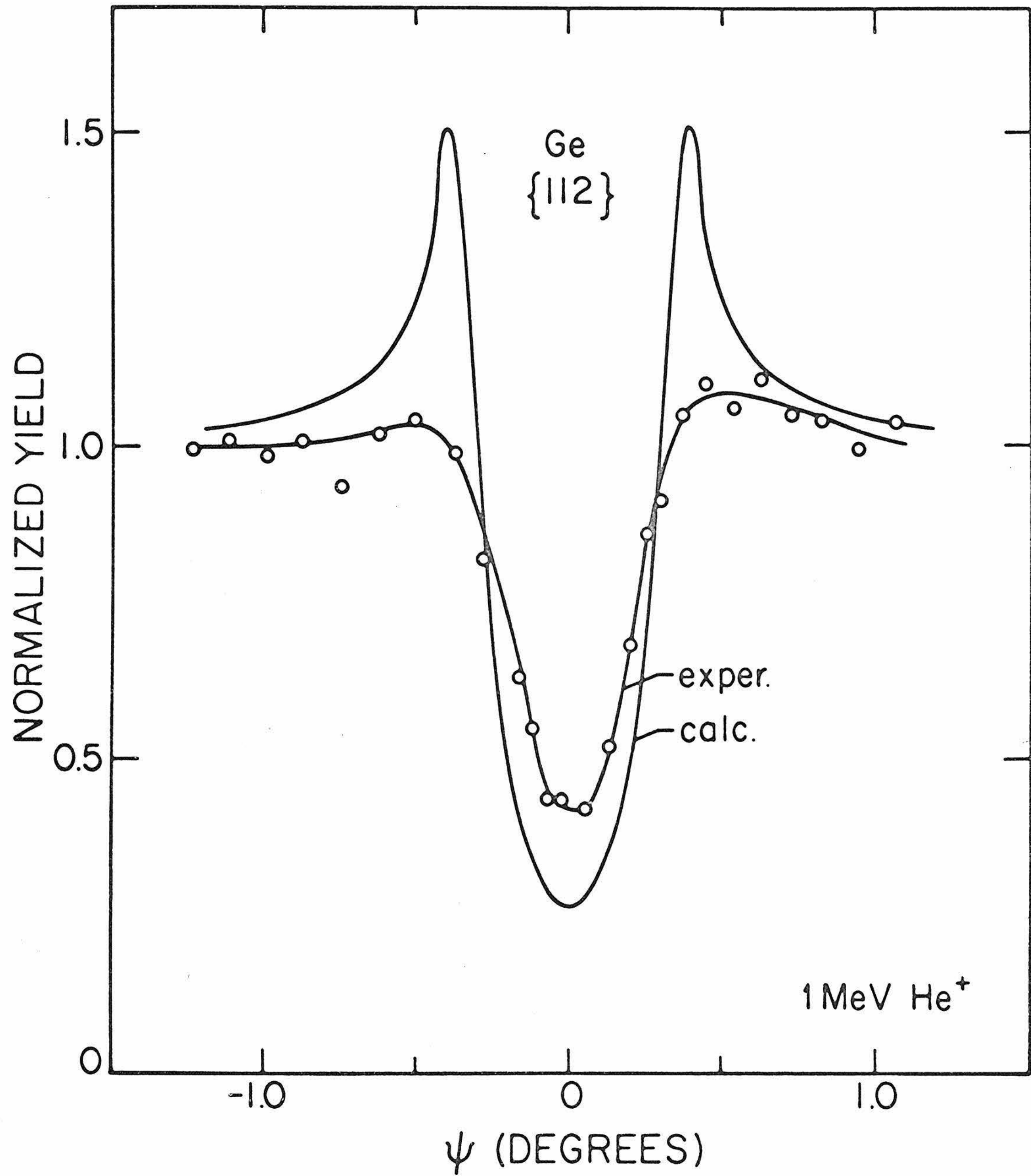

Fig. I.19 Measured backscattering yield and calculated angular distributions for planar channeling of 1 MeV He ions incident along the {112} plane in germanium.

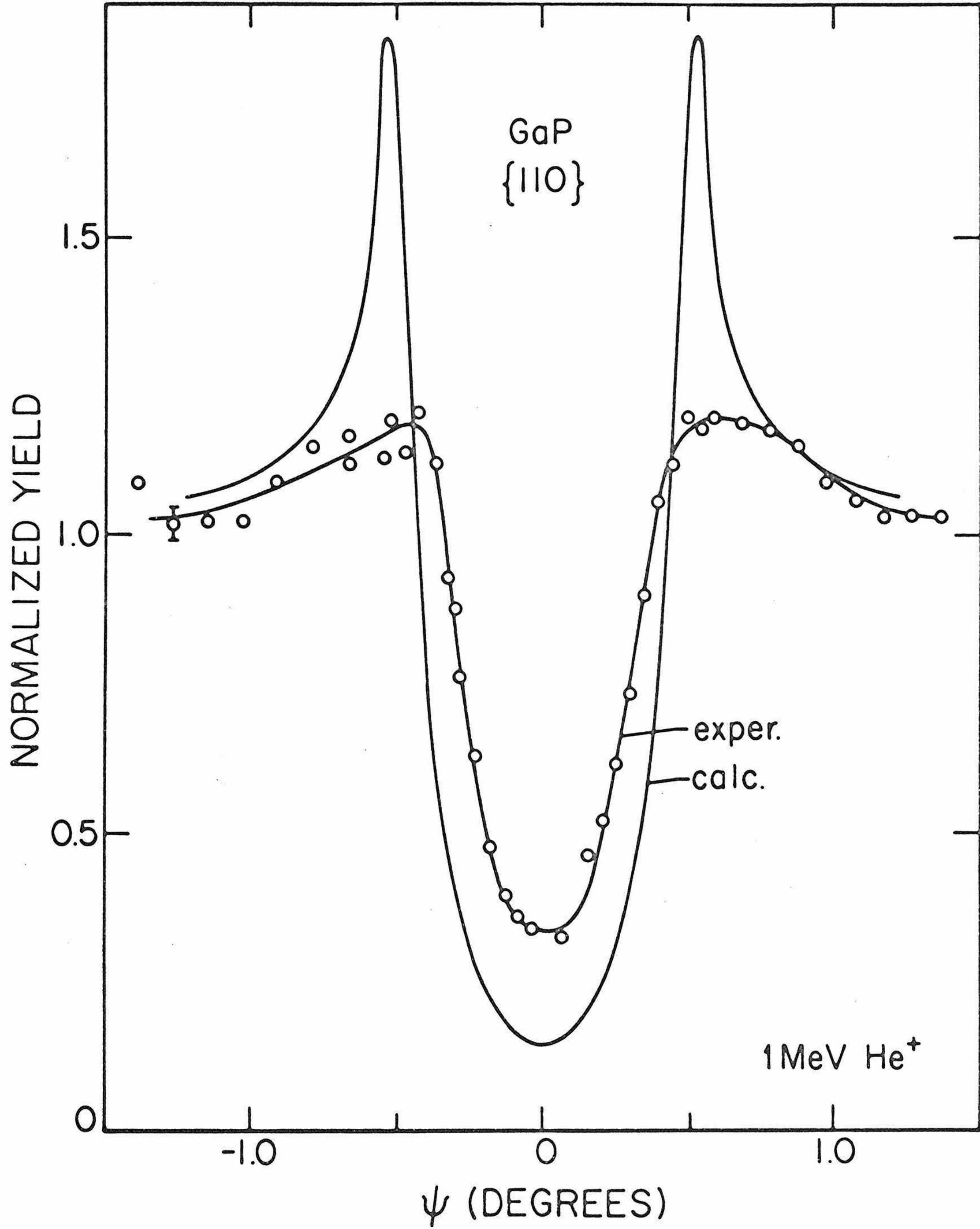

Fig. I.20 Measured backscattering yield and calculated angular distributions for planar channeling of 1 MeV He ions incident along the {110} plane in gallium phosphide.

only change for the {110} planes which contain equal numbers of Ga and P atoms is that the average planar atomic charge density is now given by $Nd_p\bar{Z}e$ where the average atomic number $\bar{Z} = \frac{Z_{Ga}+Z_P}{2}$.

1.5 Summary.

We have investigated proton and helium channeling in diamond type lattice semiconductors, and have measured $\psi_{\frac{1}{2}}$ and χ_{min} values near the surface for comparison with theory. The high energy region (axial $\psi_{\frac{1}{2}} \leqslant a/d$) has been studied over a wide range of lattice parameters.

The axial critical angles have a functional dependence which agrees well with average potential calculations, when the thermal vibrational amplitude of the lattice atoms is included in the calculation. This agreement extends both to uniform and non-uniform atomic spacing and to monatomic and diatomic rows of atoms. For those directions along which the different atomic species lie on separate rows (i.e. $\langle 110 \rangle$), the data indicate that each row steers the incident particles in a manner described by the average potential of that row. For axial channeling, the measured values of the critical angle are approximately 25% lower than the calculated ones. The reason for this discrepancy is not known.

The observed values of the axial minimum yield (a measure of the unchanneled fraction of the beam) agree well with the theoretical estimates in the case of C (diamond), Si, Ge and GaP lattices. In GaAs and GaSb, however, the observed values are significantly larger than expected; this is attributed to a surface effect such as the influence of oxide layers, contamination or lattice imperfections.

Planar critical angles also show good functional agreement with calculated values for different lattice spacings, for a variety of semicon-

ductors, and for monatomic and diatomic planes. In the planar case, however, it is necessary to include the effect of surface transmission which is dependent on planar spacing. To include this effect, calculations of the full angular distributions were performed. The calculated planar channeling angular distributions compare reasonably well with the experimental results. Estimates of the planar angular distribution can easily be obtained from the normalized calculated results for silicon. Similar to the axial case, the observed planar critical angles are lower in magnitude by approximately 20 to 25% from the calculated results.

Chapter II

Applications to the Study of Ion Implantation

II.1 Introduction.

There has been a great deal if interest in the past two decades in the behavior of impurities in semiconductors. Much is presently known about the more standard dopants in silicon, germanium and gallium arsenide. Yet the general understanding of impurity behavior in semiconductors is still quite limited and much of the knowledge has only an empirical basis. To extend the work in this area, one can study the behavior of unconventional dopants in a well characterized semiconductor such as silicon, or one can study a more conventional dopant in some of the less standard semiconductors such as III-V and II-VI compounds. By combining channeling effect measurements with other experiments such as optical or electrical measurements, one has available a powerful method to study the behavior of impurities in semiconductors. A convenient way to introduce unconventional dopant species into the semiconductor lattice is to use ion implantation. To illustrate this concept of the study of impurity behavior in semiconductors, we have examined the behavior of Te and Cd in silicon using channeling effect and electrical measurements.

The channeling effect may be used to study two aspects of ion implantation processes in single crystals. These are lattice disorder[3] and impurity atom location.[1,6] The measurement of these properties by a channeled beam of particles depends on the existence of a forbidden region around the lattice rows (or planes) into which the channeled particles do not penetrate. This forbidden region corresponds to that area around the rows defined by a radius corresponding to the minimum impact

parameter (typically of the order of 0.1 to 0.2 Å) for the steering of the channeled particles by the lattice rows. Thus, one has available a technique to determine whether the atoms in the crystal lie within the forbidden region of the lattice rows or outside these regions (fig. II.1). All that is needed is an identifiable interaction with an impact parameter less than 0.1 Å between the channeled beam of particles and the atoms of interest in the crystal. In this study we have used elastic backscattering of 1 MeV helium ions although other close encounter interactions such as nuclear reactions and inter-shell x-ray production may be selected depending on the particular application of interest. The lattice disorder is investigated by observing the interaction of the channeled particles with those lattice atoms which have been displaced by more than 0.1 to 0.2 Å from the lattice rows. Similarly the location of impurity atoms with respect to the lattice rows may be studied. Measurements are made along several crystallographic directions (e.g. ⟨111⟩ and ⟨110⟩) to distinguish between different well-defined lattice positions (fig. II.1).

Electrical measurements of the Hall effect and sheet resistivity give information on the number of carriers and their mobility in ion implanted samples. However, these results depend both on the implanted ion location and on the amount of lattice disorder or defect centers present. Thus, it is very difficult to interpret the results of these electrical measurements unambiguously. But, by use of channeling measurements, we have a means of independently studying the lattice disorder and implanted ion location. It is for this reason that the combining of these methods has resulted in a very powerful method of analysis of

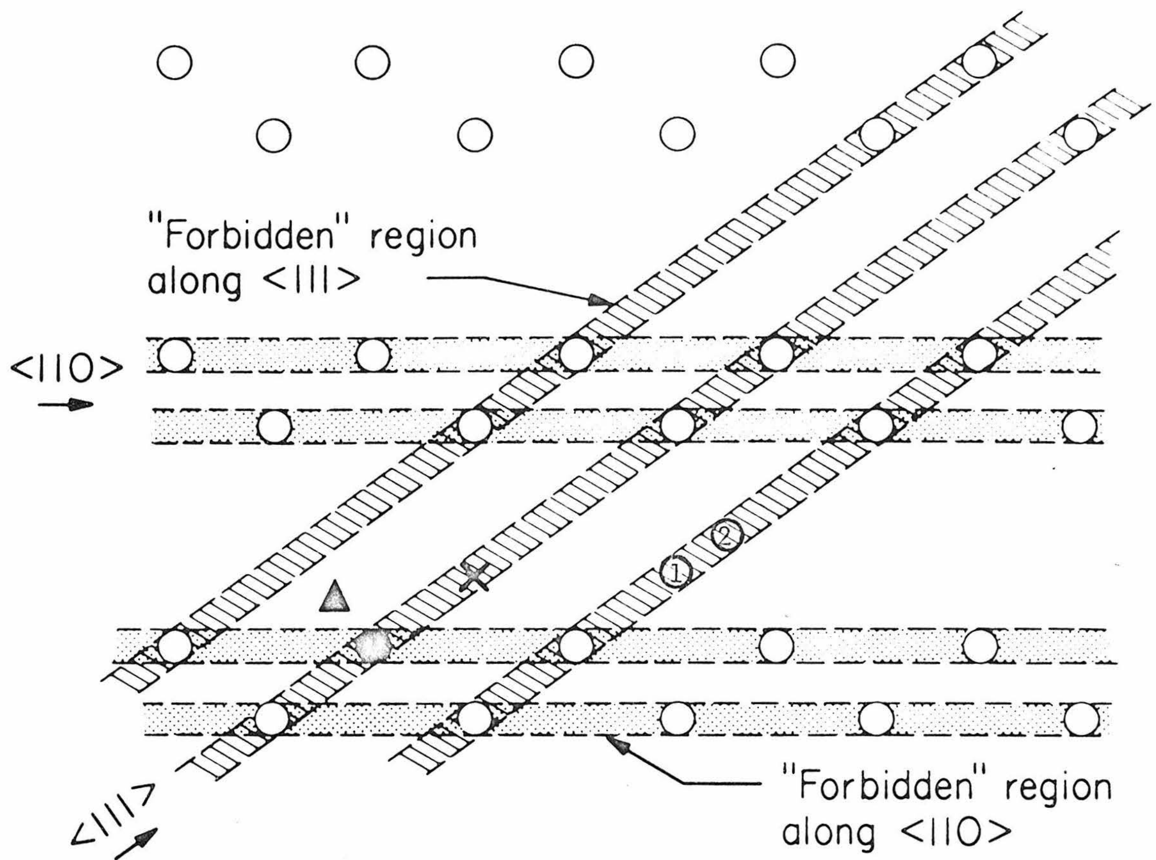

○ - silicon lattice atoms

	Direction Effect		Impurity
	<111>	<110>	
●	yes	yes	substitutional
×	yes	no	"regular" interstitial
▲	no	no	off lattice site

Fig. II.1 Demonstration of the principle of impurity atom lattice location in the silicon (diamond-type) lattice using channeling effect measurements. Positions 1 and 2 show the location of the "tetragonal" and "hexagonal" interstitial sites. Positions 1 and X are equivalent.

ion implantation.[6] In this chapter we demonstrate this approach. This is the first time channeling and electrical measurements have been performed on the same sample to analyze ion implantation phenomena.

Ion implanted samples are easily analyzed by channeling effect measurements because the implanted region is a well-defined thin layer lying near the surface of the crystal. Typical implantations of heavy ions accelerated to keV energies (normally 20-300 keV) result in a disorder region and impurity atom distribution extending in depth to the order of 100 to 1000 Å. This entire layer may be probed with light MeV ions such as He or H because of their greater penetration. The lattice location of implanted atoms can be conveniently studied for implantation doses as low as 10^{13} ions/cm^2 ($\approx 1/100^{th}$ monolayer). For the species and implantation energies used in the present study, this dose represents a concentration of approximately 10^{18} ions/cm^3.

One of the unique advantages of ion implantation for the study of impurity behavior in semiconductors is that the usual limitations on the introduction of impurity atoms into crystals (as by diffusion) may be overcome in a number of ways. The significant points are that substitutional concentrations for standard dopants can often be increased by several orders of magnitude and that a much wider range of elements may be introduced into the crystal.

By the study of the properties of implanted layers, it may be possible to obtain a more general understanding of what factors determine the properties a given dopant will exhibit in a particular semiconductor. There are, of course, limitations to this approach which arise from the

lattice disorder and radiation damage effects* produced by the implanted ions. For a given dopant species implanted in a particular semiconductor, the lattice disorder is generally controlled by the ion dose, the implantation temperature, and any subsequent annealing which may be performed. The first section of this chapter is devoted to lattice disorder studies.

Previous implantation studies[6,24-27] have been focused primarily on the Group III and V elements. In this work we have extended our study of dopant properties to other types of impurities in silicon: Cd, a Group IIB element; and Te, a Group VIA element. The lattice location studies are presented in the second section of this chapter and the electrical properties are discussed in the final section.

II.2 Lattice Disorder.

During implantation lattice disorder is created as the implanted ions come to rest in the crystal. The disorder arises from nuclear collisions in which lattice atoms are displaced, and from the distortion of the lattice defects in the implanted layer. Lattice location of the implanted atoms and the resulting electrical properties of the implanted layer will be strongly influenced by this disorder.[28] Thus, in order to study impurity atom behavior in semiconductors by ion implantation, it is important to characterize the resulting lattice disorder.

In this section the use of the channeling technique to study the disorder is described. The influence of implantation dose and anneal temperature is discussed, and it is shown how implantation at elevated

*For simplicity in this discussion, we will consider lattice disorder as those atoms displaced by $\geqslant 0.1$ Å from their lattice sites. Radiation damage effects refers to electrically active defect centers in the implanted region.

temperatures can be used to reduce the amount of lattice disorder.

<u>II.2.1 Technique</u>. Quantitative information on the amount of disorder is obtained by energy analysis of the yield of backscattered particles for aligned and random beam incidence. In this case, the amount of disorder is a measure of the number of atoms located $\gtrsim 0.1$ Å from lattice sites. Typical spectra for a 1 MeV He beam incident on silicon samples implanted with 40 keV Sb ions are shown in fig. II.2. The energy scale (given in terms of channel number) may be converted to a depth scale (see Appendix E.2). Those particles which are backscattered from the surface have the highest energy (0.575 times the incident energy for 160° scattering of He by Si). Particles which penetrate deeper into the crystal lose energy due to electronic stopping and have a lower energy corresponding to the depth at which they were backscattered. The surface peak (fig. II.2, channels 114-123) corresponds to backscattering from atoms off lattice sites in the disordered region which is ≈ 300 Å thick in this case. The yield obtained from an undamaged crystal is shown by the "undoped" spectrum. The small peak for the undoped spectrum is due to scattering from the silicon atoms in the surface oxide layer. As shown in fig. II.2, the surface peak (disorder) increases with increasing implantation dose. The height of the peak, but not the area, is related to the detector resolution. In spectra shown in fig. II.2, the surface peak for a totally disordered layer (5.4×10^{14} Sb/cm^2) does not rise all the way to the random level because the thickness of the silicon layer (≈ 350 Å) defined by the detector resolution (≈ 22 keV) is greater than the thickness of the disordered region. Note that it is not necessary to consider the attenuation in intensity of the analyzing

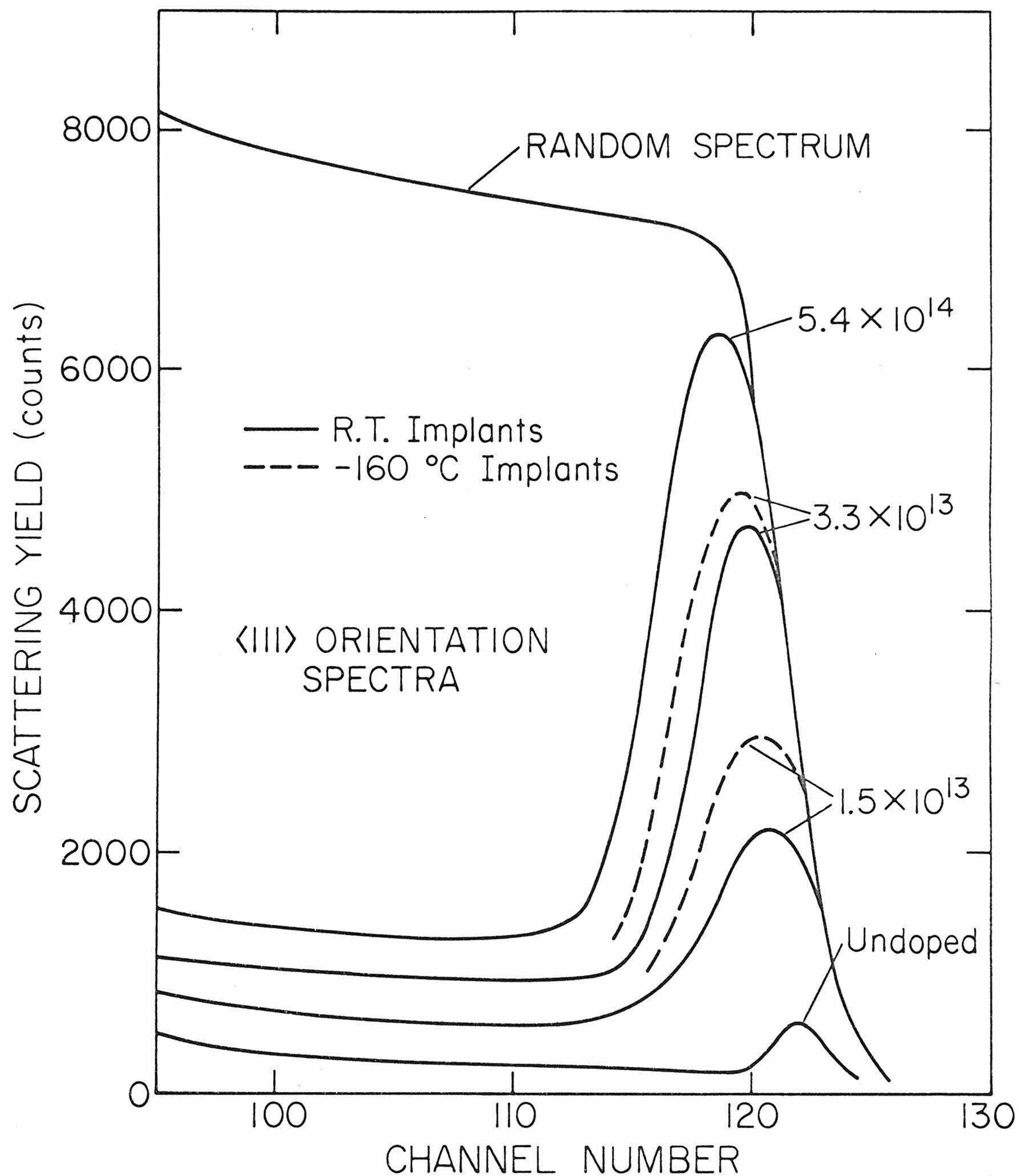

Fig. II.2 Aligned and random backscattering energy spectra for Si crystals implanted at room temperature and -160°C with 40 keV Sb ions. The spectrum from an undoped crystal is included for comparison. Random spectra coincide within statistical counting errors. The analyzing beam was 1.0 MeV He^+.

beam in the analysis since only about 1 in 10^5 of the particles are backscattered in the implanted layer.

The number of displaced atoms is obtained from the same formula used to calculate the number of implanted (impurity) atoms as derived in Appendix E.3. It gives for the number of displaced silicon atoms/cm^2

$$N_{si} = 4.8 \times 10^{18} \frac{A}{E_p \cdot R} , \tag{II.1}$$

where E_p is the channel number corresponding to the end point of the random spectrum (channel 122 in fig. II.2), R is the scattering yield/channel near the surface and A is the number of counts in the surface peak (area of the disorder peak) as shown in fig. II.3. In obtaining the area A of the surface peak, a linear approximation to the background (fig. II.3) forms the basis of a small background subtraction due to the dechanneled fraction of the beam which can interact with those atoms in the implanted layer which are still on lattice sites. The level on the right is taken as the level behind the surface peak of an undoped crystal and the level on the left is the level behind the surface peak of the implanted crystal. The level behind the surface peak (which increases with the increasing amount of disorder) is due to the dechanneling of the aligned beam by the displaced atoms. The dechanneled particles can later interact with lattice atoms on normal lattice sites causing the increased yield. The requirement for a simple linear background subtraction to be valid is that the disordered region be narrow enough and the beam energy high enough for multiple scattering effects in this layer to be negligible.[4] Also a small correction to the area of the disorder peak is made by subtracting the area of the surface oxide peak

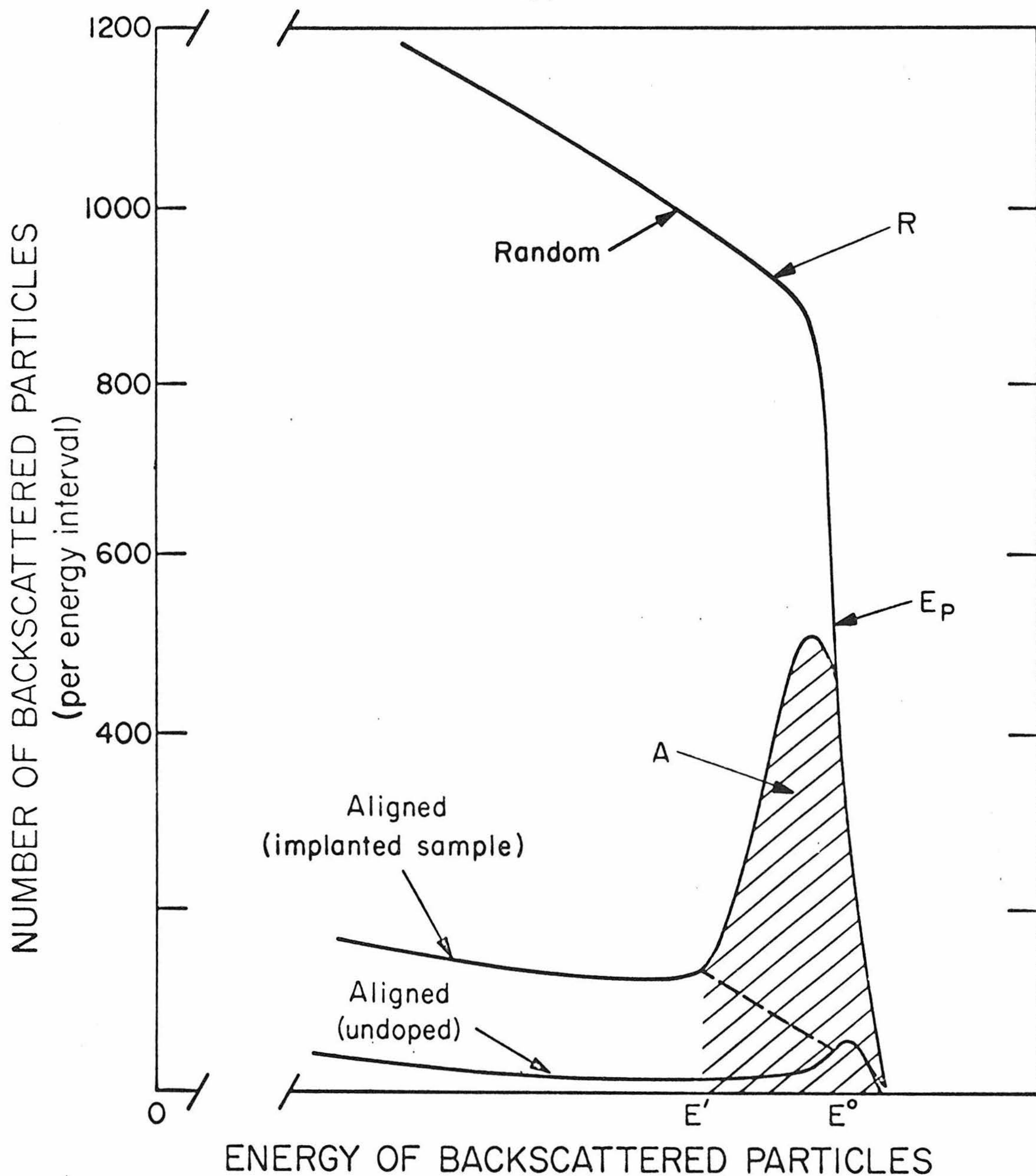

Fig. II.3 Typical random and aligned backscattering energy spectra for implanted and undoped crystals. The energy scale is given in units of channel number. The disorder is calculated from the area of the surface peak A (lined area), the level of the random spectrum R and the end channel of the random spectrum E_p.

for the undoped crystal.

In this study of lattice disorder float-zoned, etch-polished, 100 ohm-cm, p-type Si samples were implanted at Hughes Research Laboratories with a 40 keV, magnetically mass separated and electrically swept Sb ion beam. The Si surface was cut to less than 1° of the ⟨111⟩ face and the surface normal was misaligned by approximately 5° with respect to the Sb ion beam to reduce channeling effects during implantation. The target chamber pressure was less than 5×10^{-7} Torr during implantation. Substrate temperatures were maintained by either radiant heating or conductive cooling, and the temperature of the target was measured to $\pm\ 5^{\circ}$C by a calibrated thermocouple. Secondary electrons were suppressed with a biased shield so that the ion beam current could be accurately measured. The beam current density was typically 10^{-8} amps/cm^{2}. Scattering measurements were carried out on the Caltech 3 MeV Van de Graaff. The energy distribution of particles scattered at an angle $\approx 160^{\circ}$ was measured using a surface barrier semiconductor detector (FWHM $\approx$ 20 keV). Prior to analysis the crystal was aligned to within 0.1° of the ⟨111⟩ axis by the standard channeling technique.

The doses were obtained from current measurements during implantation. For each sample calculations of the dose using the relative intensity of backscattering from Si and Sb atoms (according to the method of Appendix E.3) agreed with the current measurements within the yield of backscattering particles was one of the reasons for the choice of Sb as the implantation projectile.

II.2.2 Results. During implantation at room temperature disordered regions are formed around the track of the incident ion. In earlier mea-

surements[3] we found that the amount of disorder increased linearly with implantation dose until a saturation level was reached. This saturation corresponds to the formation of a completely disordered layer so that no change is observed in the surface peak for heavier doses. Electron microscope studies indicated that the layer was amorphous in the sense that there was no indication of long range order. For heavy ions in silicon (e.g. 40 keV Sb and Ga) the overlapping of the individual disordered regions to form an amorphous layer was complete at a saturation dose of $\approx 10^{14}$ ions/cm^2.

In the isochronal anneal there were two well-defined anneal stages.[2,3] For doses below saturation ($\approx 10^{13}$ ions/cm^2), the disorder annealed at about 260°C. For above saturation doses ($\approx 3 \times 10^{14}$ ions/cm^2) the amorphous layer reordered at 550 to 600°C.

In the present study we investigated the amount of disorder which occurs when the implantation is performed as a function of substrate temperatures. The purpose was to determine the temperature dependence of the annealing which occurs during implantation. Low dose implantations (≈ 1 to 3×10^{13} Sb ions/cm^2) were used so that the amount of disorder was insufficient to form an amorphous layer over the range of implant temperatures investigated. If a saturation dose was reached our technique would be insensitive to any further increase in dose. Previous channeling studies[6] of the temperature dependence of lattice disorder have investigated the higher dose region ($> 10^{14}$ ions/cm) at substrate temperatures greater than 150°C.

Low dose implants were studied for implant temperatures ranging from -160°C to 200°C. Figure II.4 shows the disorder per ion as a func-

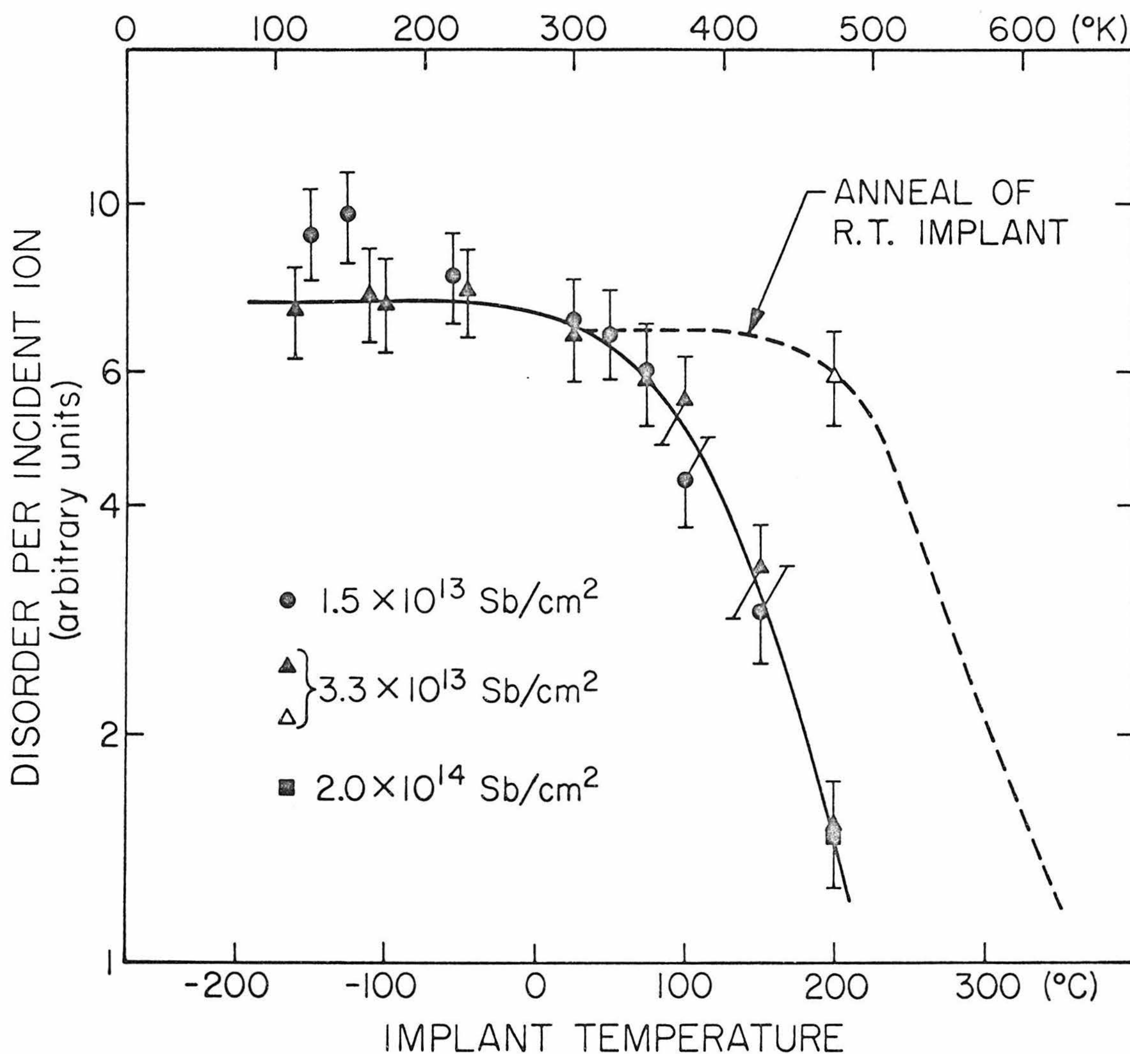

Fig. II.4 Disorder per incident 40 keV Sb ion vs. Si substrate temperature during implantation. The dashed line is the anneal[2] of a room temperature implant of $\approx 10^{13}$ 40 keV Sb ions. The open point represents the disorder in a sample implanted at room temperature and annealed to 200°C in the implantation target holder. The error bars represent the uncertainty in dose measurement.

tion of implant temperature as well as the anneal characteristics of a low dose, room temperature 40 keV Sb implant.[2] One room temperature implant was annealed in the implantation target holder at 200°C for comparison with the anneal data. An implant with a factor of 10 higher dose rate (2×10^{12} ions/cm^2-sec) was made at 200°C to determine if the amount of disorder was strongly dose rate dependent. Both points agreed with previous measurements. The area of the damage peak was approximately the same for ⟨111⟩ and ⟨110⟩ spectra indicating that the displaced Si atoms were <u>not</u> sitting on the regular interstitial lattice sites.*

The samples implanted at temperatures below room temperature were stored in liquid nitrogen, but the measurements were made after the sample had been at room temperature for about one hour. Subsequent measurements two to three days later showed no appreciable change in the amount of damage. Although some annealing may have taken place between implantation and measurement, the anneal characteristics of 23°C implantations (fig. II.4) suggest that this is unlikely. The point in fig. II.4 for the -160°C implant of 3.3×10^{13} Sb ions/cm^2 gives a further indication that the disorder created in this $T < 50°C$ region is not strongly temperature dependent. If the rate of increase of disorder per incident ion continued to increase linearly at low temperatures as it does for $T > 50°C$, the damage layer would be amorphous at -160°C for 3.3×10^{13} Sb/cm^2. Such a layer would not anneal until temperatures around 600°C.[2] The formation of such a layer is not observed.

Approximately 3300 off lattice sites Si atoms per incident Sb ion

---

*For discussion of the lattice location technique, see section II.3.

(6.8 on the ordinate of fig. II.4) remain after a 23°C implantation. A similar result was found earlier.[2] It should be noted that this number is about a factor of 2 greater than the number of displaced atoms calculated by Sigmund[29] on the basis of a well-defined displacement threshold energy. However, lattice distortions greater than 0.1 to 0.2Å around the defects might account for this difference. For example, Watkins[30] has estimated that the six nearest neighbors of the divacancy are displaced by approximately 0.25 Å.

The temperature dependence of the disorder per incident ion is characterized by two regions. For implants in the region above 50°C, the amount of disorder/ion varies rapidly with implant temperature and is independent of ion dose (in the dose region in which an amorphous layer is not formed). In the lower temperature region ($T < 50°C$), the disorder per incident ion was only mildly temperature dependent. This disorder level is clearly below the level resulting when an amorphous layer is formed. At the lowest implantation temperatures, the data suggest that the disorder/ion may be dose dependent.

Note that the region in which the disorder/ion decreases strongly with temperature is approximately 100°C <u>lower</u> than the region of corresponding decrease in the anneal of a low dose room temperature implantation. This difference indicates that even at low doses the dynamic anneal occurring during implantation is not equivalent to anneal after the damage regions have been formed.

To reduce the amount of lattice disorder for impurity atom studies, one has the option of implanting either at elevated substrate temperatures or at room temperature and performing a post-implantation anneal at

a higher temperature. It should be emphasized that this measure of disorder alone does not imply that further annealing will not be needed to obtain the best electrical activity in the implanted layer. For example, a defect concentration comparable to the implanted dose could have a large effect on the electrical behavior and still would not be observable by the channeling technique. Thus, while the channeling effect measurements are a powerful tool for the study of disorder as with any method, it alone should not be considered as sufficient for the understanding of radiation damage.

II.3 Lattice Location of Impurities.

The technique of lattice location of impurities by means of channeling measurements[1] is similar in principle to the study of lattice disorder. In the first section II.3.1 we discuss the technique using backscattering of a 1 MeV helium ion beam. Important limitations to be considered are the difficulties of unambiguous lattice site location for interstitial impurities and the sensitivity of the measurement.

In our study of impurity atom behavior in semiconductors, we have adopted the first of two approaches suggested in the introduction to this chapter - the study of unconventional dopants in a well characterized semiconductor. In the results section (II.3.2), the lattice location properties of Te and Cd implanted into silicon are investigated. Silicon was the natural semiconductor substrate to choose since we have the largest background of information about impurity behavior (introduced both by diffusion and ion implantation) for this material. Also we have the necessary preliminary experience in the lattice disorder properties of ion implanted silicon. The reason for the selection of Cd and

Te is that very little was known about the behavior of these impurities in silicon. They lie next to the more commonly studied Group III and V column impurities (Cd being IIB and Te VIA) and are difficult to introduce into the silicon lattice by any means other than ion implantation.

II.3.1 Technique. In this study the lattice location of Te and Cd in silicon was analyzed by the channeling effect measurements with a 1 MeV helium ion beam. The relative backscattering yields are measured for the beam aligned with a low order crystallographic axis and the beam incident along a random direction. Similar to the lattice disorder studies the channeled beam can interact only with those impurity atoms lying further than the channeling minimum impact parameter ($\approx$ 0.1 Å) from the lattice rows. Energy analysis of the scattering yield allows separate identification of scattering interactions with the lattice and the heavier impurity atoms. This allows the study of impurities over regions near the surface, extending in depth beyond the implanted layers used in this work.

It can be seen from fig. II.1 that measurements along the ⟨111⟩, ⟨110⟩ and random directions in the silicon diamond type lattice allows one to distinguish between atoms located: i) on substitutional sites, ii) on regular interstitial sites along the ⟨111⟩ rows, and iii) on positions displaced $\approx$ 0.1 Å from both these sites.

An example of channeling data for a substitutional atom is shown for the case of Sb in silicon in fig. II.5. In this case the implantation was done at room temperature and then annealed to 800°C. The attenuation in the scattering yield from the Sb is $\approx$ 90% for both the ⟨111⟩ and ⟨110⟩ directions compared to the random yield. This

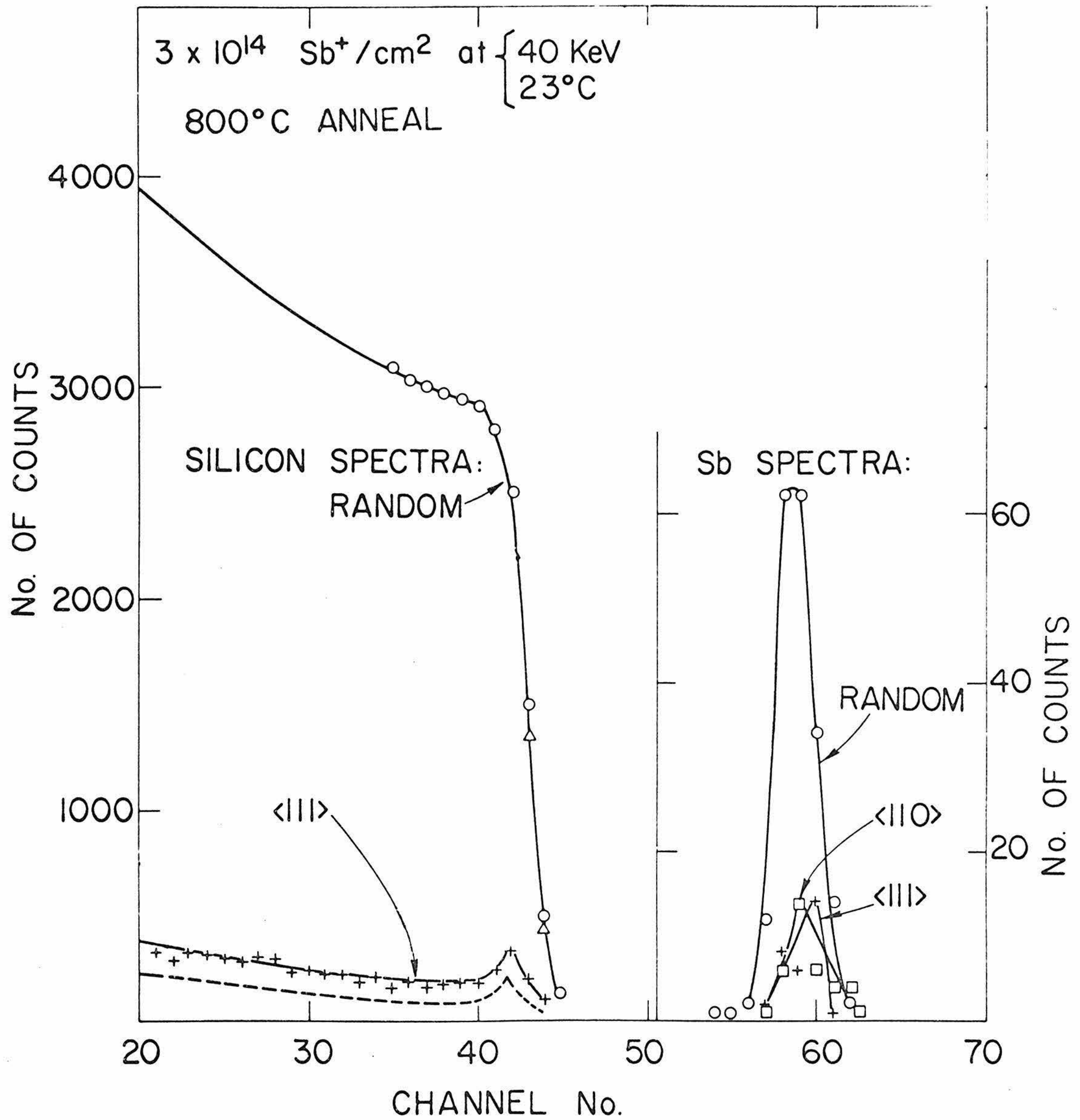

Fig. II.5 Random, ⟨111⟩, and ⟨110⟩ backscattering energy spectra using 1 MeV He^+ for a 40 keV R.T. Sb implantation in silicon after annealing to 800°C.

attenuation* implies that $\approx$ 90% of the Sb atoms lie along both these crystal rows indicating that Sb is a highly substitutional species in silicon.

Another example of ion location data is given for Te in silicon in fig. II.6. The Te spectra show roughly equal attenuation of $\approx$ 60% in the scattering yield for the $\langle 111 \rangle$ and $\langle 110 \rangle$ directions. We interpret this to mean that 60% of the Te are on substitutional sites and the remaining 40% are elsewhere (as precipitation sites, etc.,). However, an alternative interpretation which cannot be ruled out would suggest that this is a lower limit on the per cent substitutional. For the case when all the impurity atoms were substitutional but were strained off of the lattice site position by $\approx$ 0.1 Å then on the average only a fractional amount would be shielded from the channeled beam. For example, this might be due to the differing of the equilibrium covalent bond lengths established between the substitutional impurity and the lattice atoms from the normal covalent bond lengths of the lattice atoms. Without thermal vibration of the impurity atoms, one would not expect to observe an intermediate attenuation from this effect. This follows because the radius of the cross section for elastic backscattering is only of the order of 10^{-5} Å and thus the probability is small that an atom will lie within 10^{-5} Å of the edge of the forbidden region. However, if

*The attenuation is calculated by $\left[(A_r-A_a)/(A_r-\chi_{min}\cdot A_r)\right]\cdot 100$ where A_r and A_a are the summation of the scattering yield (counts) in the impurity peak for random and aligned orientations and χ_{min} is the minimum yield near the surface for the lattice atoms. The factor $\chi_{min}A_r$ results from the fact that even if all the impurity atoms all lie along the row there will still be a small scattering from them just as from the crystal lattice, due to the dechanneled fraction of the beam (χ_{min}). This correction is generally insignificant.

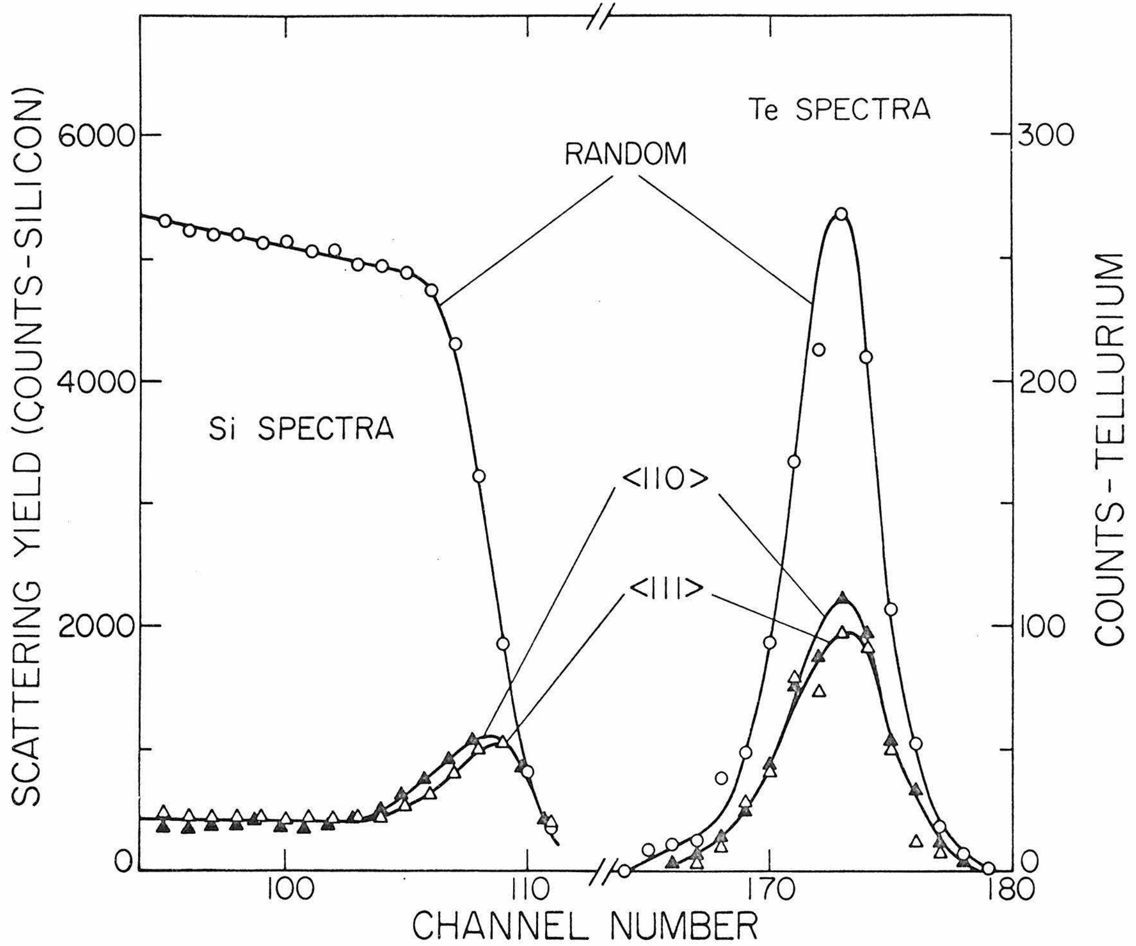

Fig. II.6 Random, ⟨111⟩, and ⟨110⟩ backscattering energy spectra using 1 MeV He^+ for a 50 keV R. T. Te implantation ($8 \times 10^{14}/cm^2$) in silicon after annealing to 650°C.

the thermal vibrations of the impurity atoms around their mean equilibrium position are included, the transition region between the forbidden region and the region outside where the channeled beam can interact with the impurity atoms is much larger. It should be emphasized, however, that for either of these two interpretations the substitutional level is not less than the observed attenuation along the ⟨111⟩ and ⟨110⟩ directions.

A detailed analysis of the percentage of atoms on a particular interstitial site is somewhat more difficult. As a general rule of thumb, one may obtain quantitative information on interstitial location only for very high order symmetry positions. As an example, we consider two positions which have been proposed[31] as interstitial sites for impurities in the silicon diamond type lattice. These are labeled in fig. II.1 as 1, the "tetragonal" interstitial site, and 2, the "hexagonal" interstitial site. There are four non-equivalent ⟨111⟩ directions and position 1 lies at the intersection of all four of these directions. Thus, for the case when all the impurity atoms were in this tetrahedral interstitial position, one would obtain 100% attenuation in the scattering yield along the ⟨111⟩ direction and 0% attenuation along the ⟨110⟩ direction. However, position 2 lies only along one of the four non-equivalent ⟨111⟩ directions. So for the case of all the impurity atoms being in the hexagonal interstitial sites only a 25% attenuation would be observed along the ⟨111⟩ and again a 0% attenuation along the ⟨110⟩ direction. So, for example, in the case of a 25% ⟨111⟩, 0% ⟨110⟩ attenuation result, one cannot distinguish between the two sites without measurements along other crystal directions. In the present work, measure-

ments were made only along the ⟨111⟩ and ⟨110⟩ directions and we will use per cent interstitial to define the lower limit of the number of atoms along the ⟨111⟩ rows.

An advantage of this technique of studying lattice location is that one obtains a measure of the number of impurity atoms (atoms/cm^2) at the same time. The method of calculating this from the relative yields of the impurity and lattice atoms is given in Appendix E.

Using a 1 MeV helium beam, the lower limit to the number of impurity atoms in silicon which can be detected with adequate scattering statistics for lattice location analysis at present is $\approx 10^{14}$ atoms/cm^2 for As to $\approx 10^{13}$ atoms/cm^2 for Bi (yield $\propto Z_2^{\ 2}$). This corresponds to 10^{-3} to 10^{-4} atomic per cent impurities for typical implantation energies used here ($\sim$ 40 keV). This level of sensitivity is limited primarily by pulse pile-up in the pulse handling system and can be reduced by an order of magnitude by use of significantly lower beam current or higher Z_1 incident particles (e.g. carbon).

In this study the channeling measurements were made using the Caltech Van de Graaff with a 1 MeV helium analyzing beam. A silicon surface barrier detector was used for the energy analysis of the scattered particles. In any individual run the error in the per cent attenuation may be as great as ± 10% due to uncertainties in the choice of a proper random spectrum and the scattering statistics.

Implantations of Cd and Te were made at energies between 20 and 50 keV into 10 and 100 ohm-cm n- and p-type etch-polished, float-zoned silicon. Ion doses were between 5×10^{13} and 8×10^{14} ions/cm^2 with substrate temperatures of 350°C and room temperature (R.T.). Implantations

were made with isotope separators at the Chalk River Nuclear Laboratories and the Research Institute for Physics, Stockholm. No deliberate attempt was made to orient the crystal with the incident beam. Annealing of the samples from 300 to 900°C was done in a tubular furnace with a flowing argon atmosphere.

<u>II.3.2 Results</u>. As discussed in the disorder section, the channeling measurements indicated that a heavily disordered (amorphous) layer was formed in R.T. implants for doses $\gtrsim 10^{14}$ ions/cm^2. This layer[2,3] anneals around 600°C as shown in fig. II.7 by the decrease in the surface peak of the ⟨111⟩ aligned silicon spectra measured after the 550 and 625°C anneals.

The decrease in the aligned Te spectra with increased anneal temperature in fig. II.7 indicates that as the disorder anneals an increasing fraction of the Te is found to be along the ⟨111⟩ crystal rows. A similar attenuation of the aligned Te spectrum for the ⟨110⟩ direction (fig. II.7) shows that $\approx$ 60% of the Te atoms occupy substitutional sites. The attenuation as a function of anneal tempeaature is shown in fig. II.8.

Based on the detector resolution, the width of the Te spectra gives 400 Å as an upper limit of the mean width of the dopant distribution. From this, a concentration of about 10^{20}/cm^3 Te atoms are found within 0.1 Å of substitutional sites. This exceeds by more than 3 orders of magnitude the maximum value of the reported solid solubility which was obtained by vapor deposition.[32]

Room temperature Cd implants behaved differently from that of Te or any of the Group III or V elements in silicon.[6] Around the tempera-

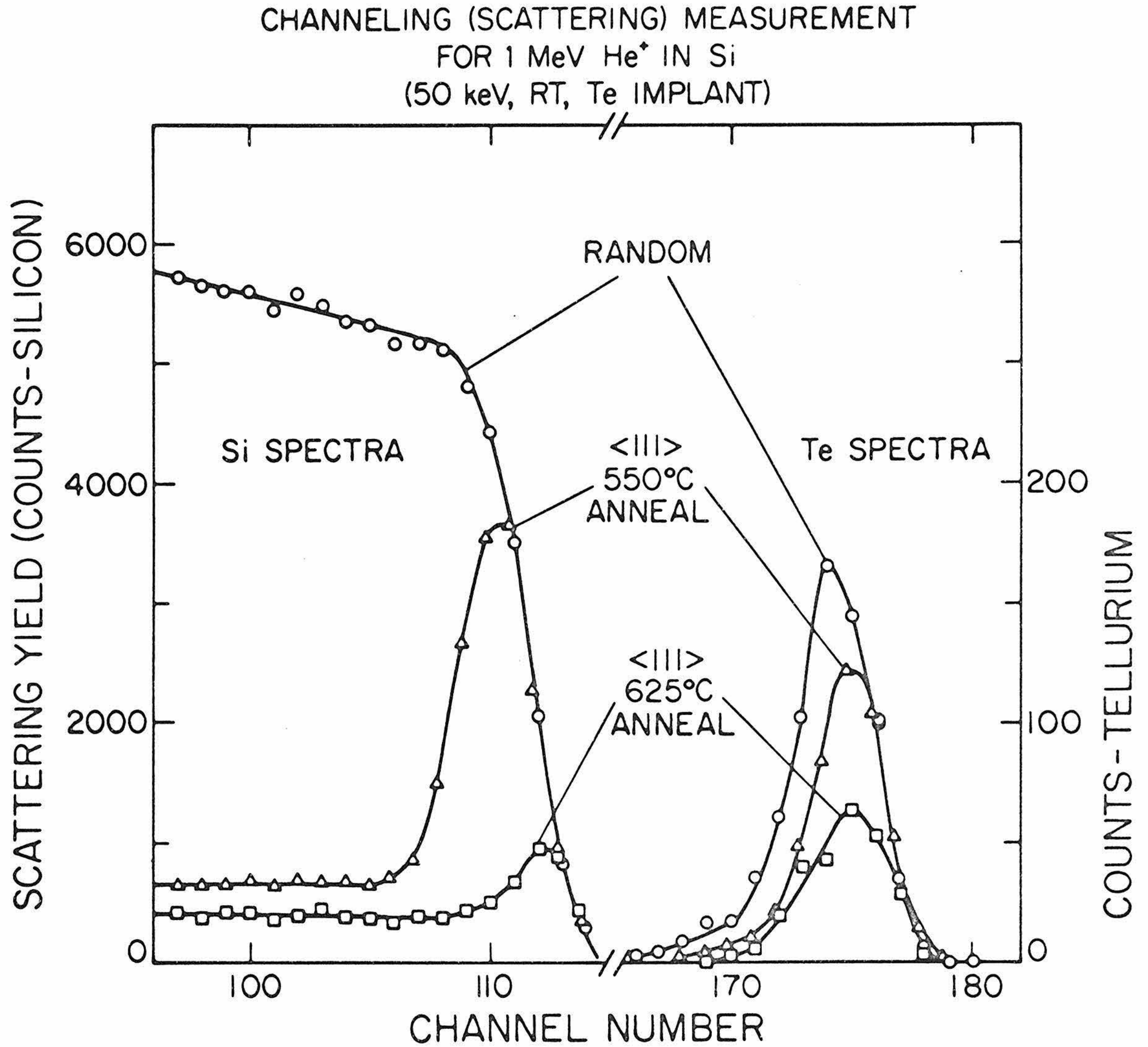

Fig. II.7 Random and ⟨111⟩ backscattering energy spectra using 1 MeV He^+ for a 50 keV R.T. Te implantation ($4 \times 10^{14}/cm^2$) in silicon

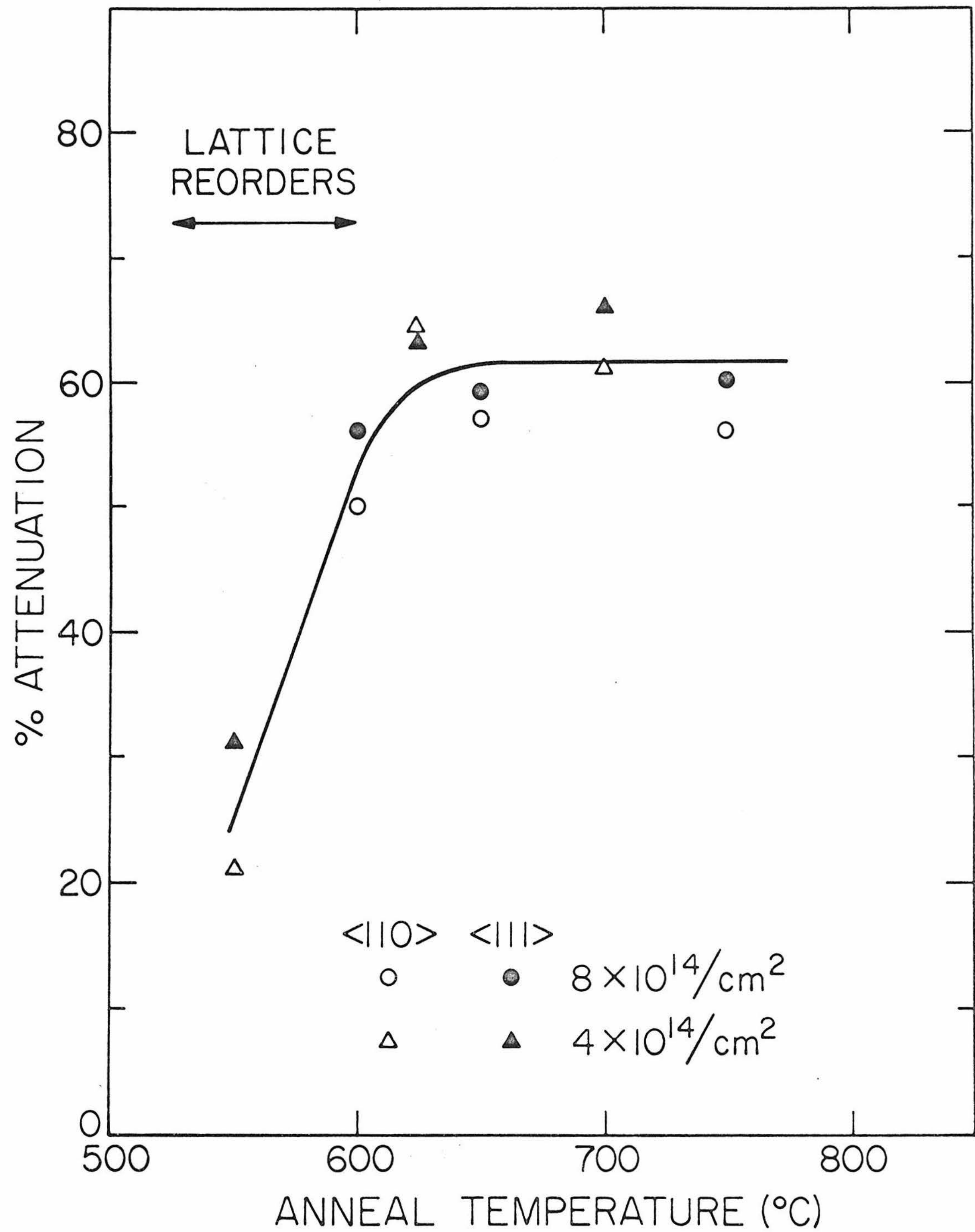

Fig. II.8 Attenuation in Te ⟨111⟩ and ⟨110⟩ spectra as a function of anneal temperature for 50 keV R.T. Te implantations in silicon.

ture region where the silicon lattice disorder anneals a decrease is noted in the total number of Cd atoms and no interstitial or substitutional component is found. This decrease in the Cd level can be clearly seen in fig. II.9 for a 40 keV implant of $2 \times 10^{14}/cm^2$. At the 600°C anneal stage essentially all the Cd is still present, as calculated from the scattering yield from the Cd peak, while the silicon ⟨111⟩ surface peak shows that only a small amount of lattice disorder remains. After annealing at 725°C, less than 10% of the Cd remains and the lattice disorder has decreased further.

We suggest that the Cd is swept to the surface during the reordering of the silicon lattice in a similar manner to that observed in gas release studies by Jech and Kelly[33] of Kr implanted in silicon. Other elements may exhibit this same behavior and be swept to the surface during the reordering of the amorphous layer. In the case of Cd, this was overcome by implanting in elevated temperature substrates (350°C) so that an amorphous layer was not formed.[6] Channeling effect measurements (figs. II.10 and II.11) indicated that there is no substitutional component and that at least 25% of the Cd is on regular interstitial sites along the ⟨111⟩ rows. However, this interstitial determination does not distinguish between the "tetrahedral" and "hexagonal" interstitial sites as discussed previously. Above anneal temperatures of 700°C, the interstitial component decreases with no decrease in the total amount of Cd.

II.4 Hall Effect Measurements.

Hall effect and sheet resistivity techniques[24,34] are used in this section to determine if such measurements can be correlated with

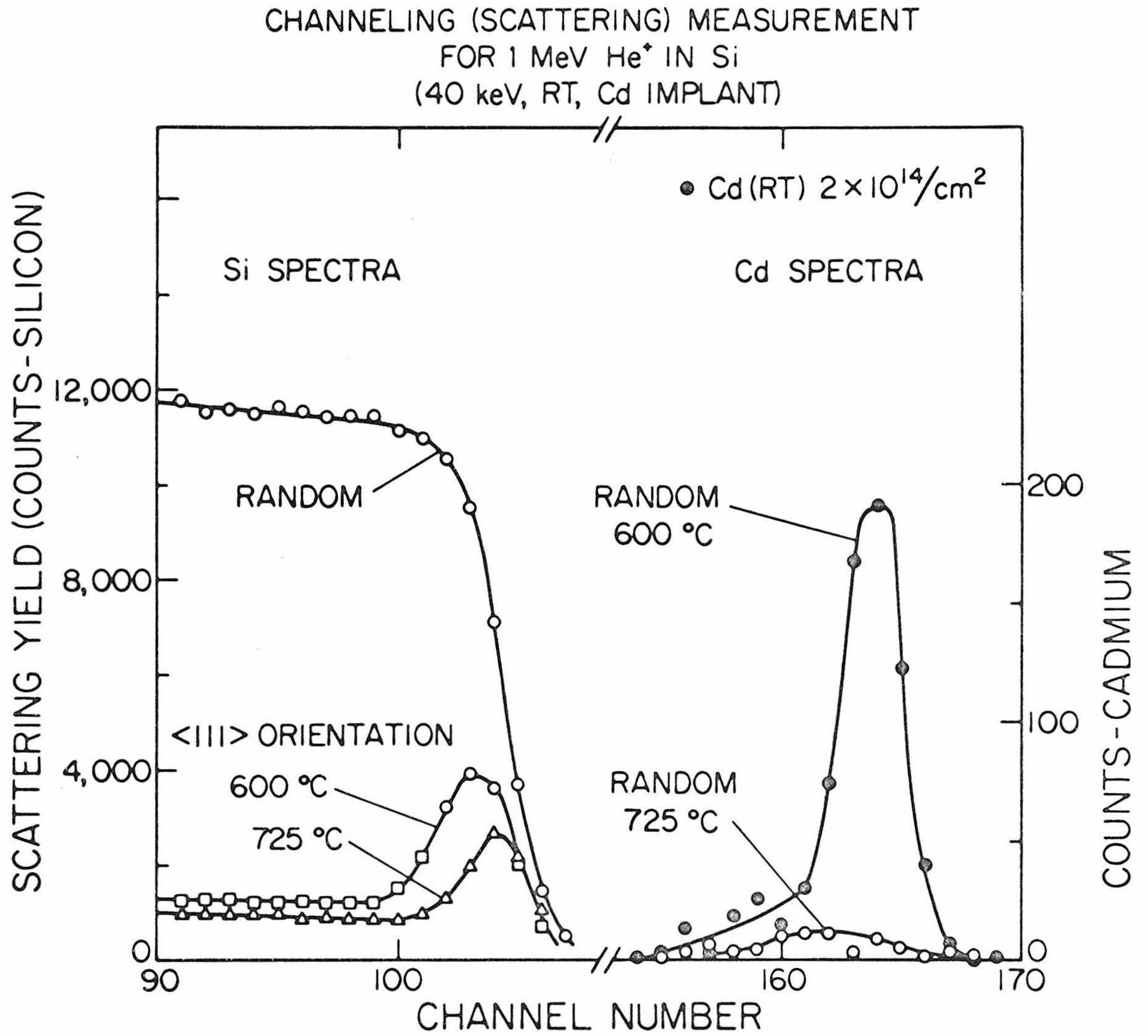

Fig. II.9 Random and ⟨111⟩ backscattering energy spectra using 1 MeV He^+ for a 40 keV R.T. Cd implantation ($2 \times 10^{14}/cm^2$) in silicon. Note decrease in Cd spectra with anneal.

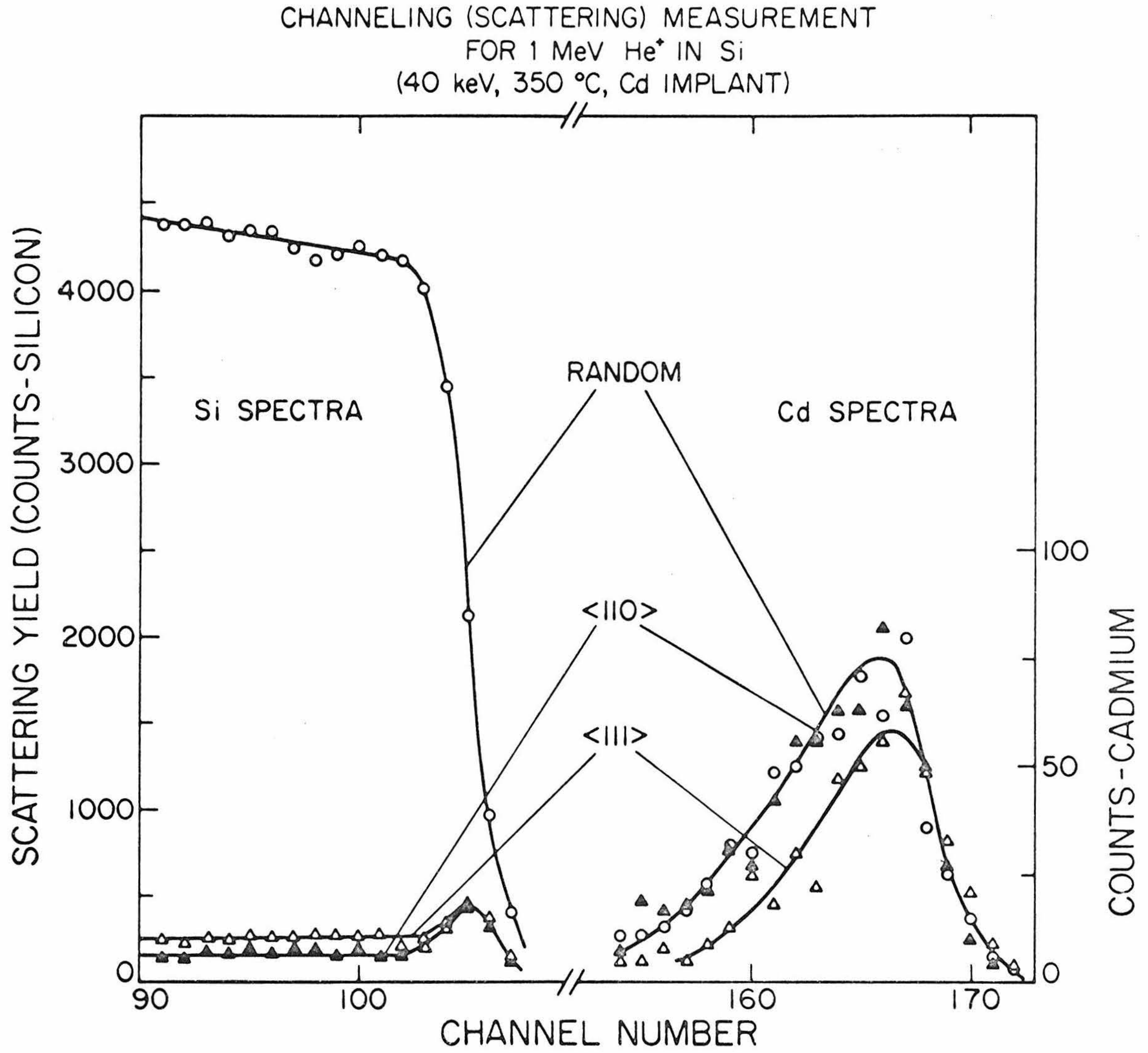

Fig. II.10 Random, ⟨111⟩, and ⟨110⟩ backscattering energy spectra using 1 MeV He^+ for a 40 keV 350°C Cd implantation ($5 \times 10^{14}/cm^2$) in silicon.

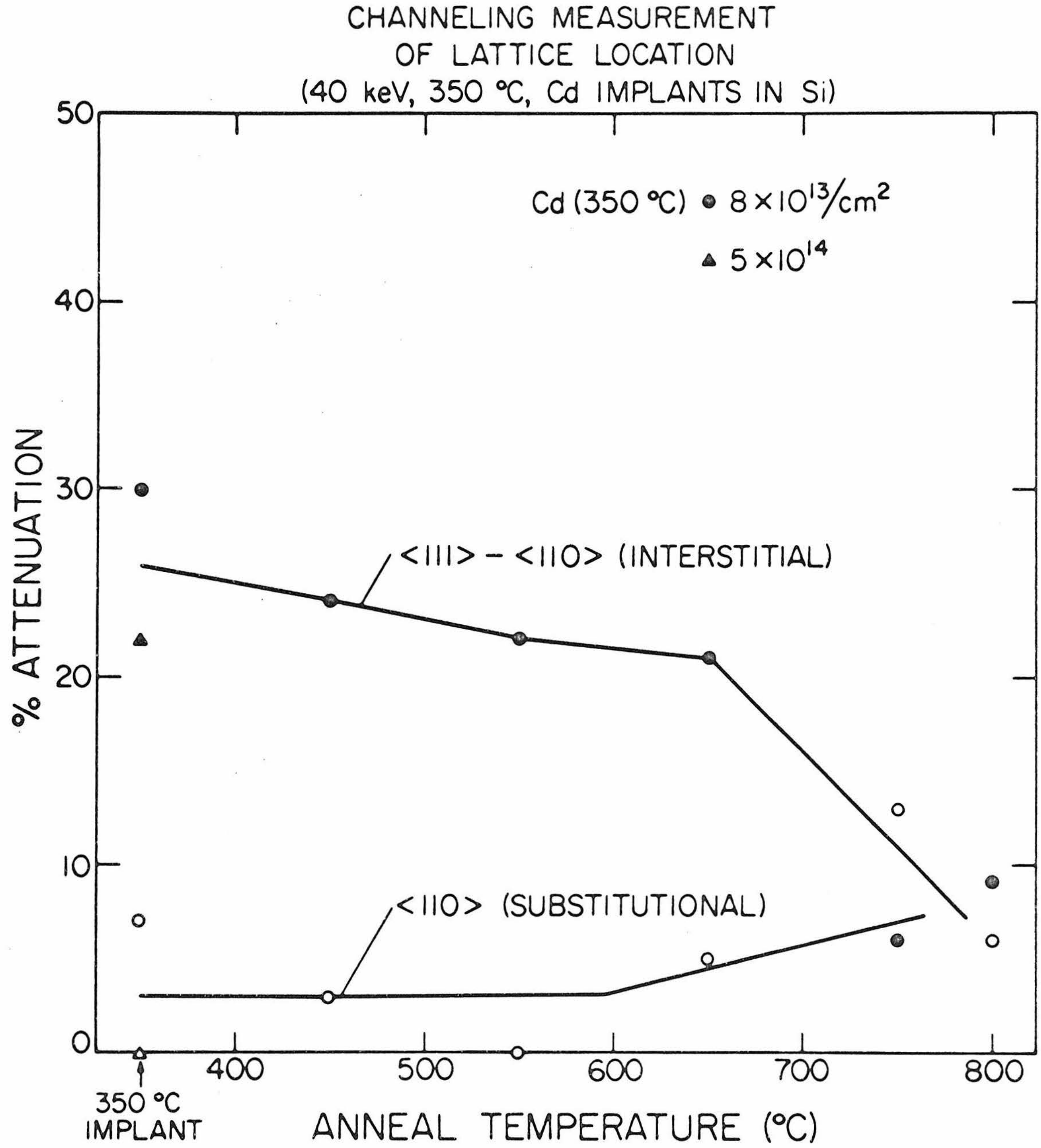

Fig. II.11 Attenuation in Cd spectra as a function of anneal temperature for 40 keV 350°C Cd implantations in silicon.

the channeling effect measurements. In particular, we study the electrical behavior of Te and Cd in the silicon lattice and attempt to correlate this with the lattice location and disorder results.

II.4.1 Technique. The ion implanted samples were analyzed in the Van der Pauw configuration[35] for Hall effect and sheet resistivity measurements. The geometry was obtained by conventional photo-resist and etching techniques. The silicon substrate is chosen to be of opposite electrical conductivity type from that in the implanted layer. The resulting p-n junction provides electrical isolation of the implanted region from the substrate. The configuration used for the measurement is a central circular region with four arms for electrical contacts (numbered clockwise 1 through 4).

The sheet Hall coefficient R_s is given by the change in voltage ΔV_{13} normal to the current path I_{24} for a magnetic field B perpendicular to the normal surface,[35]

$$R_s = \frac{\Delta V_{13} \cdot 10^5}{B \cdot I_{24}} \tag{II.2}$$

for units of volts, amps and kilogauss. The effective number of carriers/cm^2 is given by

$$N_s = \frac{1}{R_s e} \ . \tag{II.3}$$

The effective Hall mobility μ_H is then obtained from measurement of the sheet resistivity

$$\rho_s = \frac{\pi}{2 \log 2} \ (R_1 + R_2) \ f \tag{II.4}$$

by

$$\mu_H = \frac{1}{N_s e \rho_s} \tag{II.5}$$

where $R_1 = V_{12}/I_{34}$, $R_2 = V_{23}/I_{14}$, e is the charge on an electron and f is a function of R_1/R_2 having a value near unity for symmetrical geometry.[35]

These measured effective values of N_s can differ from the true value due to the variation of the carrier concentration n and mobility μ with depth x. In terms of these quantities, the measured sheet values of Hall coefficient and resistivity are*

$$R_s = \frac{\int n(x)\mu^2(x)dx}{e\left[\int n(x)\mu(x)dx\right]^2} \tag{II.6}$$

$$\rho_s = \left[e\int n(x)\mu(x)dx\right]^{-1} \tag{II.7}$$

which give

$$N_s = \frac{1}{eR_s} = \frac{\left[\int n(x)\mu(x)dx\right]^2}{\int n(x)\mu^2(x)dx} \tag{II.8}$$

$$\mu_H = R_s/\rho_s = \frac{\int n(x)\mu^2(x)dx}{\int n(x)\mu(x)dx} \tag{II.9}$$

whereas the true number of carriers/cm^2 is given by $\int n(x)dx$. From the integrals we see the measured N_s and μ_H are weighted averages.

---

*Following Baron[24] we neglect the difference between the conductivity and Hall mobilities since the difference is usually small for the high doping concentrations found in implanted samples.

In a typical sample there is a region of high concentration and low mobility followed by a tail region of low concentration and high mobility. The measured effective N_s can be as much as 1.5 times the true number of carriers due to the weighting of the higher mobility values in the tail region. Also typically the measured effective mobility can be a factor of 2 higher than the mobility in the high concentration region. These differences have been discussed in more detail previously[24] and confirmed experimentally.[24,36] For our purposes, it is only necessary that we be aware of these differences between the effective and true values of N_s and μ_H.

The description of the implantations and annealing was given in the previous section on lattice location. The Hall circuit had an input impedance of more than 10^{11} ohms and a magnetic field of 3900 gauss was used. Junction characteristics were examined to determine that the junction leakage current was less than 10% of the Hall current. The resistivity voltage V_{12} was measured for a range of values of current I_{34} to establish that V_{12} varied linearly with I_{34}.

<u>II.4.2 Results</u>. The electrical measurements indicate that Te acts as a donor. Measurements show (fig. I.12) that N_s increases through the region where the lattice is reordering. The number of carriers then levels off similar to that found in the lattice location measurements but at a level lower by a factor of ≈ 40 from the number of Te atoms on substitutional sites.

In order to compare the average Te concentration in 20 and 60 keV implantations, it is necessary to consider the distribution in depth of the implanted atoms rather than the upper limit of the distribution. The

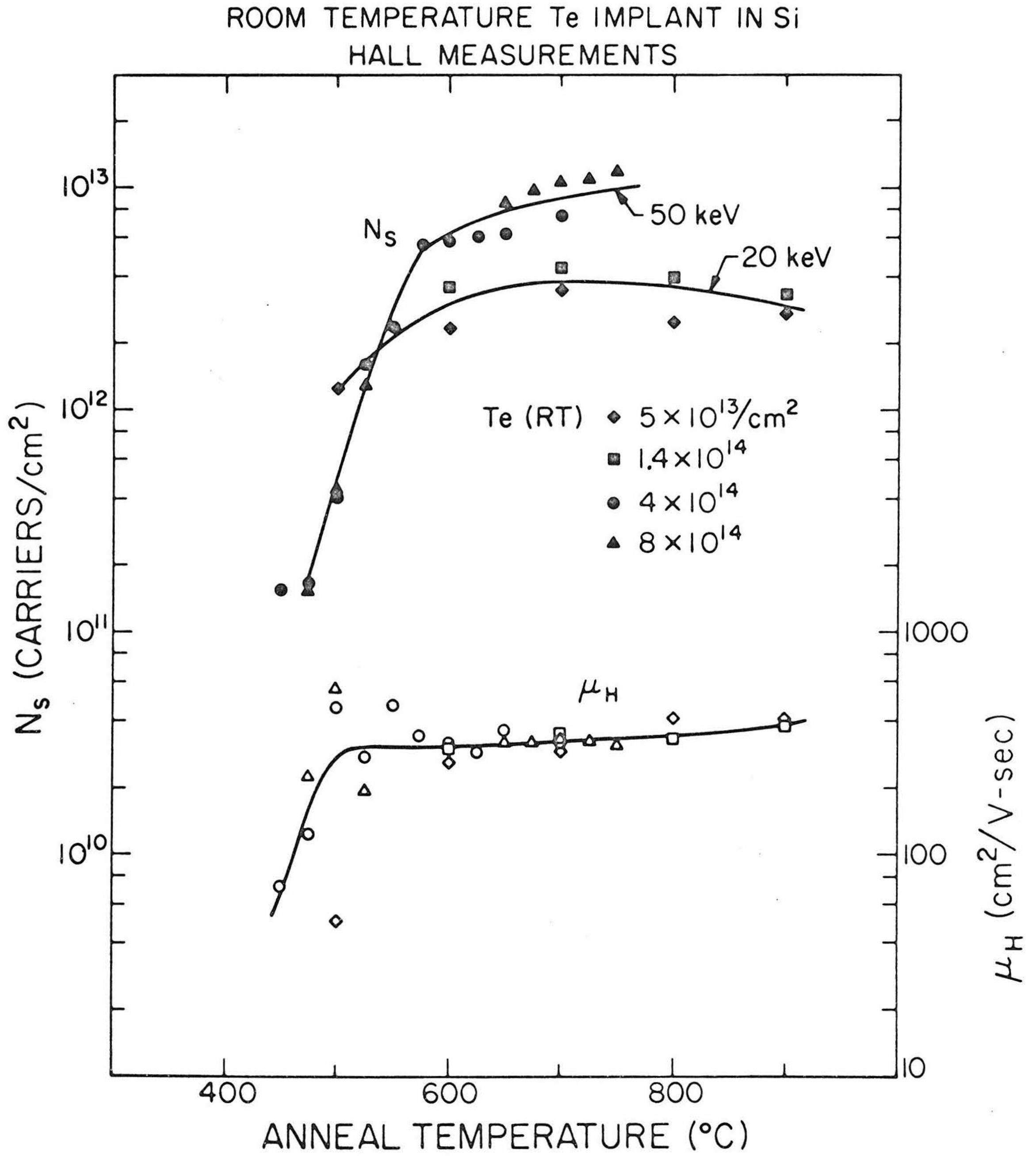

Fig. II.12 Effective number of carriers/cm^2 N_S and Hall mobility μ_H as a function of anneal temperature for R.T. Te implantations in silicon.

Gaussian widths (ΔR) as calculated from the theory of Lindhard et al.[37] are 42 and 85 Å respectively. The average carrier concentration ($\bar{n}$) can be determined from N_s by, $\bar{n} \approx N_s/2.5\Delta R$, assuming that the electron and Te distributions have the same shape. This gives a value of approximately 10^{18} carriers/cm^3 at 700^oC anneal for both the 20 and 50 keV implants. Thus the primary difference in N_s for the two different sets of Te implants (fig. I.12) is due to the difference in implant energy.

The measured effective mobility value of 320 cm^2/V-sec is a factor of 1.5 higher than the Hall mobility determined from the carrier concentration.[38,39] The high effective mobility is due to the mobility variation in the implanted region as discussed previously. For example, in silicon samples implanted at R.T. with Sb[34] and Bi,[36] the effective mobility was found to be 1.5 to 2 times greater than the mobility in the region of maximum carrier concentration. This factor depends on the carrier distribution. The mobility value for the Te ion implantations is consistent with a concentration of $10^{18}/cm^3$ ionized Te impurity scattering centers rather than the much greater concentration of substitutional Te atoms. Based on these data we suggest that the implanted Te has a deep level. This is in agreement with the only reported measurement[32] of the energy level of Te in silicon (0.14 eV).

The lattice location analysis indicated that the Cd implantations at room temperature exhibited an outdiffusion behavior when the damage annealed. In these implantations no electrical activity that could be identified with Cd was found in 11 ohm-cm n-type silicon.

It was shown that this outdiffusion behavior could be overcome by implanting at elevated temperatures. Junction evaluation and Hall mea-

surements showed n-type behavior for hot substrate Cd implantations in Cd implantations in p-type silicon for anneal temperatures between 500 and 750°C (fig. II.13). No dopant action was observed in similar implants in n-type silicon. The increase in electrical activity in the region up to 550°C is typical of hot implants.[40] The decrease in N_s above 650°C (fig. II.13) corresponds with the decrease in interstitial Cd (fig. II.11). The maximum value of N_s of $10^{11}/cm^2$ corresponds to an average density $\bar{n} \approx 5 \times 10^{16}/cm^3$. This is lower by about 2 or 3 orders of magnitude than the concentration of Cd on interstitial sites and the bulk mobility for this density in n-type silicon would be $\approx 1000\ cm^2/V$-sec. The effective Hall mobility is much lower ($\approx 250\ cm^2/V$-sec) suggesting, in contrast to the Te case, that the low number of carriers is due to strong compensation effects. The only reported measurement of diffused Cd in silicon indicated only marginal electrical activity.[41]

We attribute the n-type behavior of the Cd implantations to donor action of the observed interstitial component. In hot substrate Tl implantations in silicon, similar n-type behavior was also attributed to the donor action of the interstitial component.[24]

II.5 Summary.

We have demonstrated how one can use these techniques of channeling effect and Hall effect measurements to study ion implanted impurities in semiconductors. This approach is seen to be especially useful for the investigation of unconventional dopant species. A correlation is obtained between the channeling effect measurements of lattice disorder and lattice location and the Hall effect and sheet resistivity measurements.

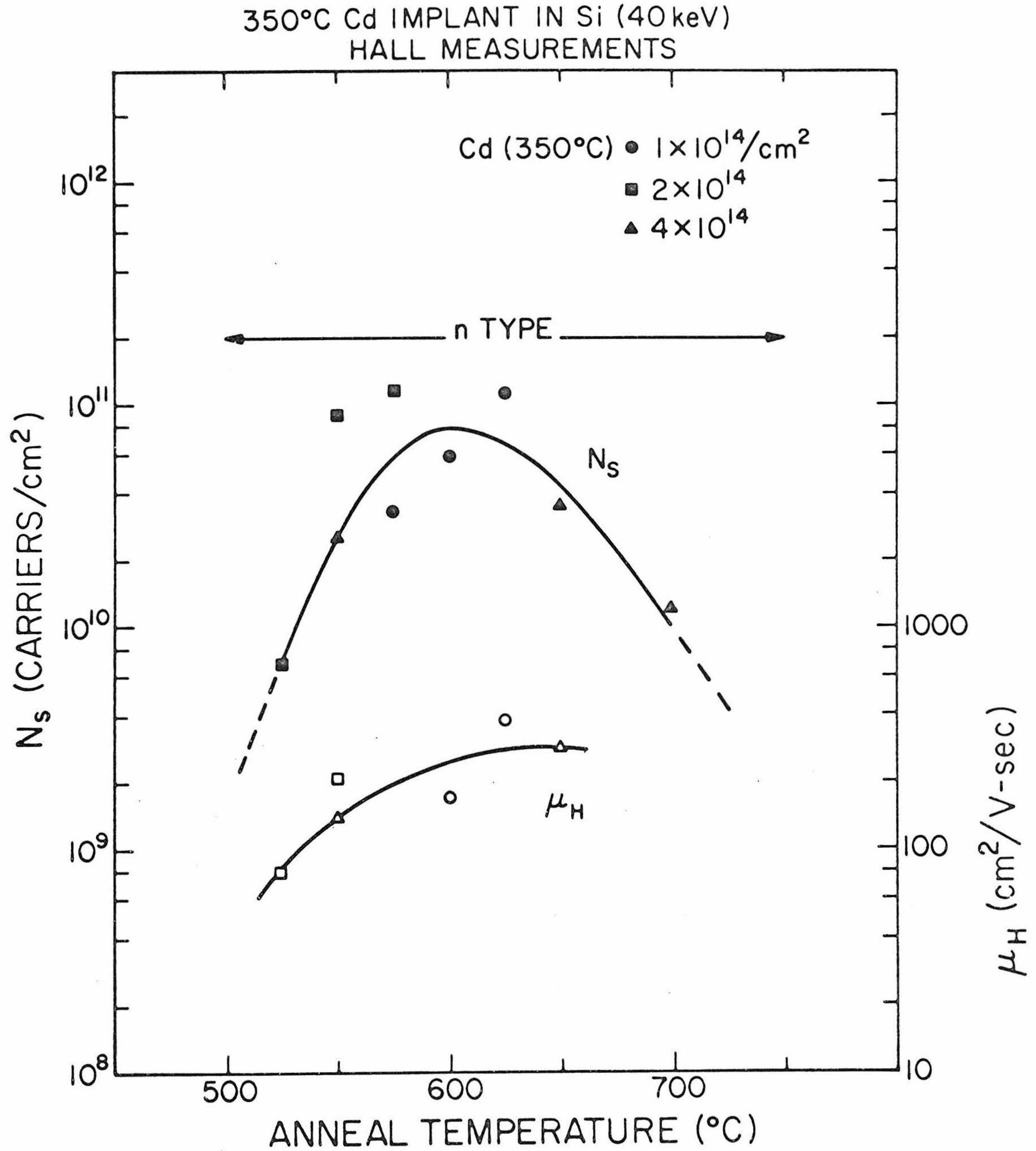

Fig. II.13 Effective number of carriers/cm^2 N_S and Hall mobility μ_H as a function of anneal temperature for 40 keV 350°C Cd implantations in silicon.

In particular Te implanted into silicon is a substitutional atom and exhibits donor action. In contrast to this Cd has an interstitial component which appears to be responsible for its n-type behavior.

Appendix A

Table of Symbols

Symbol	Meaning
Z_1	Atomic number of projectile
Z_2	Atomic number of lattice atoms
$\overline{Z}_2$	Average atomic number of atoms along row or in plane
d	Distance between atoms along row
$\overline{d}$	Average distance between atoms along row
d_p	Distance between planes
E	Projectile energy
N	Atomic density of crystal
a	Thomas-Fermi screening distance
ρ_r	Root mean square vibrational amplitude perpendicular to a row
ρ_p	Root mean square vibrational amplitude perpendicular to a plane
$\psi_{\frac{1}{2}}$	Channeling critical angle
ψ_1	Axial characteristic angle = $(2Z_1Z_2e^2/Ed)^{\frac{1}{2}}$
ψ_n	Planar characteristic angle = $(Z_1Z_2e^2Nd_pa/E)^{\frac{1}{2}}$
ψ	Angle of particle motion with respect to crystal row or plane
$E_\perp$	Energy associated with transverse motion of particle = $E\psi^2$
α	Axial critical angle coefficient
β'	Planar critical angle coefficient = $b\beta$
β	Planar critical angle coefficient without surface transmission
b	Planar surface transmission coefficient
V	Screened atomic potential
$\overline{V}$	Average potential for crystal row or plane
C	Constant of screened potential approximation $\approx \sqrt{3}$
r	Radial distance of axial channeled particle from the row

y Perpendicular distance of planar channeled particle from the plane

r_{min} Minimum impact parameter for axial channeling

y_{min} Minimum impact parameter for planar channeling

Θ_D Debye characteristic temperature

M_1 Mass of projectile atom

M_2 Mass of lattice atoms

η Depth from which particle is backscattered

E_o Incident energy of the projectile

S Stopping power of the material (dE/dx)

k Fractional energy of projectile after being backscattered

θ_s Scattering angle

Appendix B

Derivations for Critical Angles

B.1 Minimum Impact Parameter for Axial Channeling.

The minimum impact parameter (r_{min}) for the steering of a channeled projectile by a row of atoms can be obtained from emission calculations. Emission or blocking experiments are for particles incident in a random direction and scattered by a lattice atom (i.e. the lattice atoms are treated as a source of particles). The angular distribution is observed along a channeling direction. This is equivalent by the reversibility law[7,42] to particles coming in along a channeling direction. A particle is emitted with energy E from a lattice atom that is vibrating with a mean square vibration amplitude ρ_r^2 with respect to the row. We assume that the probability of an atom to be a radial distance r from the row is a Gaussian

$$dP(r) = e^{-r^2/\rho_r^2} \frac{2r}{\rho_r^2} dr .$$

The probability distribution in transverse energy of the particles emitted from the vibrating atom has been given as[d]

$$\pi(E_\perp) \simeq \int_0^\infty dP(r) \int d(E\varphi^2) \int_0^{2\pi} \frac{d\theta}{2\pi} \delta(E_\perp - \overline{V}(r) - E\varphi^2) \qquad \text{(B.1)}$$

which gives

$$\pi(E_\perp) = e^{-\hat{r}^2/\rho_r^2} \qquad \text{(B.2)}$$

where $\hat{r}(E\ )$ is given by

$$\overline{V}(r) = E_\perp .$$

It has been shown[14] for axial channeling that the modification of this distribution by the effect of surface transmission has a negligible effect on the critical angle. Therefore, we do not consider surface transmission in this calculation.

The angular distribution is related to $E_\perp$ by $E\psi^2 = E_\perp$ and at minimun impact,

$$\pi(E_\perp = E\psi_{\frac{1}{2}}^2) \simeq \tfrac{1}{2} \tag{B.3}$$

so that

$$e^{-r_{min}^2/\rho_r^2} = \tfrac{1}{2}$$

and

$$r_{min} = \rho_r(\log 2)^{\frac{1}{2}} . \tag{B.4}$$

B.2 Critical Angle Coefficient (α) for Axial Channeling.

Neglecting surface transmission,

$$E\psi_{\frac{1}{2}}^2 = \bar{V}(r_{min}) \tag{B.5}$$

$$= 1/d \int_{-\infty}^{\infty} V\left(\sqrt{r_{min}^2 + z^2}\right) dz \tag{B.6}$$

$$= \tfrac{1}{2} E\psi_1^2 \xi\left(\frac{r_{min}}{a}\right) \tag{B.7}$$

where

$$\psi_1 = \left(\frac{2Z_1Z_2e^2}{Ed}\right)^{\frac{1}{2}} .$$

Using Lindhards' approximation to a Thomas-Fermi potential,* a good overall fit to ξ is given by

$$\xi(r/a) = \log\left[\left(\frac{Ca}{r}\right)^2 + 1\right] .$$

This corresponds to using

$$V(r) = Z_1Z_2e^2\left(\frac{1}{r} - \frac{1}{(r^2+C^2a^2)^{1/2}}\right). \qquad \text{(B.8)}$$

Then

$$\alpha = \psi_{\frac{1}{2}}/\psi_1$$

$$= \left[\frac{1}{2}\log\left(\frac{C^2a^2}{\rho_r^2 \log 2} + 1\right)\right]^{\frac{1}{2}} \qquad \text{(B.9)}$$

The numerical calculations of Andersen show that this choice of α is valid for $\psi_1 < \rho/d$. The values of α have been calculated using ρ_r values obtained from available experimental values for the Debye characteristic temperature Θ_D. Wherever possible, values of θ_D obtained from x-ray data rather than from specific heat measurements were used. This was done because the specific heat measurements give equal weight to each of the normal modes of the frequency spectrum whereas for the mean square displacement the contribution is greater for the lower frequency

*In this energy region, the Moliere approximation of the screened atomic potential has also been used.[11] In this work, we have used the Lindhard approximation because of the simplicity of the resulting formulas.

than the higher frequency modes. The x-ray measurements of the temperature dependence of the Bragg reflections give this latter type of weighting of the frequency spectrum.[43] The mean square, vibrational amplitude perpendicular to an axis is given by[19]

$$\rho_r^2 = 2/3\ \rho^2$$

$$= 2/3 \left[\frac{9\hbar^2}{kM_2\Theta_D}\left(\frac{\varphi(x)}{x} + 1/4\right)\right] \qquad \text{(B.10)}$$

assuming $\rho_x^2 = \rho_y^2 = \rho_z^2$ where $x = \frac{\Theta_D}{T}$ and the Debye function

$$\varphi(x) = \frac{1}{x}\int_0^x \frac{\zeta d\zeta}{e^{\zeta}-1} \ .$$

The following values were used:

Crystal	Θ_D (^oK)	ρ^2 ($\AA^2$)	α	ref.
Si	543	$.0167_5$	1.12_5	a
Ge	290	.0214	1.00	a
C	2240	$.0045_5$	1.44	b
GaAs	314	.0183	1.03	b
GaP	445	.0135	1.14	c
GaSb	233	.0234	0.94	b

a. B. W. Batterman and D. R. Chipman, Phys. Rev. 127, 690 (1962).

b. K. Lonsdale, International Tables for X-ray Crystallography Vol. 3 (Kynoch Press, Birmingham, U. K. 1962).

c. R. Weil and W. O. Groves, J. Appl. Phys. 39, 4049 (1968).

B.3 Minimum Yield Related to Critical Angle.

The minimum yield for axial channeling is that fraction of the

aligned incident beam that does not become channeled,

$$\chi_{min} = \pi N d r_{min}^2 \tag{B.11}$$

where N is the atomic density of the crystal. As in the case of the critical angle derivations, the dependence on depth is not included. The minimum yield is related to the critcal angle in section A.2 by

$$\psi_{\frac{1}{2}}^2 = \tfrac{1}{2}\psi_1^2 \xi(r_{min}/a)$$

which, for the region under consideration ($r_{min} \approx a$), can be approximated[7] by the simple form

$$\xi\left(\frac{r_{min}}{a}\right) = \frac{\pi a}{2r_{min}} \quad . \tag{B.12}$$

Thus

$$\chi_{min} = \frac{\pi^3}{16} N d a^2 (\psi_1/\psi_{\frac{1}{2}})^4 \quad . \tag{B.13}$$

B.4 Critical Angle Coefficient for Planar Channeling.

The transverse energy at the critical angle

$$E\psi_{\frac{1}{2}}^2 = \overline{V}(y_{min})$$

$$= N d_p \int_0^{\infty} 2\pi z V\left(\sqrt{y_{min}^2 + z^2}\right) dz$$

$$= 2\pi Z_1 Z_2 e^2 N d_p \left[\left(y_{min}^2 + C^2 a^2\right)^{\frac{1}{2}} - y_{min}\right] \tag{B.14}$$

where d_p is the planar spacing and y_{min} the minimum impact parameter

for channeling of the projectile with the plane. Using

$$\psi_{\frac{1}{2}} = \beta \psi_n$$

where

$$\psi_n = \left[\frac{Z_1 Z_2 e^2 N d_p a}{E}\right]^{\frac{1}{2}}$$

gives

$$\beta = \left\{ 2\pi/a \left[(y_{min}^2 + C^2 a^2)^{\frac{1}{2}} - y_{min} \right] \right\}^{\frac{1}{2}} . \tag{B.15}$$

Appendix C

Limits of Average Potential Approximation

The region of validity for the average potential approximation* in the channeling calculation is derived for both the axial and planar cases. This establishes a lower limit to the critical angle for a given choice of crystal, projectile, and direction. The approach we have used for the axial case is slightly different from that used by Lindhard[7] although the results are equivalent. This approach was used so that we could also obtain limits for the planar case.

The basic assumption is that at the point of minimum impact with the row or plane the deflection given to the projectile ($\Delta\psi$) by the lattice atom in that row or plane should be only a small fraction of the total turning angle ($\psi=2\psi_{\frac{1}{2}}$) of the channeled particle. This insures that the steering of the projectile is the result of a series of gentle collisions with many atoms in the row or plane, as implied by the approximation of an average potential. The classical formula for small angle scattering can be obtained from the momentum transfer

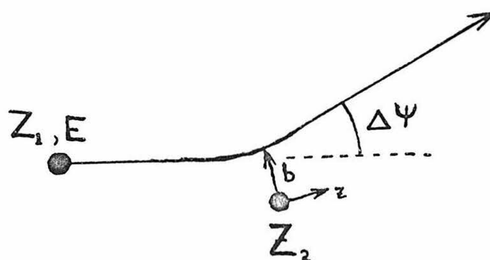

*A wave diffraction calculation has not been used here since for the energies and mass of the particles considered in this work the classical limit applies.[44]

$$\Delta\psi = \frac{\Delta p}{p} \quad (\text{for } \Delta p \ll p)$$

$$= \frac{1}{2E}\int_{-\infty}^{\infty} -\frac{\partial V}{\partial b}\left[\sqrt{b^2+z^2}\right] dz \qquad (C.1)$$

where E is the energy, V(r) the potential at a distance r and b the impact parameter.

C.1 Axial Case.

Using Lindhard's approximation to the Thomas-Fermi potential

$$V(r) = Z_1 Z_2 e^2 \left(\frac{1}{r} - \frac{1}{\sqrt{r^2+C^2a^2}}\right),$$

we obtain

$$\Delta\psi = \frac{Z_1 Z_2 e^2}{E\, r_{min}} \frac{1}{1+\left(\frac{r_{min}}{Ca}\right)^2} . \qquad (C.2)$$

Using $\psi = 2\psi_{\frac{1}{2}}$

$$\frac{\Delta\psi}{\psi} = \frac{\psi_1 d}{4\alpha r_{min}} \frac{1}{1+\left(\frac{r_{min}}{Ca}\right)^2} \qquad (C.3)$$

to define an arbitrary cross-over point into a slow transition region. We require the deflection at minimum impact to be 20% of the total turning angle before the approximation begins to break down

$$\frac{\Delta\psi}{\psi} < 0.2$$

or

$$\psi_1 < \frac{r_{min}}{d}\, 0.8\alpha \left[\left(\frac{r_{min}}{Ca} \right) + 1 \right]$$

where $\alpha \approx 1$, $C = \sqrt{3}$ and $r_{min} = \rho_r(\log 2)^{1/2}$.

This gives the criteria:

$$\psi_1 < \frac{a}{d} \ .$$

The measurements in this thesis met this requirement for energetic particle channeling. For example, $\frac{\Delta\psi}{\psi} = 0.03$ for 1 MeV He in Si along the $\langle 111 \rangle$ direction.

C.2 Planar Case.

The deflection corresponding to a particle passing directly over a lattice atom at the point of minimum impact (y_{min}) with the plane is given by

$$\Delta\psi = \frac{Z_1 Z_2 e^2}{E y_{min}} \frac{1}{1 + \left(\frac{y_{min}}{Ca} \right)^2} \ .$$

From the relation $\psi = 2\psi_{\frac{1}{2}}$ and using $\psi_{\frac{1}{2}} = \beta\psi_n$, we obtain

$$\frac{\Delta\psi}{\psi} = \frac{\psi_n}{2 N d_p a} \frac{1}{y_{min}\left[1 + \left(\frac{y_{min}}{Ca} \right)^2 \right]} \frac{1}{\sqrt{\frac{2\pi y_{min}}{a} \left[\left(1 + \frac{C^2 a^2}{y_{min}^2} \right)^{\frac{1}{2}} - 1 \right]}} \qquad (C.4)$$

In the planar case, the minimum impact parameter cannot be derived in closed form from the distribution function as for the axial case (Appendix B.1). However, we can obtain a numerical solution for the distribution function (Appendix D, eq. D.2) for a particular case and hence y_{min} for that case. For helium channeling along the {110} in silicon,

we obtain, $\beta = 2.7$. Then from Appendix B.4

$$\beta = \sqrt{\frac{2\pi}{a}\left[\left(y_{min}^2 + C^2 a^2\right)^{\frac{1}{2}} - y_{min}\right]}$$

giving $y_{min} \approx 0.7a$ (e.g. 0.12 Å for He in Si). This value of y_{min} can also be used as an approximate estimate for planar channeling for other projectiles and semiconductor crystals. The numerical calculation of β is only weakly dependent on vibrational amplitude, potential screening distance, and planar spacing. From this estimate of y_{min} we can obtain

$$\frac{\Delta\psi}{\psi} = \frac{\psi_n}{4.5\ Nd_p a^2} \ .$$

Unlike the axial case the projectile will not always pass directly over a lattice atom in the plane at its minimum impact. So if we relax the restrictions a little from the axial case to

$$\frac{\Delta\psi}{\psi} < \frac{1}{2} ,$$

then

$$\psi_n < 2Nd_p a^2 \qquad (C.5)$$

is our estimate of the limit for the average potential approximation to be valid. To give an estimate for 1 MeV He in Si along the {110} $\frac{\Delta\psi}{\psi} \simeq 0.2$. The value of $\psi_n = 2Nd_p a^2$ corresponds to $\approx$ 200 keV in Si.

Appendix D

Planar Channeling Angular Distribution Calculation Including the Effect of Surface Transmission

This calculation follows that outlined by Andersen.[14] The channeling distribution is calculated for the emission of particles from a vibrating atom in the plane. The zero-point and temperature dependent vibrations are represented by a Gaussian distribution of the probability of the emitting atom to be a distance y from the plane*

$$dP = \sqrt{\frac{2}{\pi}}\, e^{-y^2/2\rho_P^2}\, \frac{dy}{\rho_P} \qquad (D.1)$$

where here ρ_P^2 is the mean square displacement perpendicualr to the plane.

The angular distribution for $E_{\perp} = E\psi^2$ without the influence of surface transmission is given by the probability distribution

$$\pi(E_{\perp}) = \int_{\hat{y}(E_{\perp})}^{d_p/2} \left[\frac{E_{\perp}}{E_{\perp} - V(y)}\right]^{\frac{1}{2}} dP(y) \qquad (D.2)$$

where $\hat{y}$ is given by the average potential

$$\bar{V}(\hat{y}) = E_{\perp} \qquad \text{for } E_{\perp} < \bar{V}(o)$$

$$\hat{y} = o \qquad \text{for } E_{\perp} \geq \bar{V}(o)$$

and E is the energy of the particle and ψ the angle with respect to the plane. This gives an angular width proportional to $d_p^{\frac{1}{2}}$. Including the effect of surface transmission gives an angular distribution

*Note Andersen's correction in this formula from that originally given in ref. 14.

$$P(E\psi^2) = \int_0^{d_p/2} \frac{dy}{d_p} \; K(E\psi^2+\overline{V}(y)) \; \pi(E\psi^2+\overline{V}(y)) \tag{D.3}$$

where the normalization factor

$$K(E_\perp) = \left[\int_{\hat{y}(E_\perp)}^{d_p/2} \frac{dy}{d_p} \left(\frac{E_\perp}{E_\perp+V(y)} \right)^{\frac{1}{2}} \right]^{-1} .$$

The integrals involved in the distribution functions were solved numerically by computer to obtain the $P(E\psi^2)$ vs. ψ distribution for each given set of parameters (projectile, energy, crystal and direction).

Appendix E

Useful Formulas for Channeling Applications

E.1 Rutherford Scattering Cross Section.

The Rutherford scattering probability for large angle scattering of a particle of mass M_1, charge Z_1 and energy E by a target atom of mass M_2 and charge Z_2 into a solid angle $d\Omega$ is given by

$$\frac{d\sigma}{d\Omega} = \left(\frac{Z_1 Z_2 e^2}{4e}\right)^2 \left(\frac{M_1+M_2}{M_2}\right)^2 \frac{1}{\sin^4(\theta/2)}$$

$$= 1.3 \times 10^{-27} \left(\frac{Z_1 Z_2}{E}\right)^2 \left(\frac{M_1+M_2}{M_2}\right)^2 \frac{1}{\sin^4\left(\frac{\theta}{2}\right)} \ \mathrm{cm}^2/\mathrm{sr} \qquad \text{(E.1)}$$

where θ is the scattering angle in center of mass coordinates and E is the energy in units of MeV.

E.2 Energy Loss.

Consider an incident particle penetrating the crystal to a depth η and then being backscattered

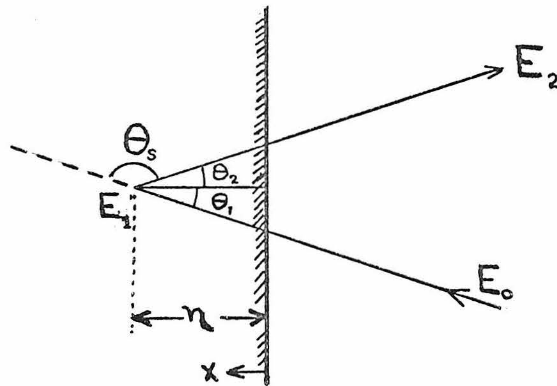

Fig. E.1

where E_o is the incident energy, E_1 the energy just before scattering, E_2 the energy after leaving the crystal and θ_s the scattering angle.

The energy of the backscattered particle E_2 is given by

$$E_2 = k\left[E_o - \int_o^{\eta/\cos\theta_1} S_1(E)dx\right] - \int_o^{\eta/\cos\theta_2} S_2(E)dx \qquad (E.2)$$

where S_1 and S_2 are the stopping powers* (dE/dx) for the particle along its incident and scattered paths and the fractional amount of energy the particle has after scattering is

$$k = \left[\frac{M_1\cos\theta_s + \sqrt{M_2^2 - M_1^2\sin^2\theta_s}}{M_1+M_2}\right]^2$$

$$\simeq \left[\frac{M_1\cos\theta_s + M_2}{M_1+M_2}\right]^2 \qquad (E.3)$$

for large angle backscattering. Typical stopping powers for a non-channeling (random) direction are 30 eV/Å for 1 MeV He in Si and 40 eV/Å for 1 MeV He in Ge. A small uncertainty is introduced for a particle for a channeling orientation due to its reduced energy loss while being channeled and a lack of knowledge of the point at which the particle is dechanneled. This is not critical in our measurements because of the small depths probed in these studies (typically $\leqslant$ 5000 Å). A reasonable estimate can be given by $S_1 = tS$ where S is the normal stopping power and t is $\approx$ 0.6 (i.e. S_1 between random and best channeled dE/dx).

In most cases the stopping power for MeV He atoms can be approximated as a constant or linear function giving for the depth

*Stopping powers are frequently tabulated as (1/N)dE/dx but here we are not normalizing to density (N).

$$\eta = \frac{(kE_o - E_2)\cos\theta}{s_o(tk+1)} \qquad \text{for } S = s_o = \text{constant} \tag{E.4}$$

where $\theta_1 \approx \theta_2 = \theta_s$, or

$$\eta = \frac{\cos\theta}{s_1} \log\left[\frac{s_1(kE_o - E_2)}{(s_o + s_1 E_o)(tk+1)} + 1\right] \qquad \text{for } S = s_o + s_1 E \,. \tag{E.5}$$

E.3 Number/cm^2 of Impurity Atoms from Backscattering Spectrum.

In cases where the impurity atoms have a larger mass than the substrate atoms and are confined to a region near the surface, the particles scattered from impurity atoms will all be of a higher energy than those scattered from the substrate atoms (see section E.2). By comparing the scattering yield from the impurity atoms to the yield from the substrate we may use the known density (#/cm^3) of substrate atoms to estimate the number of impurity atoms per unit area (area normal to the beam direction).

From the random energy spectrum, we obtain the total scattering yield from the impurity atoms by summing the counts in the impurity peak A (# counts). The scattering yield R from the substrate of atomic density N is the number of counts/channel in the portion of the random energy spectrum near the end-point E_p. The end-point E_p in the spectrum is the channel number which corresponds to the energy of particles scattered from the substrate surface with energy kE_o.

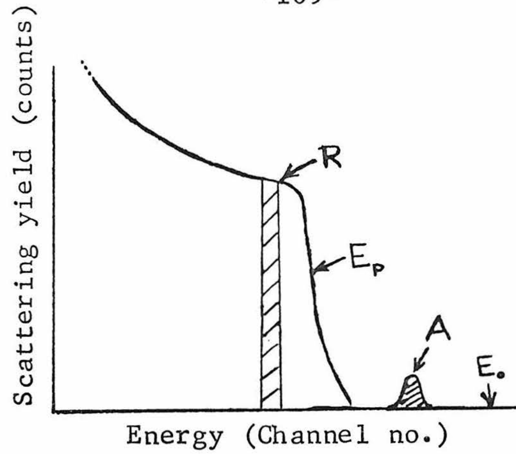

Fig. E.2

The energy per channel is given by kE_o/E_p and using the stopping power S we obtain the depth in the substrate which corresponds to one channel on the energy spectrum $\left(\frac{kE_o}{E_p}\right)\left\{[1+\csc(\pi-\theta_s)]\ S\right\}^{-1}$. In this case the stopping power is assumed constant over the small depth involved and normal incidence of the beam is assumed with θ_s the scattering angle (see fig. E.1). The number of substrate atoms per unit area represented by scattering counts R from one channel (near the surface) in the energy spectrum is

$$\left(\frac{N}{R}\right)\left(\frac{kE_o}{E_p}\right)\left\{S[1+\csc(\pi-\theta_s)]\right\}^{-1} \quad \#/\mathrm{cm}^2/\mathrm{counts}\ .$$

The relative scattering yield for the impurity can then be directly converted from number of counts to its density $N_I(\#/\mathrm{cm}^2)$,

$$N_I = \frac{NkE_o}{RE_p S[1+\csc(\pi-\theta_s)]} \cdot A \cdot \left(\frac{Z_2}{Z_I}\right)^2 \qquad (E.6)$$

where the correction for the difference in scattering cross section (eq. E.1) with atomic number of the substrate Z_2 and impurity Z_I have been taken into account. Note that the mass correction from eq. E.1

is neglected since typically $M_1 \ll M_2$. For a typical case of 1 MeV He ions incident on silicon we obtain from eq. E.6

$$N_I = 9.5 \times 10^{20} \frac{A}{E_p R Z_I^2} \ \#/cm^2 \qquad \text{(E.6)}$$

References

1. E. Bøgh, in Interaction of Radiation with Solids, edited by A. Bishay (Plenum Press, Inc., New York, 1967), p. 361.

2. J. A. Davies, J. Denhartog, L. Eriksson and J. W. Mayer, Can. J. Phys. 45, 4053 (1967).

3. J. W. Mayer, L. Eriksson, S. T. Picraux and J. A. Davies, Can. J. Phys. 46, 663 (1968).

4. E. Bøgh, Can. J. Phys. 46, 653 (1968).

5. F. Brown, D. A. Marsden and R. D. Werner, Phys. Rev. Letters 20, 1449 (1968).

6. L. Eriksson, J. A. Davies, N. G. E. Johansson and J. W. Mayer, J. Appl. Phys. 40, 842 (1969).

7. J. Lindhard, Kgl. Danske Videnskab Selskab, Mat. Fys. Medd. 34, 14 (1965).

8. B. R. Appleton, C. Erginsoy and W. M. Gibson, Phys. Rev. 161, 330 (1967).

9. J. A. Davies, J. Denhartog and J. L. Whitton, Phys. Rev. 165, 345 (1967).

10. A. R. Sattler and G. Dearnaley, Phys. Rev. 161, 244 (1967).

11. S. Datz, C. Erginsoy, G. Leibfried and H. O. Lutz, Ann. Rev. of Nucl. Sci. 17, 129 (1967).

12. L. C. Feldman, Ph. D. Thesis, Rutgers University, December, 1966; also, L. Feldman and C. Erginsoy, Bull. Am. Phys. Soc. 12, 391 (1967).

13. L. C. Feldman and J. U. Andersen (to be published).

14. J. U. Andersen, Kgl. Danske Videnskab. Selskab, Mat. Fys. Medd. 36, 7 (1967).

15. C. Erginsoy, in Interaction of Radiation with Solids, edited by A. Bishay (Plenum Press, Inc., New York, 1967), p. 341.

16. J. U. Andersen and E. Uggerhøj, Can. J. Phys. 46, 517 (1968).

17. L. C. Feldman, B. R. Appleton and W. L. Brown, in Solid State Research with Accelerators (Brookhaven), p.58. Brookhaven Natl. Lab. Rept. No. 50083 (1968).

References

18. G. Dearnaley, B. W. Farmery, I. V. Mitchell, R. S. Nelson and M. W. Thompson, Phys. Rev. (in press, 1969).

19. B. R. Appleton, L. C. Feldman and W. L. Brown, in Solid State Research with Accelerators (Brookhaven), p. 45. Brookhaven Natl. Lab. Rept. No. 50083 (1968).

20. K. Lonsdale, Acta Cryst. 1, 142 (1948).

21. I. Bergström, K. Björkqvist, B. Domeij, B. Fladda and S. Andersen, Can. J. Phys. 46, 2679 (1968).

22. L. Eriksson and J. A. Davies, Arkiv Fysik (to be published, 1969).

23. L. C. Feldman and J. U. Andersen, 1969. Private communication.

24. R. Baron, G. A. Shifrin, O. J. Marsh and J. W. Mayer, J. Appl. Phys. (to be published).

25. W. M. Gibson, F. W. Martin, R. Stensgaard, F. P. Jensen, N. I. Meyer, G. Galster, A. Johansen and J. S. Olsen, Can. J. Phys. 46, 675 (1968).

26. L. N. Large and R. W. Bicknell, J. Mater. Sci. 2, 589 (1967).

27. J. F. Gibbons, Proc. IEEE 56, 295 (1968).

28. J. W. Mayer, IEEE Trans. NS-15, (No. 6) 10 (1968).

29. P. Sigmund, Appl. Phys. Letters 14, 114 (1969).

30. G. D. Watkins in Radiation Effects in Semiconductors, ed. F. L. Vook, p. 67 (Plenum Press Inc., New York, 1968).

31. K. Weiser, Phys. Rev. 126, 1427 (1962).

32. S. Fischler, Metallurgy of Advanced Electronic Materials (Interscience, New York, 1962).

33. C. Jech and R. Kelly, J. Phys. Chem. Solids (to be published, 1969).

34. J. W. Mayer, O. J. Marsh, G. A. Shifrin and R. Baron, Can. J. Phys. 45, 4073 (1967).

35. L. J. van der Pauw, Phillips Res. Repts. 13, No. 1 (1958).

36. O. J. Marsh, R. Baron, G. A. Shifrin and olde Jim Mayer, Appl. Phys. Letters 13, 199 (1968).

References

37. J. Lindhard, M. Scharff and H. E. Schiøtt, Danske Videnskab Selskab, Mat. Fys. Medd. 33, 14 (1963).

38. F. J. Morin and J. P. Maita, Phys. Rev. 96, 28 (1954).

39. J. C. Irvin, Bell Sys. Tech. J. 41, 387 (1962).

40. N. G. E. Johansson and J. W. Mayer (to be published).

41. C. B. Collins and R. O. Carlson, Phys. Rev. 108, 1409 (1957).

42. E. Bøgh and J. L. Whitton, Phys. Rev. Letters 19, 553 (1967).

43. B. W. Batterman and D. R. Chipman, Phys. Rev. 127, 690 (1962).

44. L. T. Chadderton, Phil. Mag. 18, 1017 (1968).